Absolute Measurements of the Fast Neutron Capture Cross Section of In^{115}

DANIEL JAMES GRADY

May 1981

Technical Report Number 101
Department of Nuclear Engineering

This work has been supported by
the U.S. Department of Energy.

ABSOLUTE MEASUREMENTS OF THE FAST NEUTRON CAPTURE CROSS SECTION OF In^{115}

by
Daniel James Grady

A dissertation submitted in partial fulfillment
of the requirement for the degree of
Doctor of Philosophy
(Nuclear Engineering)
at The University of Michigan
1981

Doctoral Committee:

Professor Glenn F. Knoll, Chairman
Professor Joachim W. Janecke
Assistant Professor William R. Martin
Professor J. Craig Robertson, University of New Mexico
Professor Dietrich H. Vincent

ABSTRACT

ABSOLUTE MEASUREMENTS OF THE FAST NEUTRON CAPTURE CROSS SECTION OF In^{115}

by
Daniel James Grady

Chairman: Glenn F. Knoll

The $In^{115}(n,\gamma)In^{116ml}$ cross section has been absolutely determined at neutron energies of 23, 265, 770 and 964 keV. These energies are the median neutron energies of the four photoneutron sources, Sb-Be, Na-D_2C, La-Be and Na-Be, utilized in this work. The measurements are independent of other cross section data except for corrections amounting to less than 10%.

Independent determinations of the reaction rate, detector efficiency, neutron source strength, scalar flux and target masses were performed. Reaction rates were determined by beta counting of the In^{116ml} decay activity using a 4π gas flow proportional counter. The detector efficiency was measured using $4\pi\beta$-γ coincidence counting techniques. A correction factor for non-ideal detector behavior and the complex decay scheme effects was performed using the foil absorber method of efficiency extrapolation. Photoneutron source emission rates were determined by intercomparison with a Cf^{252} spontaneous fission neutron source in The University of Michigan Manganese

Bath. The Cf^{252} source was itself calibrated against NBS-II, the secondary national neutron standard. The normalized scalar flux was calculated from the neutron emission angular distribution results of the Monte Carlo computer program used to model neutron and gamma transport in the source. Target mass determinations were made with a microbalance.

Correction factors were applied for competing reaction activities, neutron scattering from experiment components, room-return induced activities, spectral effects in the manganese bath and the neutron energy spectra of the photoneutron sources. The neutron energy spectra were also determined with the Monte Carlo program. The experimental cross section results were normalized to the source median energy using the energy spectra and cross section shape data.

The absolute cross sections obtained for the $In^{115}(n,\gamma)In^{116ml}$ reaction were 588 ± 12, 196 ± 4, 288 ± 10 and 203 ± 3 millibarns at 23, 265, 770 and 964 keV, respectively.

To my Parents,
Kevin, Nancy and Kathy

ACKNOWLEDGEMENTS

The author is indebted to his advisor, Professor Glenn Knoll, for his guidance, confidence, encouragement and personal friendship. Working with him has been an extremely rewarding experience.

The author wishes to express his thanks to Professor J. Craig Robertson for his many contributions to this work. His practical experience in the field of nuclear measurements was invaluable. His friendship and continuing encouragement were enough to make even the most frustrated experimentalist persevere.

This work was made possible with the support provided by the Department of Energy under Contract No. C-EY-76-S-02-2025.

The author gratefully acknowledges the contributions of Dr. John Engdahl. He was always willing to discuss any aspect of this work and his insight and experience provided invaluable lessons. In addition, his personal warmth and friendship are treasured by this author.

Special consideration is due George T. Baldwin for his invaluable contributions, suggestions and discussions. Working with him was a constant education and a truly rewarding experience. His professional expertise and more importantly, his personal friendship, are very important to this author.

Special thanks are also due the staff of the Ford Nuclear Reactor and the Phoenix Memorial Laboratory. Their cooperation and expert assistance made this work possible. Particular recognition goes to Mr. Ward Rigot for his innumerable services in the course of this work. Both his personal friendship and professional talent are held in the highest regard by this author.

Finally, the author wishes to thank Pam Derry for typing and assisting in the production of this manuscript. She turned a seemingly insurmountable task into an "almost" enjoyable experience.

TABLE OF CONTENTS

TABLE OF CONTENTS (cont.)

TABLE OF CONTENTS (cont.)

TABLE OF CONTENTS (cont.)

LIST OF TABLES

LIST OF TABLES (cont.)

LIST OF FIGURES

LIST OF FIGURES (cont.)

LIST OF FIGURES (cont.)

LIST OF APPENDICES

CHAPTER 1

INTRODUCTION

1.A. Motivation

The measurement and intercomparison of neutron fluxes in the keV energy region requires standard neutron cross section data. Traditionally, the $Au^{197}(n,\gamma)$ reaction has been utilized as a standard for neutron capture reactions. An alternative is available in the In^{115} neutron capture cross section. This isotope exhibits a cross section that is generally higher and less energy dependent. The reaction produces an activity (In^{116ml}) with a half life of 54.12 minutes which compares favorably with the often inconveniently long Au^{198} half life of 2.695 days. The target isotope is nearly as naturally abundant as Au^{197} (95.7% versus 100%) and has either small or very short lived competing reactions to consider.

Past cross section measurements have been carried out with the $In^{115}(n,\gamma)In^{116ml}$ cross section as a standard. These measurements have suffered from a lack of absolute cross section data in the keV neutron energy region. Ryves, et. al. (RYV 73) actually measured the In^{115} capture cross section in order to determine the flux for an U^{238} capture cross section determination. Where the data base

does exist, discrepancies in evaluated data and experimental results exceed 10% over much of the energy range. In order to effectively use this reaction as a standard, more absolute measurements at discrete neutron energies, using independent experimental techniques are required.

A secondary motivation for this work is the expansion of the capabilities of The University of Michigan Absolute Cross Section Measurement Facility. Previous experiments have provided the expertise to absolutely measure fission cross sections (GIL 73, DAV 76, GRA 79), (n,α) cross sections (STE 75, ENG 78) and nu-bar for spontaneous fission neutron sources (BOZ 76). With the completion of this work, generalized activation or absolute capture cross section measurements are added to the above list of capabilities. The experimental equipment and methodology as well as the analytical procedure are now in place.

1.B. General Discussion of the Measurements

1.B.1. Measurements of Interest

In the present work the absolute neutron capture cross section of In^{115} has been measured at neutron energies of 23, 265, 770 and 964 keV. The measurements are absolute because to first order they do not depend upon any other cross section data. Correction factors amounting to less than 10% in general, are the only aspects of these measurements which rely on other cross section data.

Neutron capture in In^{115} populates three relatively long lived (greater than one second) energy states of the In^{116} product nucleus. The decay modes and branching ratios for these three energy levels are diagrammed below and were obtained from Lederer (LED 78).

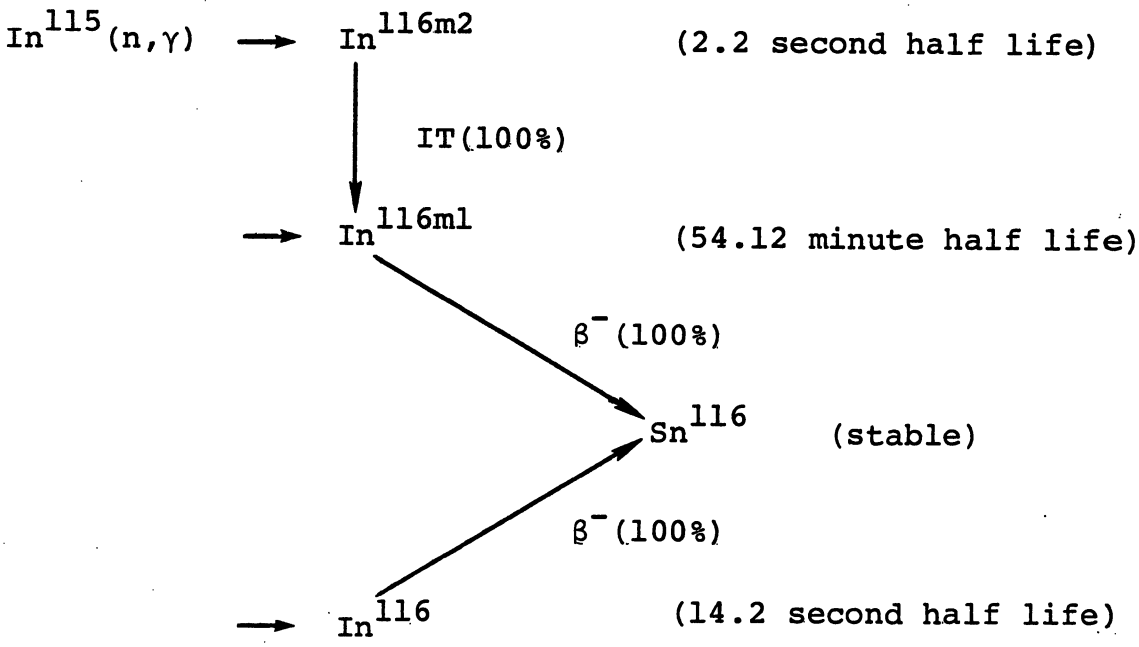

The first metastable state, In^{116m1}, bypasses the usual isomeric transition (IT) to the ground state. Instead it decays by beta emission to the stable Sn^{116} isotope. Because the delay between foil activation and foil counting is about 30 minutes, only In^{116m1} activity will remain to be detected in the ideal case of no competing reaction activities. Consequently, the capture cross section being measured is for the reactions which directly or indirectly populate the In^{116m1} metastable state. Through-

out further discussion this metastable state will be referred to as In^{116m}.

1.B.2. Measurement Strategy

Indium target foils were irradiated at various distances from each of the four photoneutron sources. The resulting In^{116m} activity was detected in a $4\pi\beta$ gas flow proportional counter. Count data was reduced to saturated activity per indium target atom. Independent determinations of the beta detector efficiency, the neutron source strength and the scalar flux were combined with the saturated activity data to arrive at the neutron capture cross sections.

1.B.3. Actual Quantity Measured

The actual cross section measurements were considerably more involved than the idealized methodology above suggests. Expressed in terms of saturated activities (the activity produced after infinite irradiation time with a constant strength neutron source), the counts recorded from the actual foil counting in the beta detector reduced to the following expression:

$$\lambda N + \sum_{i=1}^{ncom} \lambda_i N_i = \varepsilon_\beta N' \bar{\sigma} (\phi_o + \delta\phi_o) S_o$$

$$+ \varepsilon_\beta N' (\overline{\sigma\phi_{RR}})$$

$$+ \sum_{i=1}^{ncom} \varepsilon_{\beta i} N_i' \bar{\sigma}_i (\phi_o + \delta\phi_o) S_o$$

= In^{116m} activity through direct production

+ In^{116m} activity produced by room-return neutrons

+ Competing reaction activities

where: λN = saturated In^{116m} activity from all sources

$\lambda_i N_i$ = i^{th} competing reaction product activity

ε_β = absolute beta detector efficiency for In^{116m}

$\varepsilon_{\beta i}$ = absolute beta detector efficiency for the i^{th} competing reaction product

N' = number of In^{115} target atoms

N_i' = number of parent target atoms for the i^{th} competing reaction

$\bar{\sigma}$ = neutron energy spectrum averaged $In^{115}(n,\gamma)In^{116m}$ cross section

$\bar{\sigma}_i$ = neutron energy spectrum averaged cross section for the i^{th} competing reaction

$N'(\overline{\sigma\phi_{RR}})$ = room-return induced In^{116m} activity

ϕ_o = normalized neutron scalar flux (n/cm^2) due to direct source neutrons

$\delta\phi_o$ = normalized neutron scalar flux due to neutrons scattered by the experimental package

S_o = neutron source strength at start of foil irradiation (n/s)

The direct production In^{116m} activity of interest was masked by spacing-independent room-return activity and a variety of small, spacing-dependent competing reaction activities. Consequently, experiments and analyses were devised to account for these added activities.

1.B.4. Organization of the Discussion

The discussion has been organized to follow the basic approach of the capture cross section measurements. That approach was the reduction of the saturated activity expression of the last section to a series of independent experiments or calculations. A brief description of the various steps performed in this capture cross section work is summarized here.

Photoneutron sources were activated in the Ford Nuclear Reactor. Their yield of photoneutrons were then used to irradiate a series of indium target foils placed

at up to seven different distances from the source. The activated foils were transferred to the $4\pi\beta$ gas flow proportional counter for the relative beta decay activity determination.

Photoneutron source strengths were determined by the relative manganese bath method. The saturated manganese activity induced in the bath by a photoneutron source was compared with that obtained from a pair of Cf^{252} standard calibration runs. The Cf^{252} spontaneous fission neutron source strength was determined from a calibration against NBS-II, the secondary national neutron standard.

The beta detector efficiency for the In^{116m} decay was measured using $4\pi\beta$-γ coincidence counting techniques. A NaI(Tℓ) gamma ray detector system was added to the beta detector system. Coincidence experiments resulted in the foil-dependent, apparent beta detector efficiencies. Efficiency variation experiments resulted in the decay spectrum correction factor required to adjust the apparent efficiencies for complex In^{116m} decay scheme effects.

Beta detector efficiencies for competing reaction activities were determined experimentally or by extrapolation. The efficiency for the In^{115m} activity produced in an inelastic scattering reaction with In^{115} was experimentally obtained using absolute gamma counting with a Ge(Li) detector system. Extrapolated efficiencies were calculated based upon the In^{115m} and In^{116m} efficiencies,

mean beta or internal conversion electron energies and electron emission branching ratios.

The scalar neutron flux, normalized to a source strength of one neutron per second, was calculated from the results of a Monte Carlo computer program. Used to model neutron and gamma transport in the photoneutron sources, the code calculated the neutron emission angular distribution. A fifth order polynomial expansion of this distribution was integrated to obtain an analytic expression for the scalar flux averaged over the surface of an indium target foil.

Four major correction factors were determined. Neutron inscatter from the experimental package back toward the target was calculated using a point source-point scatterer-point target approximation with limited scattering anisotropy capability. Backscatter in the target foil holder was determined using a Monte Carlo based, average path length through the foil calculation. The room-return activity correction was derived from a plot of the saturated In^{116m} activity per target atom versus the spacing-dependent scalar flux. The y-intercept is the activity associated with the spacing-independent room-return. Finally, the measured capture cross sections were normalized to the source median energy using the calculated neutron energy spectrum and $In^{115}(n,\gamma)In^{116m}$ cross section shape data.

1.B.5. General Comments on Error Analysis

All errors quoted in this work reflect uncertainties at the 68% confidence level or one standard deviation. Uncorrelated error propagation has been performed using the standard equation. If $u = f(x,y...)$, the uncertainty in u, σ_u, is calculated from

$$\sigma_u^2 = \left(\frac{\partial f}{\partial x}\right)^2 \sigma_x^2 + \left(\frac{\partial f}{\partial y}\right)^2 \sigma_y^2 + \ldots$$

A distinction is drawn here between random and systematic uncertainties. The latter being interpreted as those quantities that cannot be reduced by repeated measurement. These quantities reflect uncertainties inherent in the experiment design and performance. Random uncertainties are in general associated with stochastic processes and in this work are predominantly due to counting statistics. These uncertainties can be reduced by repeated measurement of the same quantity using the same technique. Table 1.B.1 is a list of the major uncertainties in this work.

Table 1.B.1

Major Uncertainties Associated with This Work

Systematic

- -Neutron Source Calibration
- -Indium Foil Mass
- -Flux Calculations
- -Scattering Calculations
- -Decay Corrections
- -Competing Reaction Corrections
- -Neutron Energy Spectrum
- -Aspects of the Decay Spectrum Correction

Random

- -Apparent Efficiency Determination
- -Foil Activity Measurement
- -Dead Time Determinations
- -Room-Return Correction
- -Source-Target Spacing Measurements

CHAPTER 2

PHOTONEUTRON SOURCES AND SOURCE STRENGTH DETERMINATION

The four measurements of the capture cross sections were obtained as averages over the neutron energy spectra of the associated photoneutron sources. These sources were activated in the Ford Nuclear Reactor and calibrated using The University of Michigan Manganese Bath System. The neutron emission rate for each source was provided by a relative comparison with a Cf^{252} spontaneous fission neutron source, calibrated in turn against NBS-II, the secondary national neutron standard.

2.A. Source Description

Table 2.A.1 contains a summary of the pertinent data for the four photoneutron sources. The median neutron energies or the energies to which the final cross sections were normalized are 23, 265, 770 and 964 keV for the Sb-Be, Na-D_2C, La-Be and Na-Be sources respectively. The photoneutron sources are comprised of up to four concentric spherical shells as depicted in figure 2.A.1. The innermost region is the gamma emitting core which is enclosed by the aluminum containment shell of region #2. Region #3 is the neutron producing shell of either beryllium or

Table 2.A.1

Photoneutron Source Parameters

Parameter	Photoneutron Source			
	Sb-Be	Na-D_2C	La-Be	Na-Be
Neutron energy (keV):	23	265	770	964
Radii (cm):				
R1	1.448	1.190	1.190	1.504
R2	1.499	1.505	1.505	1.504
R3	1.799	1.796	1.806	1.798
R4	2.099	1.796	1.806	1.798
Core materials:	Sb	NaF	La_2O_3	NaF
Mass (g)	85.091	8.903	13.905	30.959
Core containment:	Aluminum	Aluminum	Aluminum	N/A
Mass (g)	3.756	19.110	19.100	-
Target Materials:	Beryllium	Deuterium	Beryllium	Beryllium
Mass (g)	19.027	10.620	19.135	18.729
(γ,n) Threshold (MeV)	1.665	2.225	1.665	1.665
Source containment:	Aluminum	N/A	N/A	N/A
Mass (g)	38.727	-	-	-
Gamma emitter:	Sb^{124}	Na^{24}	La^{140}	Na^{24}
Energy (MeV)	1.691	2.754	2.522	2.754
Branching ratio	0.49	1.00	0.03	1.00
Half life	60.2 days	15.01 h	40.23 h	15.01 h

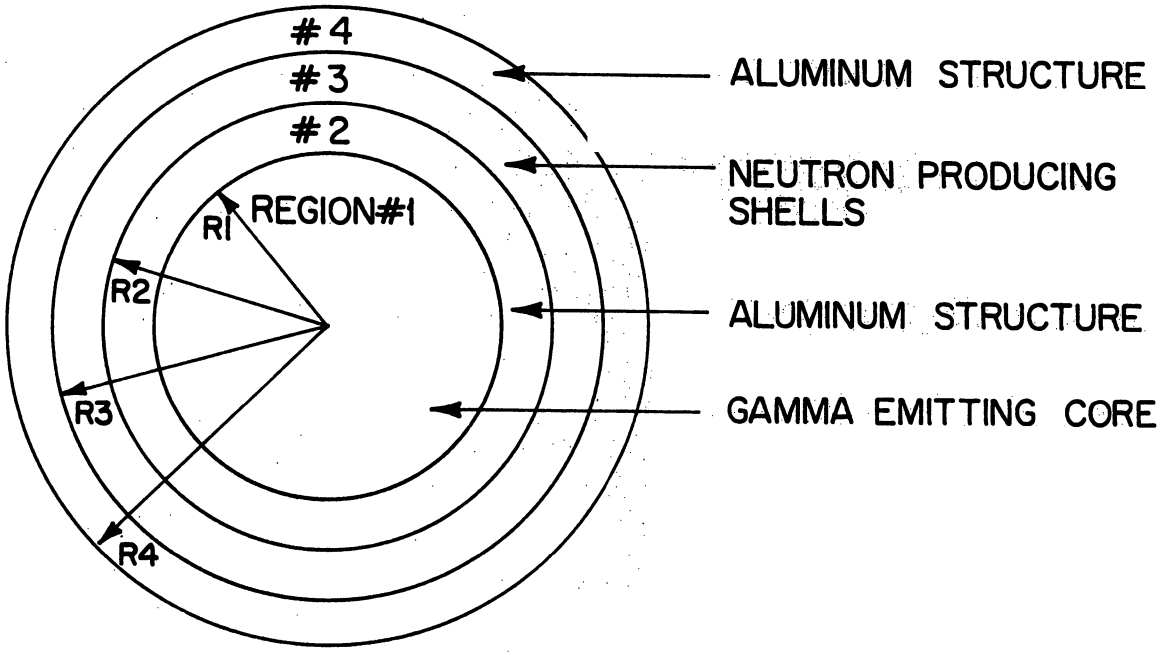

Figure 2.A.1. Schematic of Photoneutron Source Construction

deuterated polyethylene. Composed of a pair of adjoining hemispherical shells, this region has a 3 mm nominal thickness.

Region #4 is the aluminum source containment shell. Found on the Sb-Be source only, this pair of threaded, aluminum hemispheres serves two purposes. Firstly, the shells insure source integrity in the event that the source is dropped and the brittle antimony core breaks. Secondly, the source geometry is maintained without the use of an adhesive to secure the beryllium shells to the antimony core. This adhesive is subject to source-

induced, radiation degradation. The consequences of the loss of a beryllium shell could not be tolerated.

The Na-Be source is also a special case in terms of construction. The core was fabricated by high pressure molding of granular sodium fluoride. A small amount of aluminum was added to facilitate the molding process. The core is fit with a pair of beryllium hemispheres which are attached to one another with small beryllium pins. A small shell mismatch of 0.007 cm was filled with and welded in place by fine beryllium wire.

The remaining sources, Na-D_2C and La-Be, both began with a pair of 0.3175 cm thick aluminum hemispherical shells. A small hole was drilled into one hemisphere and the two halves were welded together. Sodium fluoride or lanthanum oxide powder was packed into the hollow spheres. The sources were welded shut and remachined to spheres of radius, R2. The neutron shells were press-fitted onto the source assemblies after neutron irradiation in the reactor.

All three pairs of beryllium shells were machined from beryllium metal to an inside radius of 1.5 cm and a thickness of 3 mm. The deuterium shells were produced from 98% polyethylene powder obtained from BIO-RAD Industries in Richmond, California. The shells were fabricated by Davis using a target shell mold and press (DAV 76, p.31).

2.B. Source Activation

Only the Sb-Be and Na-Be sources were activated with the neutron shells attached. In the case of the deuterium shells of Na-D_2C, the motivation for this activation scheme is clear. The large neutron and gamma doses associated with reactor activation would quickly destroy the polyethylene shells. In the case of the beryllium shells of the La-Be source, the problem of the adhesive degradation in the intense radiation fields of the reactor also precluded irradiation of the complete source. The neutron producing shells for both of these sources (NaD_2C and La-Be) were remotely press-fitted onto the cores once reactor activation had been completed.

How is this accomplished?

That portion of the sources which was to be irradiated in the reactor was placed in a "pull tab" can. Aluminum foil was packed around the source to facilitate heat transfer from the source during irradiation. The can was then sealed, checked for water tightness and placed in the rotator assembly. The assembly was next positioned on the south face of the Ford Nuclear Reactor and attached to the rotator motor. Uniform activation was accomplished both axially and radially. Axially, the source irradiation was performed at the midplane of the core where the flux is approximately constant. Radial uniformity was attained by rotating the source at three revolutions per minute throughout irradiation. Activation durations of 20 days

Let's look at some of the impurities encountered?

for the Sb-Be source, 80 hours for the La-Be source and 50 hours for the two sodium based sources were performed in a thermal flux of about 10^{13} neutrons/cm^2·s.

Immediately upon completion of the source irradiation, the can containing the source was transferred, via a water lock, from the reactor pool to hot caves equipped with remote manipulator assemblies. Here, the source was removed from the can, neutron producing shells were pressed on when appropriate and the completed source was placed in the retractable sliding tray of a teletherapy shielding unit. The shield was wheeled to the photoneutron laboratory where the experiments were performed. Here the shield was mated with the transfer cask docking port diagrammed in figure 3.C.2 of the next chapter.

The above procedure was followed for the Sb-Be source, but only after a one month decay period in the reactor pool. Substantial decay of the Sb^{122} activity (2.72 day half life) also produced during irradiation was required to facilitate source handling.

Short and long lived source impurities with gamma ray decay energies exceeding the (γ,n) thresholds in Table 2.A.1 were investigated. Long lived activities were responsible for the residual activities of all four sources as each had been activated several times previous to this work. A Ge(Li) detector analysis of this residual activity showed no appreciable gamma rays above the (γ,n) thresholds.

All activities were attributed to impurities in the aluminum structural material.

Short lived activities with half lives on the order of source half lives were investigated by Bowman (BOW 76) and Davis (DAV 76). Gamma analysis after half hour reactor irradiations and several hours of decay demonstrated no appreciable impurities capable of neutron production.

2.C. Source Strength Calibration

The neutron emission rates of the photoneutron sources were determined using the relative manganese bath technique. Saturated activities induced in the manganese by a photoneutron source were compared with those induced by the calibrated Cf^{252} spontaneous fission neutron source to obtain the neutron emission rate. The Cf^{252} source, itself a tertiary standard, was calibrated against the secondary national neutron standard, NBS-II.(1) High geometric efficiency,(2) small and easily determined correction factors and(3) very limited neutron energy dependence were the prime motivations for using this calibration technique.

The University of Michigan Manganese Bath Calibration System was designed and built by Gilliam (GIL 73) and Stephany (STE 75). The saturated activity analysis originally developed by these authors was incorporated into the computer program, SAT2. Refinements to this analysis

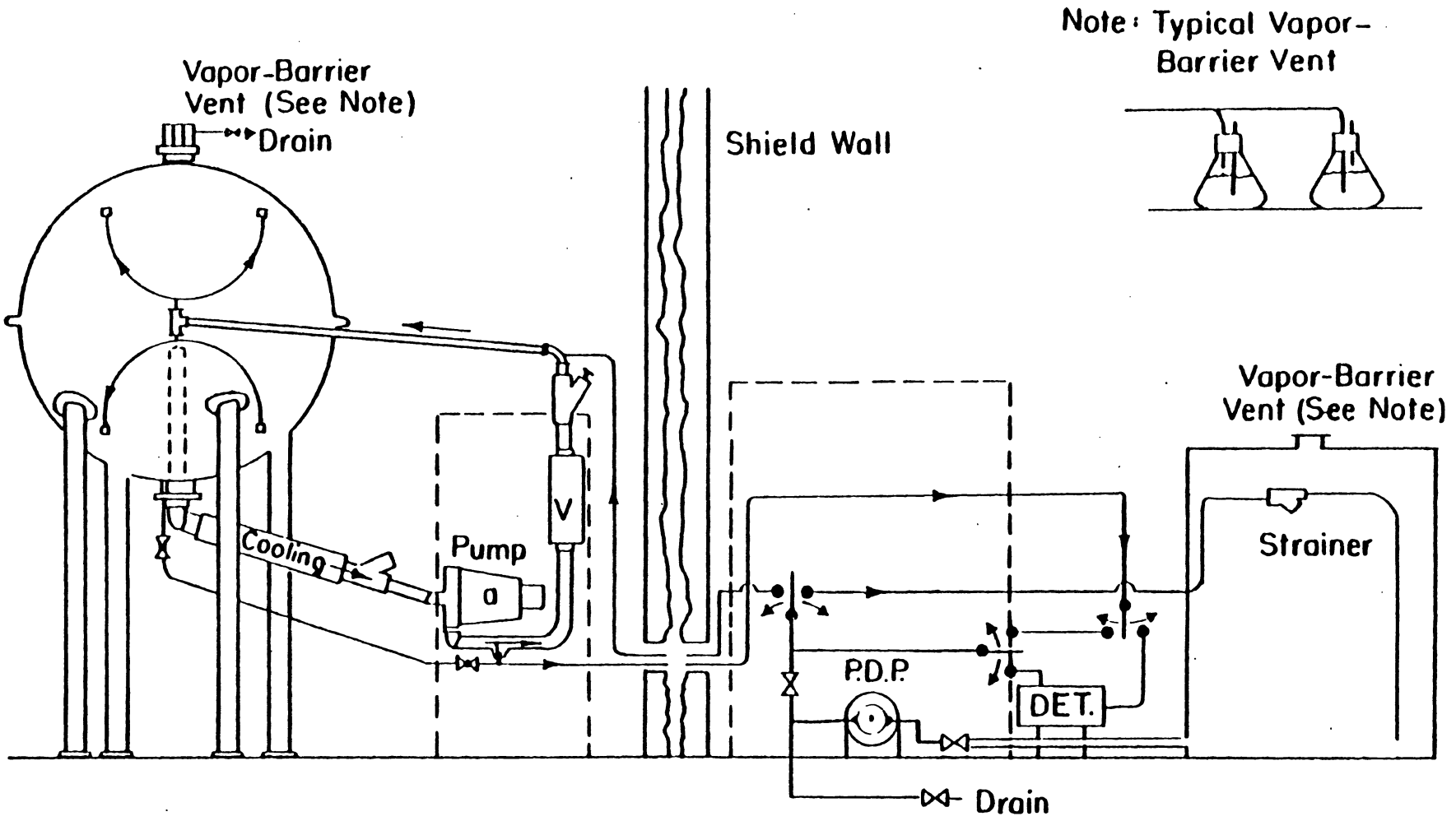

Figure 2.C.1. The University of Michigan Manganese Bath System

scheme have been applied by others (DAV 76, ENG, 76, BOZ 76) and were continued in this work.

2.C.1. Manganese Bath Calibration System

The manganese bath, shown in figure 2.C.1, as well as the calibration of the detector system electronics have been thoroughly discussed by previous authors (GIL 73, DAV 76, BOZ 76, ENG 78). For completeness, only a brief synopsis will be included here.

The bath is a one meter diameter, stainless steel sphere filled with a 1.3 gm/cm^3 density solution of manganese sulfate monohydrate and deionized water. A drywell machined from a plastic graduated cylinder positions the source at the center of the bath. Since most neutron capture in the solution occurs within the first 10 cm of the source, solution is withdrawn from the bath at a point 7 cm below the bath center. Most of this solution is then reinjected into the sphere at eight uniformly distributed points on the surface to facilitate rapid mixing of freshly induced Mn^{56} activity.

A small portion of the withdrawn solution is pumped to an adjoining room and into a lucite detector chamber which is heavily shielded with iron and lead. Mounted perpendicular to the axis of the chamber cylinder and in an inverted drywell is a 3"x3" NaI(Tℓ) detector, photomultiplier tube and preamp. The activated manganese solution circu-

lates through the detector chamber in a constant volume detection geometry and is pumped back to the manganese bath.

High stability, low noise electronics are employed in the signal analysis of the pulse information obtained from the NaI detector. A time history of the Mn^{56} activity induced by the neutron source is obtained from the counting of logic pulses produced by the energy discrimination of a single channel analyzer (SCA). A multichannel analyzer (MCA) operated in multiscaling mode with a channel of 400 seconds and a fixed dead time of 3 μs is used to accumulate the activity history. The 512 channel MCA in this configuration can accumulate a 57 hour activity history.

A reproducible SCA discriminator window is required in order to intercompare saturated activity results from one bath run to the next. This window is defined by adjusting the amplifier gain so that the ratio of count rates above a pair of SCA discriminator settings (for a Co^{60} check source) is constant. The result is an SCA window from 0.05 to 2.50 MeV, encompassing the 0.847, 1.81 and 2.11 MeV gamma energies from the Mn^{56} decay.

2.C.2. Manganese Bath Data Analysis

The reduction of the actual activity history data from the MCA to a quantity related to the neutron source strength has been discussed extensively by Engdahl

Activity of Mn^{55}

(ENG 78). Only a summary of the analysis will be included here, further details can be obtained from the above mentioned reference.

A neutron source is positioned in the drywell at the center of the manganese bath. Neutrons emitted into the solution are thermalized and captured in the various components of the solution. The only activity formed is due to the fraction, f, of neutrons captured by Mn^{55} to produce Mn^{56}, a β-γ emitter with a 2.582 hour half life. Constant mixing of the solution provides for a uniform distribution of this Mn^{56} activity within the bath volume. Data accumulated during an MCA channel duration, Δ, is simply the integrated counts from the NaI detector system. The detector efficiency, ε, is assumed to be constant as long as both the solution temperature and density remain fixed over the duration of an entire source calibration.

Assuming a constant source strength and instantaneous, uniform mixing of the Mn^{56} activity, the saturated activity count rate from the NaI detector would be, CR_s,

$$CR_s = \varepsilon f S_o = \varepsilon \lambda_{56} N_{56,s} \qquad 2.C.1$$

where: S_o = constant source strength

λ_{56} = Mn^{56} decay constant

$N_{56,s}$ = number of saturated Mn^{56} nuclei

The saturated count rate ratio of $CR_{s,1}$ for the photoneutron source, to $CR_{s,2}$ for the Cf^{252} standard gives

$$\frac{CR_{s,1}}{CR_{s,2}} = \frac{\varepsilon_1 f_1 S_{o,1}}{\varepsilon_2 f_2 S_{o,2}} \qquad 2.C.2$$

Is the detection energy dependent?

In practice, the detector efficiencies are equal because the constant solution temperature and density criteria were easily met throughout the source calibration. The neutron absorption fractions are not in general equal because of a number of source dependent gain and loss mechanisms. The fractions are assumed equal in the initial analysis and deviations are accounted for with correction factors discussed in section 2.C.3.

With $\varepsilon_1 f_1 = \varepsilon_2 f_2$, the saturated count ratio reduces to the source strength ratio. Consequently, the photoneutron source strength is simply the saturated count rate ratio multiplied by the Cf^{252} neutron emission rate, $S_{o,2}$. In this simple constant source case, calibration can be performed by separately placing the photoneutron source and the Cf^{252} standard in the bath, allowing Mn^{56} activity to equilibrate or saturate and then recording the respective count rates.

Two factors of the actual calibration process complicate this ideal case. The first is that the photoneutron source half lives are of the same order as the calibration

$(n,\gamma) \rightarrow (\gamma,n)$ exactly how this works?

photoneutron source

experiment duration, about 24 hours. Consequently, the discretized activity history from the MCA-NaI detector system must be source decay corrected.

Secondly, there is a small delay before the induced activity is uniformly mixed. Freshly produced Mn^{56} activity is concentrated at the bath center from which the mixing and detector sample solution is withdrawn. As a result, the detection efficiency for freshly induced activity is greater than that for the past activity which has long since been uniformly mixed throughout the bath volume. In the saturated activity analysis the detection efficiency for the most recently produced activity is taken as $(1+\delta)\varepsilon = (CE)\varepsilon$. The CE correction factor is applied to only the activity added in the interval τ just previous to the present time. A value of 540 seconds for τ, the mixing time, was experimentally determined by Snapp (SNA 76) by injecting a bolus of Mn^{56} activity and determining the time, after injection at the bath center, to uniform concentration of the activity. The CE correction is applied to only the count rate data when the source is in the bath. Once the source is removed and after a mixing time τ has expired, all activity is assumed uniformly mixed so that CE=1. After that, the activity should decay with the characteristic Mn^{56} half life.

Actual CE values are a function of the median neutron energy of the source. The harder the energy spectrum, the

more nearly uniform the fresh activity is distributed because neutron thermalization and capture occurs at increasingly greater distances from the bath center and solution sampling inlet point. Consequently, the CE value goes inversely with neutron energy. In the application of the CE correction, previous experience with all of the sources dictated a specific value of CE for each source. In other words, CE was not treated as a variable parameter in the data reduction for a specific source.

Each bath run was broken into three time segments. The first 10 to 20 channels of count data were background. The source was then placed in the bath either by hand (Cf^{252} only) or by remote handling with vacuum manipulators (all four photoneutron sources). After about 24 hours of activation (about 220 channels), the source was removed and the Mn^{56} activity was allowed to decay to background for about 30 hours. Channel-by-channel calculation of the saturated activity corrected to the instant of source insertion in the bath was performed for all build-up and decay channels (i.e., time segments two and three above). The two equations used in the discretized saturated activity calculations are:

Build-up Region

$$CR_{s,n} = \varepsilon f S_o = \frac{C_n e^{s t_n (\lambda - s)/\lambda}}{\left(\frac{e^{s\Delta} - 1}{s}\right)\left[e^{(s-\lambda)\tau}\left(1 + CE\left(1 - e^{(s-\lambda)\tau}\right)\right) - \frac{e^{(s-\lambda)t_n}}{\lambda}\left(e^{\lambda s} - 1\right)\right]}$$

Decay Region

$$CR_{s,n} = \varepsilon f S_o = \frac{C_n e^{\lambda t_n (\lambda - s)}}{(e^{(\lambda - s)T} - 1)(e^{\lambda \Delta} - 1)}$$

where: $CR_{s,n}$ = saturated count rate for channel "n"

C_n = dead time and background corrected number of counts in channel "n"

λ = Mn^{56} decay constant

s = neutron source decay constant

t_n = time from source insertion to start of channel "n"

Δ = channel dwell time = 400 seconds

τ = mixing time = 540 seconds

CE = detector efficiency correction factor for the most recently induced Mn^{56} activity

T = source residence time in the bath

The computer program SAT2 performed the above data reduction and provides an error weighted saturated activity value for both the build-up and the decay region. Propagation of counting statistics errors throughout the calculation is also performed.

2.C.3. Data Reduction and Error Analysis

2.C.3a. SAT2 analysis of manganese bath data

The photoneutron source strength calibration strategy consisted of three manganese bath runs, one for the

photoneutron source and two for the Cf^{252} standard. After at least one week of uninterrupted manganese solution circulation to equilibrate temperature and flow, a pre-experiment Cf^{252} bath run was performed. Upon completion the bath was drained and the indium foil irradiations were carried out in the low-albedo laboratory which housed the bath. The bath was drained to minimize the backscatter of neutrons to the experimental package. After the foil irradiations (about 16 hours) the bath was refilled. The solution was circulated for 10 hours to re-establish the Cf^{252} calibration conditions and the photoneutron source was transferred to the bath. The second Cf^{252} run was performed once the bath activity from the photoneutron source run had decayed to background.

The amplifier gain calibration for the NaI detector system was checked at the completion of each bath run. Drifting from the pre-run calibration was observed in most cases and was prevalent during the humid summer months when the experiments were performed. Channel-by-channel SAT2 results demonstrated that the drifting was fairly linear with time. SAT2 was modified to correct for the drifting effect. An efficiency correction that was linear with time was applied to the MCA activity history data. The slope of this efficiency variation correlated quite well with the size and direction of the amplifier gain shifts.

Maximum corrections to specific channel saturated activities as a result of this efficiency option were about 0.8%. The overall effect of the efficiency correction on the average saturated activity result was determined by running SAT2 with and without the option. A typical difference of about 0.3% was observed. The uncertainty attributed to this gain shift correction was assumed to be 50% of the typical effect or about 0.15%.

The activity history data from all of the manganese bath runs was processed to obtain the build-up region and decay region saturated activity values. Table 2.C.1 contains a summary of the SAT2 results for the manganese bath data. The uncertainties quoted in the table are the result of counting statistics error propagation only.

2.C.3b. Correction factors and uncertainties

All the correction factors required for the saturated activity results from SAT2 were associated with the fraction, f, of neutrons absorbed in the manganese. The value of this fraction was assumed constant initially but is actually a function of such factors as the neutron energy spectrum, the gamma energy spectrum and the source construction. Factors which affect the fraction included bulk neutron leakage from the bath, neutron streaming through the source drywell, source and drywell absorption of thermalized return neutrons, fast capture losses in oxygen and sulfur (high energy neutrons only) and photo-

Table 2.C.1

Summary of SAT2 Results

Source	Normalization Time	CE Value	Saturated Activity (counter/second)	Region
Cf^{252}	12:26:11 9/4/80	1.06	771.66 ± 0.108 772.07 ± 0.272	Build-up Decay
Sb-Be	15:16:25 9/1/80	1.10	5762.3 ± 0.293 5763.6 ± 0.723	Build-up Decay
Cf^{252}	16:39:37 9/8/80	1.06	769.97 ± 0.107 770.38 ± 0.275	Build-up Decay
Cf^{252}	01:33:24 8/11/80	1.06	778.52 ± 0.112 779.04 ± 0.271	Build-up Decay
$Na\text{-}D_2C$	19:46:45 8/8/80	1.09	1197.0 ± 0.162 1198.4 ± 0.547	Build-up Decay
Cf^{252}	11:36:17 8/13/80	1.06	777.84 ± 0.106 778.45 ± 0.270	Build-up Decay

Table 2.C.1 (cont.)

Source	Normalization Time	CE Value	Saturated Activity (counter/second	Region
Cf^{252}	12:04:13 8/19/80	1.06	774.29 ± 0.106 774.70 ± 0.258	Build-up Decay
La-Be	13:13:15 8/23/80	1.07	173.55 ± 0.053 173.61 ± 0.169	Build-up Decay
Cf^{252}	10:35:36 8/26/80	1.06	769.90 ± 0.101 770.45 ± 0.257	Build-up Decay
Cf^{252}	01:33:24 8/11/80	1.06	778.52 ± 0.112 779.04 ± 0.271	Build-up Decay
Na-Be	11:58:59 8/2/80	1.07	4326.3 ± 0.297 4327.2 ± 1.062	Build-up Decay
Cf^{252}	11:36:17 8/13/80	1.06	777.84 ± 0.106 778.45 ± 0.270	Build-up Decay

activation of the natural deuterium content of the bath solution. Table 2.C.2 contains a summary of these correction factors as well as associated errors.

(1) The bulk leakage for the Cf^{252} source was measured by Bozorgmanesh (BOZ 76) and verified by Engdahl (ENG 76) using the computer program ANISN. Additional ANISN calculations for the remaining photoneutron sources showed negligible leakage contributions. The uncertainty in this correction was assumed to be 0.03% for all sources based upon the statistics from the Bozorgmanesh measurement.

(2) Neutron streaming from the source drywell is a simple solid angle calculation and was performed for the five sources. As expected, the four photoneutron sources have the same correction because they are about the same size. The Cf^{252} source appears as a point source and so the correction is slightly smaller than for the finite extent photoneutron sources. A 30% uncertainty in the correction was assumed.

The source and drywell absorption corrections for reentry neutrons were determined experimentally by Davis (DAV 76) and Engdahl (ENG 78) using a technique suggested by Robertson. The reentry flux at the source was measured using manganese absorbers in the drywell, above and below the source. Assuming a thermal neutron spectrum and with the macroscopic absorption cross sections of the sources and drywell, the loss of neutrons due to self-absorption

Table 2.C.2

Manganese Absorption Fraction Correction Factors*

Source	Bulk Leakage	Source well Streaming	Source self-Absorption	Fast Capture Losses	Photo-activation	Total Correction
Sb-Be	0.00±0.03	0.10±0.03	1.26±0.18	-	-	1.36±0.18
Na-D_2C	0.00±0.03	0.10±0.03	0.44±0.07	-	-0.72±0.10	-0.18±0.13
La-Be	0.00±0.03	0.10±0.03	0.54±0.10	-	-0.96±0.10	-0.32±0.15
Na-Be	0.00±0.03	0.10±0.03	0.30±0.05	-	-0.94±0.10	-0.54±0.12
Cf^{252}	0.24±0.03	0.08±0.03	0.12±0.02	0.642±0.20	-	1.09±0.20

*Correction factors and uncertainties in units of %

was determined. Uncertainties in the fluxes and cross sections combined to give an uncertainty in the correction equal to about 15% of the correction itself.

④ Fast capture losses in oxygen and sulfur were limited to the high energy Cf^{252} neutron spectrum because these are threshold reactions. The value used was the result of an ANISN calculation by Engdahl. The error associated was that suggested by Davis.

⑨ Photoactivation of the deuterium of the bath was limited to those sources that emit gammas of energy greater than 2.225 MeV, the (γ,n) threshold. Gilliam and Davis measured these corrections by comparing SAT2 determined saturated activities for the sources with and without the neutron producing target shells. Uncertainties in these corrections reflect counting statistics errors from the SAT2 analysis.

Table 2.C.3 is a summary of the errors associated with the determination of the saturated counting rate that are not covered by random statistical uncertainties from SAT2 or the uncertainties associated with the correction factors.① The photoneutron source half life error reflects only the uncertainty in the decay of the source during the calibration in the manganese bath. No such error was applied for the 2.64 year Cf^{252} half life.② The amplifier gain stability error was taken as 0.15% and was due

Table 2.C.3

Additional SAT2 Saturated Activity Uncertainties

Source of Error	Error %
Photoneutron source half life	0.11
Amplifier gain stability	0.15
Dead time of electronics	0.15
Mixing parameter "τ"	0.09
Average bath background	0.075
Quadrature sums:	
Photoneutron sources	0.27%
Cf^{252} standard	0.24%

to the time dependent efficiency correction (discussed in section 2.C.3a.). The dead time error was calculated assuming a 10% uncertainty in the dead time and a maximum count rate of 5000 counts per second. A 20% uncertainty in τ, the mixing parameter of section 2.C.2 gave rise to a 0.09% uncertainty in the saturated activity results. Finally, the contribution of the uncertainty in the average background for the bath was taken as 0.075%. These errors were added in quadrature to obtain a value of 0.27% for the photoneutron sources and 0.24% for the Cf^{252} standard.

SA ~ 5

2.C.3c. Source calibration results

The conversion of the SAT2 saturated activity results to the photoneutron source emission rate was accomplished using the computer program, STRENGTH. A listing of the program and the input requirements can be found in Appendix A. The program accepts as input the saturated activity results for the two Cf^{252} standard runs and the photoneutron source run. The correction factors and all the uncertainties discussed in section 2.C.3b are processed by the code. With a Cf^{252} calibration source strength of 6.788×10^6 neutrons/second $\pm$ 0.58% on 8/21/77, the photoneutron source strengths are determined with the associated uncertainties. These uncertainties are composed of the quadrature sum of several error sources. In addition to the correction factor uncertainties and the saturated activity errors of Table 2.C.3, the standard source strength uncertainty (0.58%), random statistical variations from the bath counting data (0.03%), and the Cf^{252} source half life uncertainty (propagated error about 0.4%) are also included in the calibration calculations of STRENGTH. The final photoneutron source strength and uncertainty as calculated by STRENGTH is corrected to the exact time of photoneutron source insertion in the manganese bath.

As the activated indium foil activities are all normalized to the neutron source strength at the beginning

what exactly is this?

of the irradiation of the first foil, the neutron source strength from STRENGTH must be corrected for decay to that point in time. This adjustment was performed and one additional error component was added as a result. Assuming a 0.1% uncertainty in photoneutron source half lives, a small uncertainty (about 0.1%) was added to the STRENGTH determined error bar to account for the time normalization.

Table 2.C.4 contains a summary of the photoneutron source strengths at the beginning of the actual indium foil activation experiments. These values are also indicative of the maximum neutron source strength now attainable with these sources under the activation conditions of section 2.B.

Table 2.C.4

Photoneutron Source Strengths

Source	Date	Time	Neutron Emission Rate (neutrons/second)
Sb-Be	9/1/80	15:16:25	$2.319 \times 10^7 \pm 0.81\%$
Na-D_2C	8/8/80	19:46:45	$1.686 \times 10^7 \pm 0.80\%$
La-Be	8/23/80	13:13:15	$1.353 \times 10^6 \pm 0.80\%$
Na-Be	8/2/80	11:58:59	$4.759 \times 10^7 \pm 0.80\%$

2.C.4. The Cf^{252} Tertiary Standard

2.C.4a. Original Calibration against NBS-II

Previous cross section measurements at The University of Michigan Facility have utilized NBS-II (secondary national neutron standard) as the calibration source in neutron emission rate determinations. The source was not available for this work. The Cf^{252} spontaneous fission neutron source described by Davis (DAV 76) was chosen as the replacement. In order to tie the indium cross section results to NBS-II a set of four cross calibrations were performed with these two sources using the manganese bath. From these data, the Cf^{252} source emission rate was determined.

Table 2.C.5 is a summary of the results of the Cf^{252} calibrations. The NBS-II source strength was taken as 1.174×10^6 neutrons per second (DAV 76) on 6/1/72. Only a minimal decay correction was required for the NBS-II (a Ra-Be(γ,n) source) half life of 1620 years. The major portion of the uncertainties was the 0.5% error associated with the NBS-II emission rate. Other errors similar to those discussed in section 2.C.3b were responsible for the remaining uncertainty.

The final Cf^{252} source strength was calculated as 6.788×10^6 ($\pm$ 0.58%) neutrons per second on 8/21/77. This value was obtained by normalizing the first three calibrations to the fourth and averaging. No error propagation

Table 2.C.5

Cf^{252} - NBS-II Cross Calibration Results

Calibration #	Calibration Date	Time from Calibration #1	Cf^{252} Neutron Source Strength*
1	3/19/76	0.0 years	$9.844 \times 10^6 \pm 0.58\%$
2	3/21/76	0.0055 years	$9.831 \times 10^6 \pm 0.58\%$
3	8/10/77	1.387 years	$6.848 \times 10^6 \pm 0.57\%$
4	8/21/77	1.420 years	$6.796 \times 10^6 \pm 0.58\%$

*Source strengths in units of neutrons/second

was performed here as the 0.5% NBS-II source strength uncertainty was systematic. Instead, the 0.58% error associated with each calibration was also taken for the average. The maximum deviation of the normalized values from the mean was less than 0.1%.

The Cf^{252} source half life was calculated from the calibration data. The result of 2.651 ± 0.042 years compared with an evaluation by Bozorgmanesh (BOZ 76) of 2.638 ± 0.003 years. Although the experimental result with its uncertainty encompasses the evaluation, the Cf^{252} source half life is expected to be slightly longer than the Cf^{252} half life. The source is comprised of two spontaneous fission isotopes, Cf^{252} and the longer lived Cf^{250}. An accounting of the Cf^{250} contribution to the neutron yield of the Cf souce was required and is discussed in the next section.

2.C.4b. Cf^{250} contribution to neutron yield

Table 2.C.6 contains information about the Cf source isotopic composition on the assay date of 11/18/71. Also included in the table are the a, f, and $\bar{\nu}$ values for the four isotopes which make up the source. The quantities are respectively, the decay corrected composition on the source calibration date of 8/21/77, the fraction of decays which give rise to fission neutrons and the average number of neutrons emitted per spontaneous fission.

The ratio of neutron yields from Cf^{250} to Cf^{252} can be written as (subscript "0" refers to Cf^{250} and "2" refers to Cf^{252}):

$$R(t) = \frac{n_0(t)}{n_2(t)} = \frac{(MW_2)(f_0)(\bar{\nu}_0)(a_0)}{(MW_0)(f_2)(\bar{\nu}_2)(a_2)} e^{-t(\lambda_0-\lambda_2)} \qquad 2.C.1$$

$$= \alpha\, e^{-t(\lambda_0-\lambda_2)}$$

where: t = time from 8/21/77 calibration

n(t) = time dependent neutron yield

MW = atomic weight

λ = decay constant

α = proportionality constant

$= 2.65 \times 10^{-3}$ on 8/21/77

The value of α has been calculated from Table 2.C.6 data. It is the fraction of neutrons emitted by the source due to

Table 2.C.6

Cf Source Composition and Decay Data Information

Isotope	% Composition ** (11/18/71)	a	f*	$\bar{\nu}$*	Half life* (years)
Cf-249	6.43	17.43	0.0	-	350.6
Cf-250	12.48	25.21	7.8×10^{-4}	3.53	13.08
Cf-251	3.97	10.83	0.0	-	900.
Cf-252	77.11	46.53	3.092×10^{-2}	3.74	2.638

* Obtained from Lederer (LED 78)

**Source composition assay data from Korman (KOR 79) for this Cf^{252} source (source ID: ULS-94)

where: a = percentage of isotope comprising source on 8/21/77
f = fraction of decays going by spontaneous fission
$\bar{\nu}$ = average number of neutrons per spontaneous fission

the Cf^{250} spontaneous fission contribution. By way of demonstrating the increasing contribution of the Cf^{250}, the value of α calculated during the indium cross section work rose to 0.5% of the total neutron yield.

Defining n(t) as the time dependent neutron yield of the source

$$n(t) = n_0(t) + n_2(t) = n_2(t)(R(t)+1) \qquad 2.C.2$$

with the inital condition on the calibration date

$$n(0) = n_2(t)\ (1+\alpha)e^{\lambda_2 t}$$

gives rise to the normalized neutron yield, N(t)

$$N(t) = \frac{e^{-\lambda_2 t} + e^{-\lambda_0 t}}{1 + \alpha} \qquad 2.C.3$$

Equation 2.C.3 is used to determine the Cf source emission rate at a time, t, after the 8/21/77 calibration date. The equation accounts for the decay of both californium isotopes and consequently, the decay in the neutron yield of the source.

The uncertainty applied to the decay correction result reduced to error propagation for a simple exponential because of the overwhelming contribution of Cf^{252} to the total neutron yeild. The uncertainty in the Cf^{252} half life

was taken as the difference between the experimental value (2.651 years) and the evaluated value (2.638 years). The propagation of this 0.013 year uncertainty over the three years between the original calibration against NBS-II and the photoneutron source calibrations accounted for 0.40% of the total photoneutron source uncertainty of 0.8%. Note that this decay error would be added in quadrature.

2.D. Neutron Energy Spectra

The capture cross section measurements were performed as averages over the neutron energy spectra of the photoneutron sources. In theory, only the kinematic energy spread due to momentum conservation in the (γ,n) reaction gives rise to deviations from monoenergetic spectra. In practice, factors such as gamma and neutron scattering within the source as well as the presence of more than one gamma ray above the (γ,n) reaction threshold results in degraded neutron energy spectra. A computer program that models the neutron and gamma transport in the photoneutron sources was used to calculate the neutron energy spectra. The program is discussed in section 6.A and only the results of the calculations are presented here. Figure 2.D.1 contains the neutron energy distributions for all four photoneutron sources.

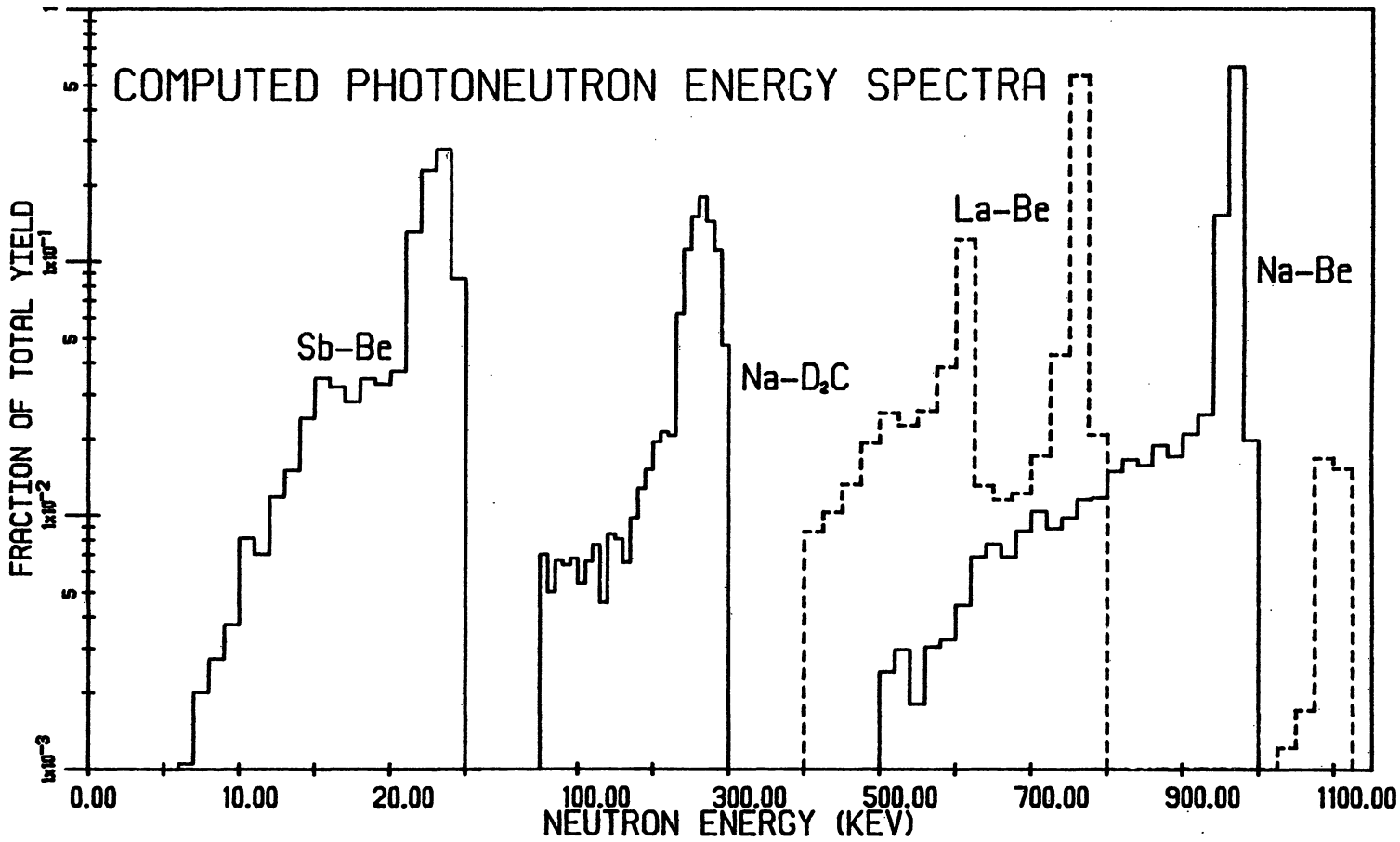

2.D.1. Photoneutron Energy Distributions as Calculated by VES

CHAPTER 3

INDIUM FOIL ACTIVATION

A set of eight indium target foils were fabricated from high purity indium ribbon using a precision punch and die set. Photoneutron source and indium foil positioning devices were designed to minimize uncertainty in the source-target spacings and orientations. Dial gauge and gauge blocks were used in the source-target spacing measurements. Indium foil activations at up to seven different source-target spacings were performed for each source. This strategy facilitated the determination of the room-return contribution to the total In^{116m} saturated activity.

3.A. Indium Target Foil Preparation

A set of eight indium foils were prepared for these capture cross section measurements, one foil for each of the seven source-target spacings plus a spare that would also be used for the general spectrum correction measurements. An indium ribbon of 0.0127 cm thickness and 2.54 cm width was obtained from the Materials Research Corporation for the target foil preparation. A metallic purity of 99.999+% was quoted (from emission spectroscopy analyses).

The two major contaminants were lead and tin having concentrations not exceeding 4 and 3 ppm respectively. Both short term and long term neutron activation analysis by Rigot (RIG 80) showed no detectable gamma emitting impurities.

Preliminary work using absolute gamma counting on a Ge(Li) detector resulted in a beta detector efficiency for In^{116m} decay of 0.28 using 2 cm diameter foils punched from the original indium ribbon. An adjustment of 15% to this efficiency value was estimated for the decay spectrum correction factor discussed in Chapter 5. Since this was too large a correction, the ribbon was rolled to obtain thinner targets. Higher detector efficiencies and a reduced correction factor were the result. The indium ribbon was rolled to 0.0067 cm, about half the original thickness. As was later determined, the correction factor for the decay spectrum was reduced to a 2% adjustment.

The indium was rolled by placing a 10 cm length of the ribbon between two sheets of paper on top of a flat aluminum plate. A smoothed copper mandrel was used as a roller and an aluminum rod assured fairly even pressure along the length of the ribbon. Sixteen disk-shaped foils were punched from the rolled ribbon using a precision machined punch and die set with diameters of 1.9202 cm and 1.9240 cm, respectively. Resulting foil diameters were taken to be 1.9221 cm, the average of the punch and die

diameters. No direct verification of the diameter was attempted because the indium foils are very soft and malleable.

A Mettler microbalance with a ±20 μg sensitivity was used to weigh the punched foils. The eight foils closest in mass were chosen for the cross section measurements. Table 3.A.1 contains the results of the weighings for the final eight foils.

Table 3.A.1

Target Foil Data

Foil & Spacing Number	Mass (g)	Thickness (cm)	% Mass Deviation
1	0.14194	0.0067	- 1.11
2	0.14000	0.0066	- 2.46
3	0.14000	0.0066	- 2.46
4	0.14702	0.0069	2.42
5	0.14245	0.0067	0.76
6	0.14581	0.0069	1.58
7	0.14452	0.0068	0.68
8	0.14658	0.0069	2.12

Foil Diameter = 1.922 cm

In addition, the average foil thicknesses (calculated from the diameter, mass and indium density of 7.31 g/cm^3) and

the percent mass deviation from the average foil mass have been included.

Each foil was always used for the same spacing number regardless of the neutron source. In addition, the foils were reweighed at the completion of each cross section experiment. Run-to-run variations in foil mass were less than 0.05%. Maximum variations over the duration of the experiment were less than 0.1%, the uncertainty applied to the foil mass determinations.

The beta detector background activity was measured for each foil before every run. Activities from one foil to the next never varied by more than two standard deviations (about 1%) for a given run. No significant change in the foil backgrounds were observed over the duration of the experiments, indicating no build-up of long lived beta activities due to the foil irradiation with the photoneutron sources.

The detector background activity with indium foils in place was about 3% greater than the background with no foils in the detector. Typical background activities with and without foils in the detector were 0.69 ± 0.003 and 0.67 ± 0.003 counts per second, respectively. The 0.02 counts per second difference was attributed to the detection of the natural beta decay of In^{115}. With a half life of 5.1×10^{14} years, the In^{115} beta decay activity for any foil would be about 0.034 Bq. Assuming a detector effi-

ciency for the In^{115} decay of about 0.5 (approximately the same as that for In^{116m}), most of the observed difference in the background can be associated with the In^{115} activity.

3.B. Activation Geometry

3.B.1. Foil and Source Positioning

The closest source surface-target foil separation was approximately three millimeters. Neutron flux calculations at this spacing are very sensitive to small uncertainties in the actual separation. Calculations show that a 0.5% uncertainty in the source center-target surface spacing (referred to as the source-target spacing throughout this work), results in a 1.8% uncertainty in the scalar flux at the closest spacing. This sensitivity places strong emphasis on the need for accurate knowledge of the foil and source positioning.

Ideally, the imaginary line connecting the source center with the foil center should be perpendicular to the plane containing the target foil surface. To minimize source movement and positional uncertainty and to approach the above situation as closely as possible, a source centering and position fixing device was built. In addition, three adjustable foil holder assemblies were built to interchangeably attach to the source positioning device.

Figure 3.B.1 is a photo of the source well, a source on the source positioning device, the three foil holder assemblies, a pair of indium foils (one in position on the left foil holder assembly) and the precision punch used to produce the foils.

The source positioning device as it fits into the source well is diagrammed in figure 3.B.2. The device consists of the aluminum source well end plate, a brass source positioning collar and a stainless steel source positioning ring. Dimensions for each component are included in the figure. The inside radius of the source positioning ring is 1.847 cm for the Sb-Be neutron source and 1.504 cm for the remaining sources. This ring fits snugly into a recessed groove in the upper surface of the positioning collar. The radius of the hole in the positioning ring was calculated from source radii and positioning collar height to guarantee that the source rests on the source well end plate. In addition, the radius is such that there was no more than a 0.005 cm horizontal freedom of movement within the ring.

The entire positioning assembly is attached to the source well with four small screws that thread into the positioning collar. The bottom of the source well is included in figure 3.B.2. Brazed to the top of the source well is a brass flange plate. It serves to secure the entire foil activation assembly to the experimental chamber in which the actual irradiations were performed.

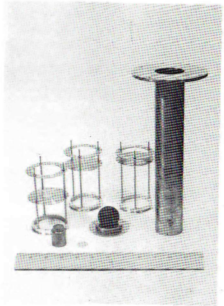

Figure 3.B.1. Indium Foil Activation Assemblies and Photoneutron Source Positioning Devices

49

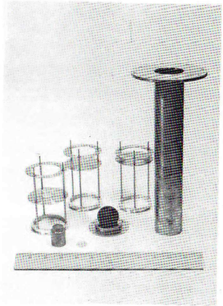

Figure 3.B.1. Indium Foil Activation Assemblies and Photoneutron Source Positioning Devices

49

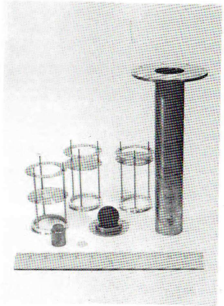

Figure 3.B.1. Indium Foil Activation Assemblies and Photoneutron Source Positioning Devices

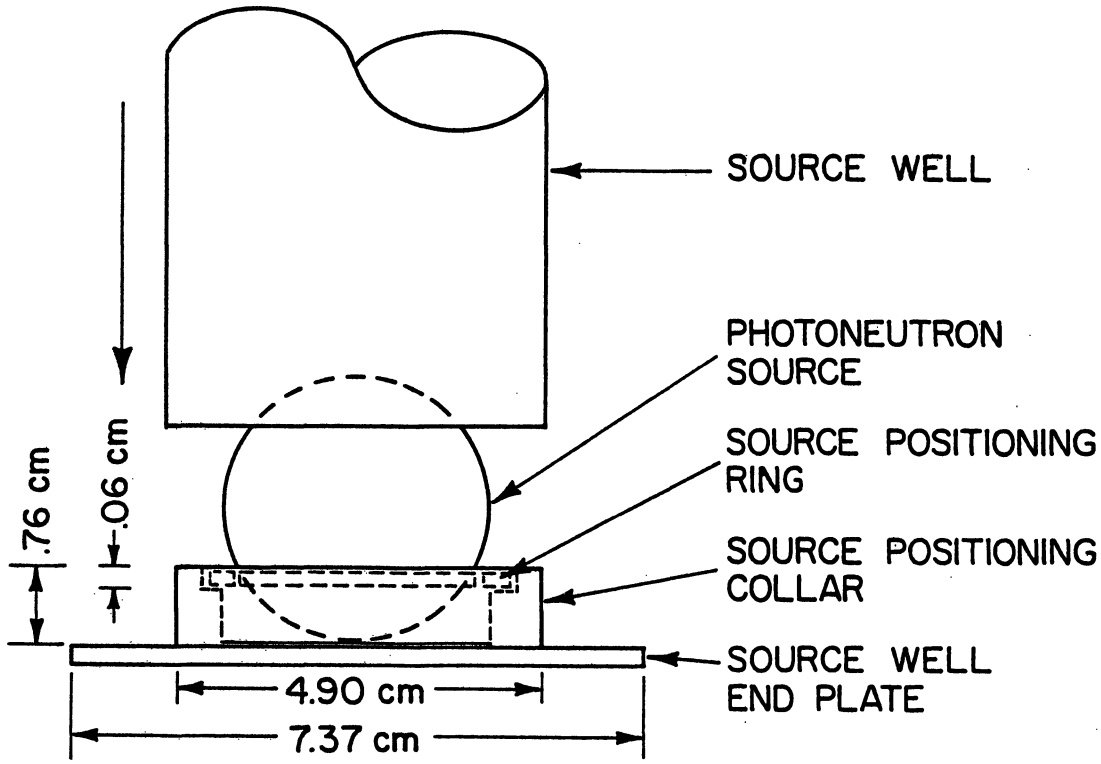

Figure 3.B.2. Source Positioning Device Components

The foil holder assemblies were designed to be structurally rigid, lightweight and easy to re-assemble. Made from stainless steel, these assemblies were composed of the assembly support ring, three threaded rods, two sets of three precision machined hollow spacers, the foil holder plate and the aluminum target assembly support collar. A schematic of the assemblies complete with dimensions, is found on figure 3.B.3.

The foil holders were assembled by screwing three, 2-80 threaded rods into the support collar. The lower set of hollow spacers were slid onto each rod followed by

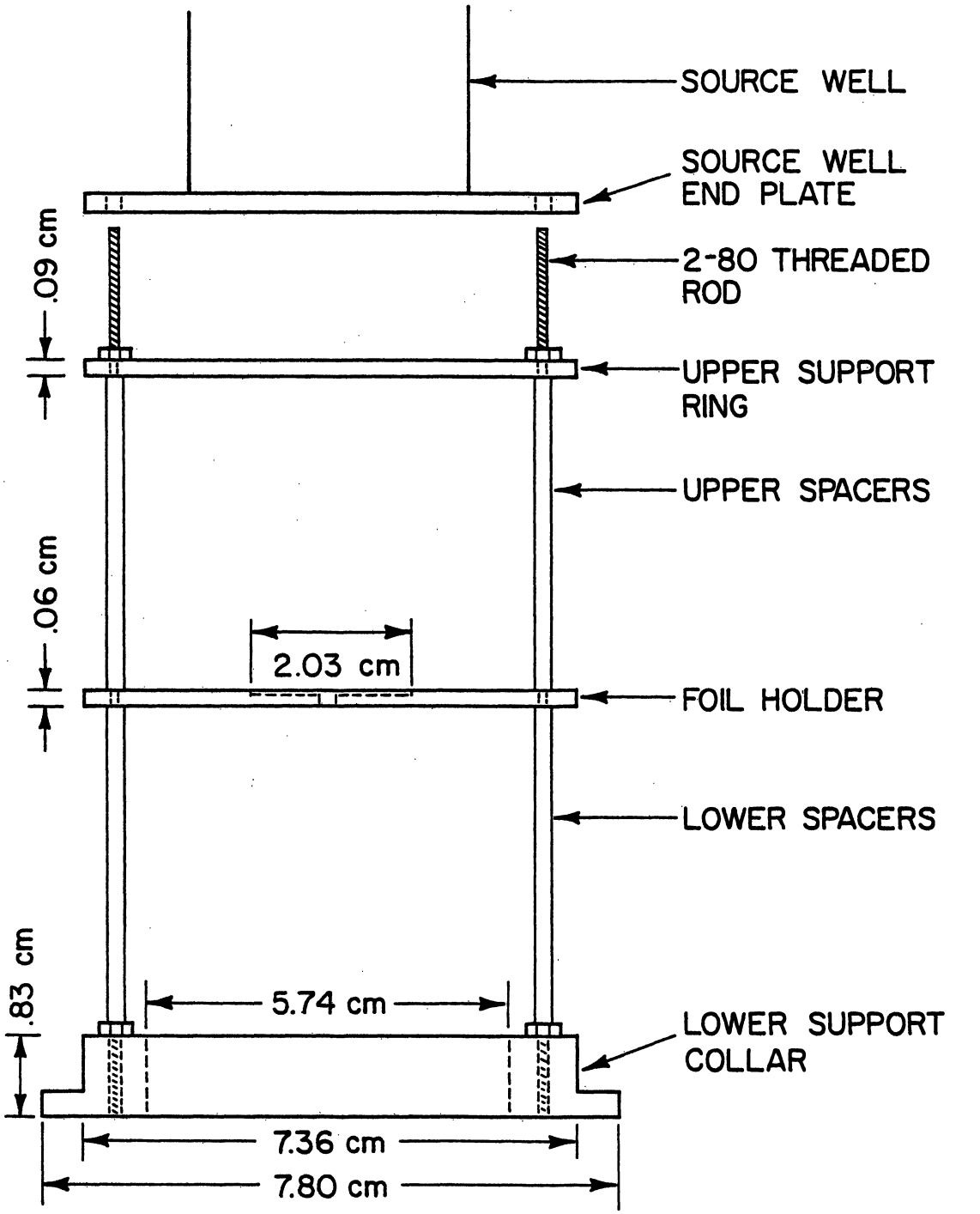

Figure 3.B.3. Foil Assemblies and Attachment to Source Well End Plate

a foil holder plate, the upper set of spacers and the support ring. The whole assembly was then bolted to form the rigid irradiation platform.

Nine sets of three spacers each were made to a tolerance of less than 0.002 cm around the nominal values referred to in Table 3.B.1. A total of eight possible source-target spacings were available with these spacers. In all spacings, the sum of the length of upper spacer and the lower spacer was 10.16 cm. For the actual experiments, individual irradiations were referred to by spacing or foil number. The spacer assignments as a function of spacing number are listed in Table 3.B.1.

Table 3.B.1

Foil Assembly Spacer Assignments

Foil or Spacing Number	Spacer Length (cm) Lower	Upper
1	5.08 + 5.08	-
2	1.27	8.89
3	2.54	7.62
4	3.81	6.35
5	5.08	5.08
6	6.35	3.81
7	7.62	2.54

Spacing number eight was never utilized because the maximum attainable In^{116m} activities were deemed too low to make the effort feasible.

The completed foil holder assembly was attached to the source well end plate by sliding the three threaded rods into the holes in the end plate and bolting them down (see figure 3.B.3). The resulting irradiation configuration has all of the components interconnected. This integral irradiation geometry served to reduce relative source-target positioning uncertainties.

An attempt at as nearly an ideal activation geometry as possible was made by using the source positioning scheme, the foil holder assembly and a special machining jig. The manufacture of the source positioning ring, source positioning collar, source well end plate, target assembly support ring, target foil holder and the target assembly support collar was all performed using a special machining jig. This approach served to provide common centers for all of these components. The ultimate effect was to minimize any deviation from the ideal activation geometry.

3.B.2. Source-Target Spacing Determination

Accurate source-target spacing measurements were required due to the sensitivity of the flux calculation to these values, particularly for the closest spacings.

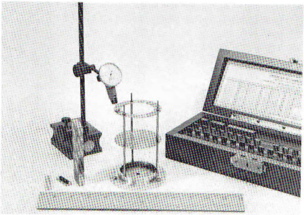

Figure 3.B.4. Dial Gauge and Gauge Blocks Used in the Source-Target Spacing Measurements

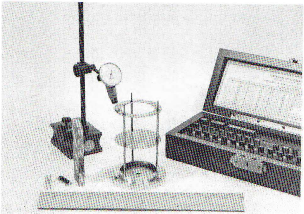

Figure 3.B.4. Dial Gauge and Gauge Blocks Used in the Source-Target Spacing Measurements

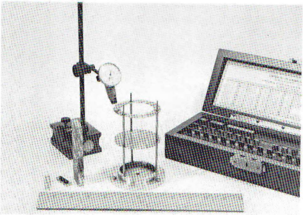

Figure 3.B.4. Dial Gauge and Gauge Blocks Used in the Source-Target Spacing Measurements

These measurements were performed using the dial gauge and precision gauge block set pictured in figure 3.B.4. The source well end plate was removed from the source positioning device and was fastened to the foil holder assembly as it would have been during the activation experiments. The average distance between the end plate and the foil holder depression was determined from measurements at 18 radial positions around the end plate and foil holder. A root mean square deviation was also calculated from these results and was used for the flux sensitivity to source-target spacing uncertainties. Final source-target spacings were obtained by adding the photoneutron source radius to the above mentioned distance. Spacing measurement results and associated RMS uncertainties for all sources and all spacings are summarized in Table 3.B.2.

3.C. Foil Activation

3.C.1. Activation Procedure

The source well with the positioning device attached was placed inside of and fastened to the experiment chamber. Davis (DAV 76) constructed this chamber from a 55 gallon, steel drum and lined the inside with a 0.076 cm thickness of cadmium foil to prevent thermal room-return neutrons from re-entering the chamber. Access to the interior of the chamber was through the removable end plate opening. The entire chamber was suspended by

Table 3.B.2

Source-Target Spacings & RMS Deviations (cm)*

Source	Spacing Number #1	#2	#3	#4	#5	#6	#7
Sb-Be (23 keV)	2.433 (0.001)	3.684 (0.004)	4.969 (0.003)	6.246 (0.004)	7.495 (0.002)	8.754 (0.002)	10.045 (0.003)
Na-D_2C (265 keV)	2.115 (0.003)	3.354 (0.004)	4.650 (0.002)	5.924 (0.007)	7.184 (0.004)	8.434 (0.002)	9.730 (0.003)
La-Be (770 keV)	2.122 (0.002)	3.371 (0.004)	4.663 (0.003)				
Na-Be (964 keV)	2.121 (0.001)	3.366 (0.002)	4.648 (0.001)	5.941 (0.002)	7.195 (0.003)	8.438 (0.002)	9.737 (0.002)

*Values in parentheses are the RMS deviations expressed in cm.

aluminum rods from an inclined track equipped with pulleys and bearings which permitted the remote raising and lowering of the chamber from the source loading point to the center of the low-albedo laboratory in which these experiments were performed. The activations were conducted by placing a foil in the foil holder recess. Foil movement during the irradiation procedure was limited by securing the foil with a small piece of lens cleaning paper and four strips of tape. Once prepared, the foil holder assembly was fastened to the source well end plate, the chamber end plate was replaced to complete the cadmium shield and the entire package was lowered to the floor for the source transfer operation. Figure 3.C.1 is a view of the completed foil activation assembly in the experiment chamber.

Foil activations were performed in The University of Michigan Photoneutron Laboratory. A floor plan of the laboratory can be found in figure 3.C.2. Each activation began by pushing the sliding tray containing the photo-neutron source out of the teletherapy shield, through a cylindrical passage in the 1.3 meter thick shield wall and into the low-albedo lab. From there, the sources were transferred to the source well using vacuum pick-ups at the end of a simple slave manipulator with the aid of a closed-circuit television system. With the source in place, the experimental chamber was raised to the center of the room

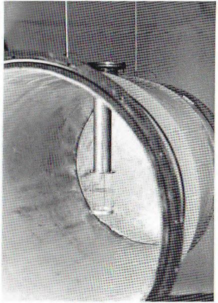

Figure 3.C.1. Foil Activation Assembly in the Experiment Chamber

58

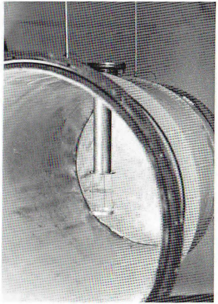

Figure 3.C.1. Foil Activation Assembly in the Experiment Chamber

58

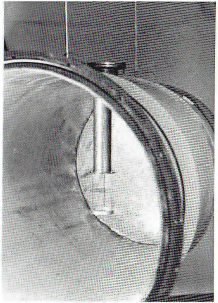

Figure 3.C.1. Foil Activation Assembly in the Experiment Chamber

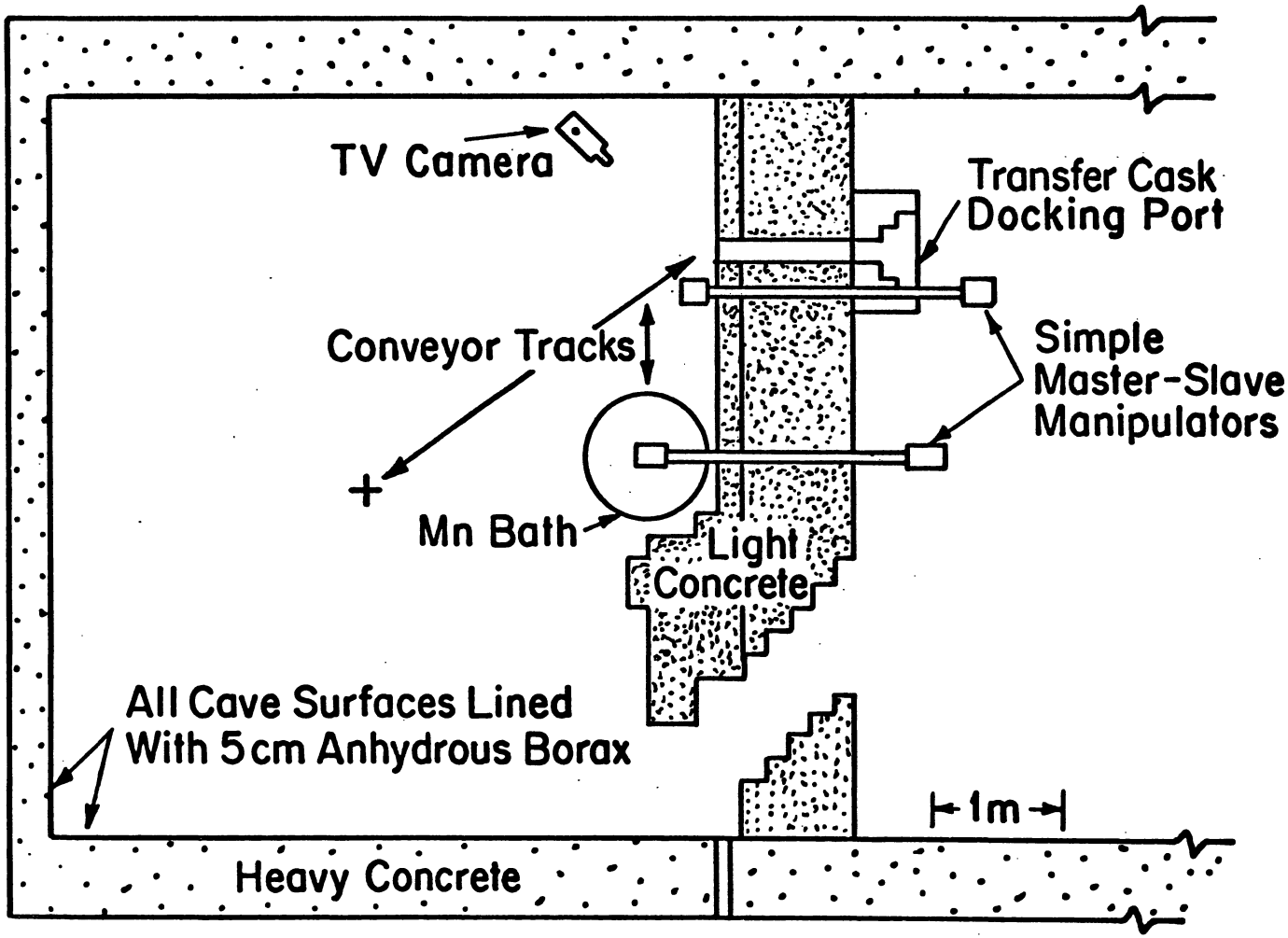

Figure 3.C.2. Floor Plan of the University of Michigan Photoneutron Laboratory

for the duration of the activation. Upon completion of the activation the chamber was lowered and the procedure was reversed. Activation duration was taken as the time from source insertion to the bottom of the source well to source withdrawal from the top of the source well. Transfer times during which the foils were exposed to the source never exceeded ten seconds. Taking solid angle considerations into account, an uncertainty in the activation duration of two second, or less than 0.05%, was assumed. All timing measurements were performed with an electronic stop watch accurate to 0.1 seconds over the term of a cross section measurement, about 16 hours.

Immediately upon completion of one activation, the previous run foil holder assembly was replaced with the next assembly. The new activation was initiated and the freshly irradiated foil was placed in the proportional counter for activity determination.

3.C.2. Activation Strategy

The multiple spacing activation strategy was employed in this work to address the problem of determining the room-return induced In^{116m} activity. Although the low-albedo laboratory walls, floor and ceiling were lined with 5 cm of anhydrous borax to reduce the room scattered flux at the targets, a significant epithermal room-return flux was still present. This flux and the 3300 barn

capture resonance integral of In^{115} resulted in substantial In^{116m} activity. This room-return induced activity accounted for about 20% of the total In^{116m} activity observed at the source-target spacing of 10 cm.

The room-return contribution to the In^{116m} activity was measured by assuming that the room-return flux was spatially flat over the extent of the irradiation spacings. By irradiating a number of foils at various source-target separations, In^{116m} activity from two different sources will be produced. One source will be spacing-dependent (direct source neutrons) and one will be spacing-independent (room-return neutrons). The y-intercept of a plot of the saturated In^{116m} activity per gram of target versus the direct source flux for the seven spacings, is the room-return induced In^{116m} activity.

The approach to the foil activation sequencing was to irradiate the foils starting with the widest source-target spacing and progress to the narrowest. Activation durations were a compromise between maximizing In^{116m} activity and minimizing the production of competing reaction activities, with the general constraint of a decaying neutron source strength. The primary competing reaction was $In^{115}(n,n')In^{115m}$, A neutron energy threshold of 0.35 MeV, however, limited that problem to only the La-Be and Na-Be photoneutron sources. In addition, the In^{115m} half life of 4.486 hours meant that a two hour foil irradiation

produced only 26% of In^{115m} saturated activity as compared with 78% for the In^{116m}. In general, the activation duration for the Sb-Be and Na-Be foils was 1.5 hours and that for the Na-D_2C and La-Be cases was 2.0 hours.

CHAPTER 4

THE 4πβ GAS FLOW PROPORTIONAL COUNTER AND THE FOIL ACTIVITY DETERMINATION

A 4πβ gas flow proportional counter was used to detect beta decay of the In^{116m} activity induced in the target foils by photoneutron irradiation. During the initial performance checkout of the detector, a spurious pulse problem was traced to impurities in the counter flow gas. Several competing reactions were investigated and their contributions to the detected beta activities were removed. The In^{116m} saturated activity with associated uncertainty was calculated at each source-target spacing for all four photoneutron sources.

4.A. Counting System Description

4.A.1. The 4πβ Gas Flow Proportional Counter

The detector is a modification of a National Physical Laboratory design supplied by Robertson (ROB 74). Pictured in figure 4.A.1, the detector consists of two essentially identical halves which are separated by the disk-shaped sample holder. Nearly 100% or 4π geometric efficiency is obtained by sandwiching a target foil on the

Figure 4.A.1. The 4πβ Gas Flow Proportional Counter

Figure 4.A.1. The 4πβ Gas Flow Proportional Counter

Figure 4.A.1. The 4πβ Gas Flow Proportional Counter

sample holder between the two detector halves which are then bolted together. All orifices of the counter, including the one face common to both halves are equipped with rubber O-rings to insure the airtight integrity required for the stable operation of the detector.

Each half of the detector was fabricated from a solid block of copper. Copper was chosen for its high conductivity, ease of machining and low background (concentration of naturally occurring radioactive impurities in copper is low compared with alternative materials). The overall outside dimensions for each half are 11.0 cm x 11.0 cm x 3.5 cm. The inner structure is composed primarily of a pair of aluminum covered, plastic cathodes which serve to shape the cylindrical active volume. Each half of the detector is a distinct counter with its own active volume (3.4 cm diameter by 7.0 cm length) and center anode wire (made of phosphor-bronze).

The sample holder is comprised of three concentric rings. The outer ring is a brass annulus with an outside diameter of 8.89 cm and an inside diameter of 3.81 cm. Six, 0.635 cm diameter holes were drilled into this ring at a radius of about 2.8 cm to permit the flow of counter gas from the bottom half of the detector where it enters, to the top half where it finally leaves the detector. Metal-to-metal contact of the brass sample holder with the copper bulk of the grounded detector is accomplished with the

interface plate, Attached to the bottom half of the detector (on the right in figure 4.A.1), this plate serves both to position the sample holder and to provide the necessary grounding of the entire sample holder assembly.

A 0.012 cm thick, stainless steel annulus with an inside diameter of 2.54 cm snaps into a mitred groove at the inside radius of the brass sample holder. Attached to the bottom surface of this ring is a 6.0 μm thick disk of aluminum foil upon which the activated indium foils are placed for counting. Here again good electrical conductivity from the sample holder to ground has been guaranteed with the use of a conductive adhesive to fasten the aluminum to the stainless steel ring.

The phosphor-bronze anode wire was obtained from Little Falls Alloy Inc. in Paterson, New Jersey. Drawn in precision dies to a diameter of 0.0051 cm, this spring tempered wire was very easy to mount in the detector because of its rigidity and resistance to kinking. The components of the wire mounting assembly in the detector halves are drawn in figure 4.A.2. Piece #1 is the stainless steel shaft of a 26 gauge tuberculin needle. With the point filed off and smoothed, this tube serves the dual role of a field tube and a wire anchor. The anode wire is fed into the needle and through the threaded insulator. The wire is then fed through the second insulator and the copper connector, pieces #3 and #4, respectively. Once

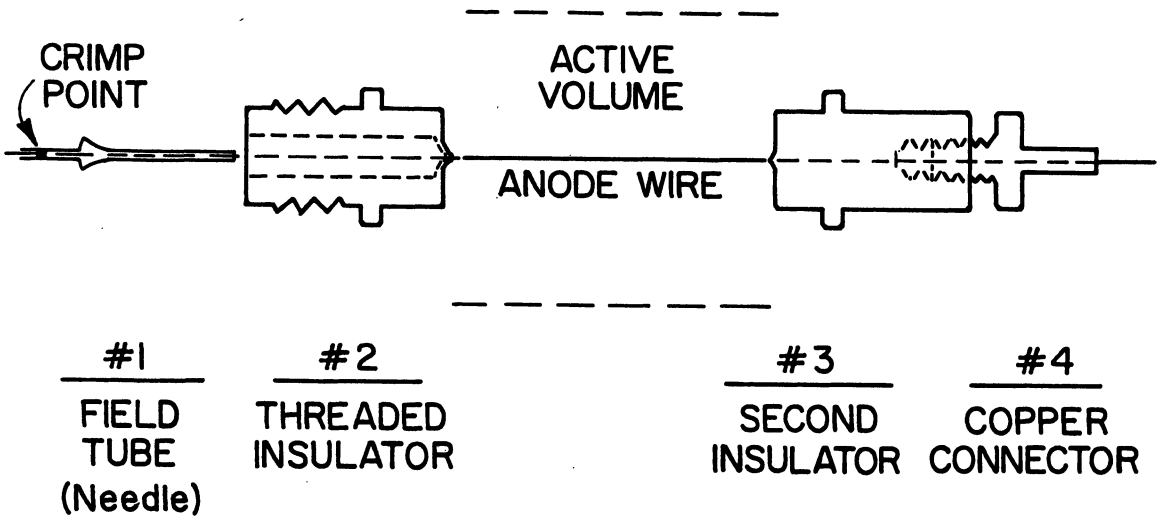

Figure 4.A.2. Anode Mounting Components

threaded through all four components, the field tube is crimped and filed down at the point depicted in the figure. The wire is then pulled to the right until the field tube extends its maximum distance (0.5 cm) into the active volume. The wire is soldered to the copper connector at the front of the detector. The final step of the mounting procedure is the adjustment of the wire position. One of the requirements for constant gas gain in the detector is that the wire be colinear with the active volume cylindrical axis. This was accomplished with the threaded insulator. The insulator was backed off until

adequate tautness of the wire was achieved. Because of the positioning of the insulators, it was assumed that when taut, the wire was colinear with the cylinder axis.

4.A.2. Signal Processing and Recording

A schematic of the detector, its shielding, associated electronics and flow gas supply is found in figure 4.A.3. The detector rests on a lab jack inside a lead shield cube, 50 cm on a side with a wall thickness of 8 cm. A sliding lead door permitted easy access to the shielded detector for sample mounting.

The rest of the detector system was designed to guarantee a stable counting configuration. The detector was used to count events above a minimum pulse height. This integral discrimination mode of operation of the counter and electronic components, required stable gain characteristics. The following expression from Diethorn (DIE 56) demonstrates the gas gain dependence, M, on the gas pressure p, and the high voltage, V.

$$\ln(M) = \frac{V}{\ln(b/a)} \cdot \frac{\ln(2)}{\Delta V} \left[\ln \frac{V}{p \cdot a \cdot \ln(b/a)} - \ln(K) \right] \qquad 4.A.1$$

where: a = anode radius

b = cathode radius

$\Delta V, K$ = constants of the flow gas

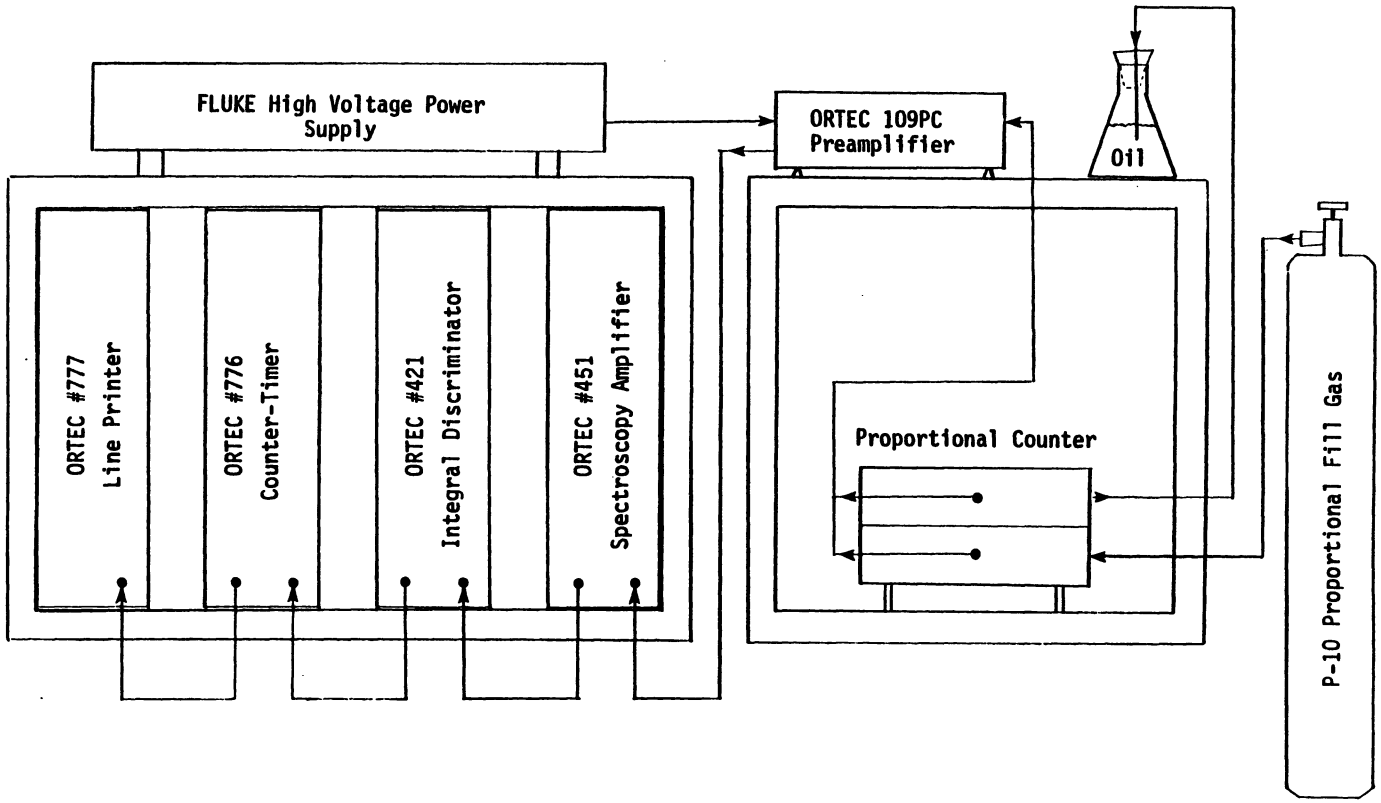

Figure 4.A.3. Schematic of the Beta Detector, Its Shielding, Associated Electronics and P-10 Flow Gas Supply

The maintenance of a stable counting system demanded minimal drifting of the high voltage and the gas pressure.

The high voltage was supplied by a high stability FLUKE power supply through the charge sensitive ORTEC 109PC preamplifier. Detector output pulses were dc coupled from the high voltage at the preamp and were sent to the ORTEC 451 amplifier for pulse shaping and amplification. These pulses were processed by the ORTEC 421 integral discriminator with a 60 mV pulse height threshold. Standard logic output pulses were then counted on the ORTEC 776 scalar-timer. Results of counting for a preset time were printed out on the ORTEC 777 printer.

The flow gas used was P-10, a mixture of 90% argon and 10% methane. Commercially available in high purity, this is a standard gas in flow counter operations. The gas flow is directed from the bottom half of the counter to the top half. Gas pressure control is accomplished through the use of a flask of silicon oil. The end of the gas outlet tube from the top half of the detector is immersed under 4 cm of the oil. The oil maintains the detector pressure just slightly above atmospheric and constant as long as the oil head is held fixed (constant within small variations due to atmospheric pressure variations).

4.B. Detector and Counting System Operation

4.B.1. General Theory of Proportional Counters

The passage of charged particle radiation through a gas results in the production of electron-ion pairs at a cost of about 30 eV to the radiation. If this ionization occurs within the active volume of a cylindrical proportional counter, the electron will be accelerated toward the anode in a radial electric field of

$$\varepsilon(r) = \frac{V}{r \cdot \ln(b/a)} \qquad 4.B.1$$

where: V = applied voltage (positive polarity)

b = cathode radius

a = anode radius

When the field strength exceeds about 10^6 V/m in P-10, the electron energy will be sufficient to cause further ionization of the flow gas. These secondary electrons are in turn accelerated and can initiate further ionization chains. This electron multiplication process is referred to as the Townsend avalanche and is responsible for gas gains or electron multiplication factors of between 10^3 and 10^5.

The electron of each primary electron-ion pair produced by the incident charged particle should be subjected to the same multiplication. Consequently, the charge collected at the anode should be "proportional"

to the energy deposited in the detector active volume. The proportionality means that the detector could be used for energy spectroscopy work. Although energy resolution is typically limited to about 10%, proportional counters are used in a variety of lower energy spectroscopy applications.

A more common application and that of this work is simply the detection of charged particle radiation. Typical electron energies in beta decay range from the keV to a few MeV. Corresponding electron ranges can exceed a meter in P-10 gas at atmospheric pressure. Counter dimensions seldom approach these ranges. Only a fraction of the beta energy will be deposited in the detector. Ideally, with extremely low-noise electronics, a single, primary electron-ion pair could give rise to a detectable pulse. Though probably not this sensitive, the $4\pi\beta$ gas flow proportional counter system of this work is operated on the basis of integral discrimination with a pulse height threshold only slightly above the electronic noise. Any low level losses are expected to be proportional to the count rate and would be accounted for in the detector efficiency determination discussed in Chapter 5.

4.B.2. Performance Characteristics

Before the capture cross section measurements were begun, the performance characteristics of the propor-

tional counter were investigated. Soon after this work began, a spurious pulse problem developed. Background pulses were observed that were too large to discriminate away without adversely affecting the true detector signal. Further experiments pinpointed the source of the problem as impurities in the P-10 flow gas. A more detailed description of the work involved in the investigation of the spurious pulse problem can be found in Appendix C.

The primary check of detector performance is the beta counting plateau curve. This curve was generated after every anode wire change to insure reproducible detector operation. The curve was obtained by measuring the beta count rate as a function of applied voltage for a fixed discriminator level. A small Co^{60} check source was used as the beta source. After some minimum voltage is achieved, the detected count rate should become nearly constant. Theoretically, all betas that interact in the detector active volume are counted once this voltage has been reached. Figure 4.B.1 is a typical plateau curve for the proportional counter. A slight slope of only 0.8% per 100 V is indicative of a very stable counting configuration. Some small slope is expected because of an efficiency increase due to higher electrical field strengths at the source.

The plateau curve results also suggest the best operating voltage for the detector. A train of periodic spurious pulses can follow an actual detector event. These

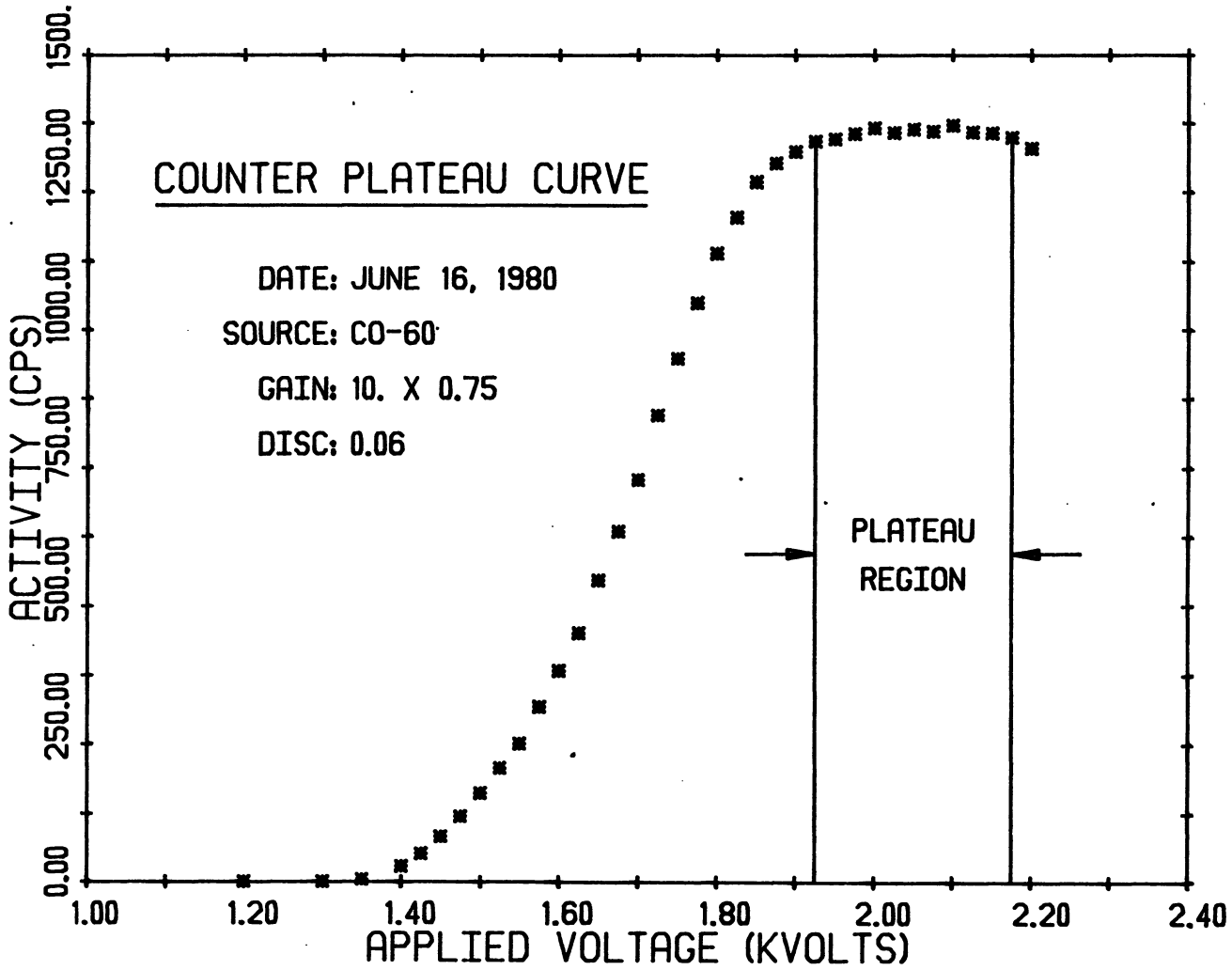

Figure 4.B.1. Typical Proportional Counter Beta Plateau Curve

afterpulses can increase the detected count rate. In proportional counters, this problem manifests itself at the high voltage end of the plateau curve. Operation at or slightly below the center of the plateau is sufficient to reduce the afterpulsing effect to less than 0.01% according to Campion (CAM 73). Based upon the plateau curve results for this detector an operating voltage of 2000 V was selected.

A second important performance characteristic was the detector background. Indium foil activities of less than one count per second were expected. The typical detector background was 0.69 counts per second. In order to make the counting of these low foil activities feasible, a stable background rate was necessary. Day-to-day variations in the background counting rate never exceeded 2% and maximum long term deviations from the mean were always less than 4%. Further reduction of this sensitivity was accomplished with the foil background measurement procedure. The background for the foils with low induced activity were always measured as close to the time of foil activation as possible.

Both short term and long term counting stability was also investigated. The Co^{60} check source activity was recorded once an hour for two months. Short term counting stability was investigated for a number of sixteen hour time segments, the typical counting duration for one cross

section measurement. The standard deviation for each set of sixteen measurements was calculated. The average of ten of these standard deviations was found to be 0.04%. Most of this deviation can be ascribed to counting statistics alone, suggesting very high short term counting stability.

The time between indium foil counting and the detector efficiency measurement was one month. Long term counting stability over this duration was studied by decay correcting many Co^{60} activities back to the first interval. The standard deviation for this set of data was calculated as 0.02%. Again, counting statistics accounts for most of this deviation. The long term counting stability of the detector system was also excellent.

The final characteristic investigated was the differential pulse height spectrum for the In^{116m} beta decay. Plotted in figure 4.B.2, the spectrum was featureless as expected. The pulse height spectrum is the result of the convolution of four different effects:

1. Three predominant beta decay endpoint energies
2. Inherent beta energy spectra
3. Varying source self-absorption
4. Varying energy deposition in the detector active volume.

It is clear that very little information can be obtained from this distribution because of the complex interaction of these four effects.

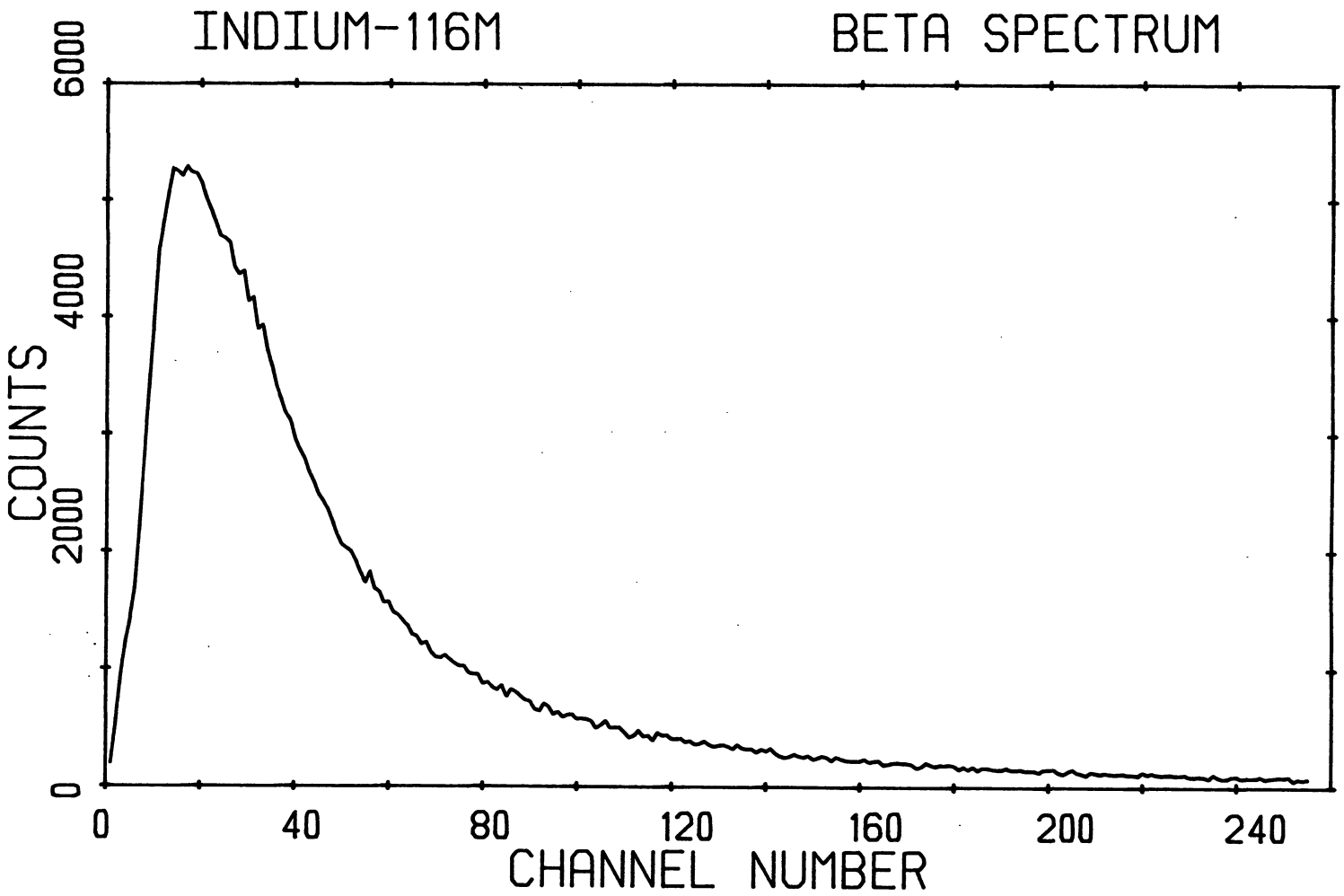

Figure 4.B.2. Differential Pulse Height Spectrum for In^{116m} Beta Decay in the Proportional Counter

4.C. Data Reduction and Error Analysis

4.C.1. Activation Rate Equation

An activity profile for two indium foils during photoneutron irradiation and subsequent counting in the proportional counter is diagrammed on figure 4.C.1. The derivation of the activation rate equation which relates the counts obtained in Δt to the saturated activity of the foil, begins with the differential equation

$$\frac{dN(t)}{dt} = \Sigma \phi_o S_o e^{-\lambda_s t} e^{-\lambda_s T_i} - \lambda N(t) \qquad 4.C.1$$

where: $N(t)$ = time-dependent number of In^{116m} atoms

λ = In^{116m} decay constant

λ_s = photoneutron source decay constant

S_o = neutron source strength at start of first foil activation

T_i = time from start of first foil irradiation to start of the i^{th} foil irradiation

t_o = irradiation duration

t_1 = beginning of counting interval relative to end of irradiation

Δt = counting interval duration

ϕ_o = normalized neutron flux

Σ = macroscopic reaction cross section

t = time from start of i^{th} foil activation.

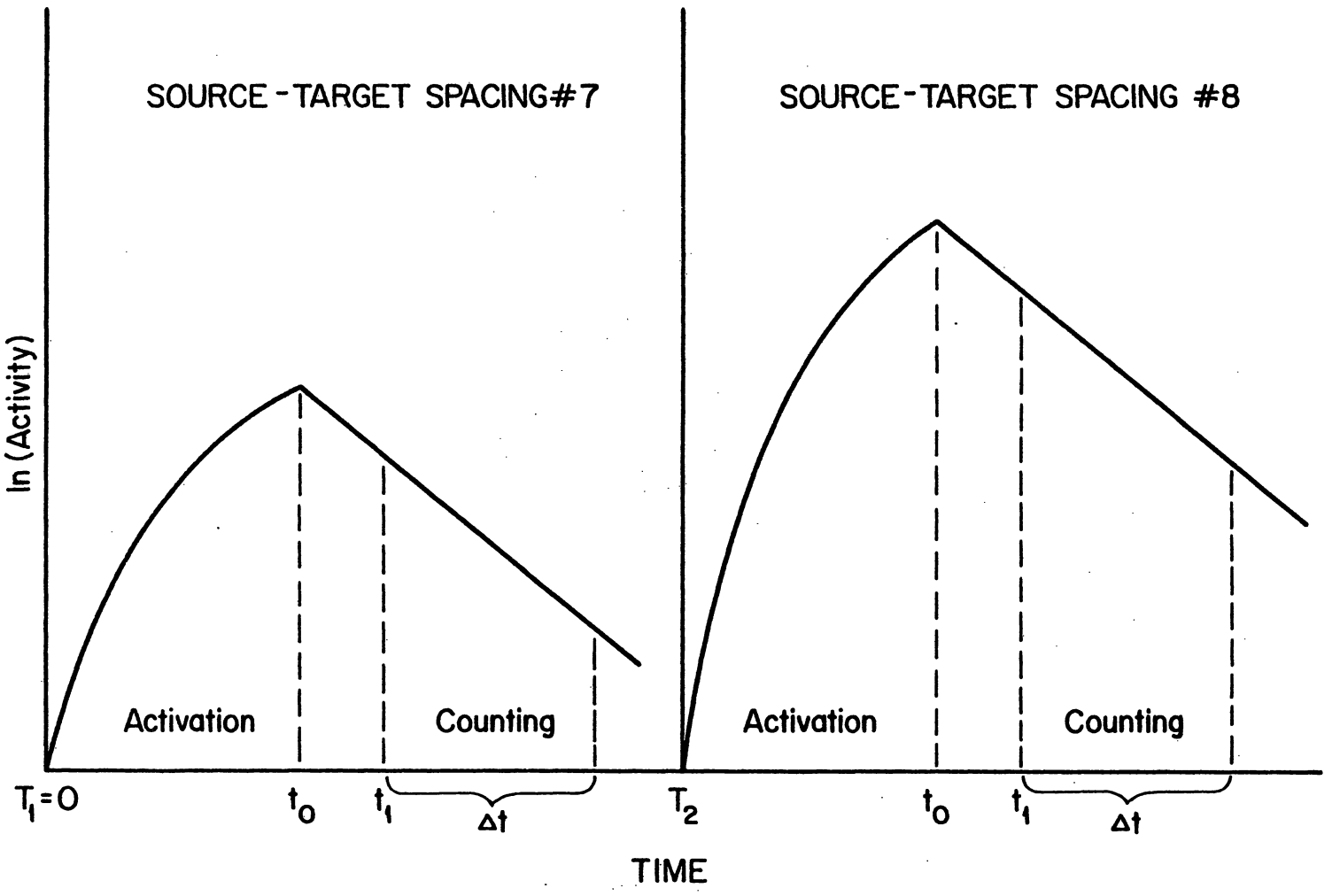

Figure 4.C.1. Indium Foil Activity Profiles

Assuming no initial activity, the expression for the number of counts from a detector with efficiency, ε_β, is:

$$C(\Delta t) = \left[\frac{D\varepsilon_\beta e^{-\lambda_s T_i} e^{-\lambda t_1}}{\lambda - \lambda_s}\right] [e^{-\lambda_s t_o} - e^{-\lambda t_o}][1 - e^{-\lambda \Delta t}] \qquad 4.C.2$$

where: $D = \Sigma \phi_o S_o$ 4.C.3

$C(\Delta t)$ = counts obtained during Δt.

By definition, the saturated activity of the foil, A_∞, is that activity after an infinite irradiation duration with a source of constant strength, S_o. Under these conditions

$$\frac{dN(t=\infty)}{dt} = \lambda_s = 0.$$

As a result, equation 4.C.1 reduces to the expression for the saturated activity

$$A_\infty = \lambda N(t=\infty) = D = \Sigma \phi_o S_o. \qquad 4.C.4$$

Since the indium foil masses are not the same, a more useful quantity than A_∞ is A_∞/N', the saturated activity per target atom. Recalling that

$$N' = \left(\frac{M}{MW}\right) (AN)(F)$$

where: N' = number of target atoms (units of 10^{24})

M = target foil mass

MW = atomic weight (114.82 g for indium)

AN = Avgadro's number

F = fractional isotopic abundance of target atom (0.0428 for In^{113} and 0.9572 for In^{115})

and solving equation 4.C.2 for D, the desired activation rate equation is

$$\frac{A_\infty}{N'} = \frac{C(\Delta t)(\lambda-\lambda_s)(MW)e^{\lambda s T_i} e^{\lambda t_1}}{(M)(AN)(F)(\varepsilon_\beta)[e^{-\lambda s t_o} - e^{-\lambda t_o}][1-e^{-\lambda \Delta t}]} \qquad 4.C.5$$

4.C.2. Competing Reactions

4.C.2a. Reactions, detectable radiations and cross sections

Only neutron induced reactions in In^{113} and In^{115} were investigated because of the high purity of the indium targets. Reaction activity half lives and energy threshold requirements further reduced the list of possible competing reactions. The three reactions and four activities considered were (reaction product half lives in parentheses are from Lederer (LED 78))

1. $In^{113}(n,n')In^{113m}$ (99.47 minutes)

2. $In^{115}(n,n')In^{115m}$ (4.486 hours)

3. $In^{113}(n,\gamma)In^{114m}$ (49.51 days)

IT (96.7%)

In^{114} (71.9 seconds)

For the first three reaction products the predominant decay mode (>95%) is isomeric transition. The proportional counter detection efficiency for these IT gamma rays is sufficiently low that all three activities could normally be disregarded. Unfortunately, all three IT decays are heavily converted. The resulting conversion electrons with energies of 0.355, 0.310 and 0.165 MeV respectively, are readily detectable in the proportional counter. The major In^{114} decay mode is β^- with an endpoint energy of 1.99 MeV, also detectable in the counter.

Cross sections for the two inelastic scattering reactions were obtained from an evaluation by Smith (SMI 76) and experimental work by Smith and Meadows (SMI 75). Neutron energy thresholds of about 0.4 MeV limited the effects of these two reactions to the La-Be and Na-Be sources only. Averaged over the photoneutron energy

spectra, the cross sections for these two reactions are listed in Table 4.C.1.

Table 4.C.1

Competing Reaction Cross Sections

Reaction	Photoneutron Energy (keV) 23	265	770	964
$In^{113}(n,n')In^{113m}$	-	-	11.2 mb	19.3 mb
$In^{115}(n,n')In^{115m}$	-	-	19.9 mb	53.6 mb
$In^{113}(n,\gamma)In^{114m}$	1.0 b	0.3 b	0.3 b	0.3 b

The cross sections for the In^{113} capture reaction were obtained from BNL-325. These values can also be found in Table 4.C.1 and pertain only to the captures which populate the In^{114m} state. Direct capture production of In^{114} is insignificant due to its short half life.

4.C.2b. Beta detector efficiencies

The beta detector efficiency for the In^{115m} decay was measured using absolute gamma counting techniques. An indium foil of the same dimensions as those used in the cross section work was irradiated with a Cf^{252} neutron source. After 15 hours of decay to remove the In^{116m} activity, the foil was counted in the proportional counter and on a Ge(Li) detector system. Using the Lederer (LED 78)

branching ratio of 0.4974 for the 0.336 MeV IT gamma ray, the beta detector efficiency for In^{115m} decay was measured as 0.383.

The contribution of the other three activities combined was an order of magnitude lower than that of In^{115m} due primarily to the low In^{113} natural abundance of 4.28%. Consequently, the detector efficiencies for these three activities were inferred from decay parameters and the In^{116m} detection efficiency result of Chapter 5.

In the calculation of these efficiencies, the beta detector efficiency was assumed to be linearly proportional to the average electron energy. This assumption was based upon the fact that detector inefficiency was due to source self-absorption losses. Since electron range is approximately linear with energy, self-absorption losses were also assumed linear with electron energy. The assumption is fairly crude, but the competing reaction activities are small compared with the In^{116m} activity and large uncertainties were applied to these corrections.

Using the linear efficiency assumption, the beta detector efficiency for the competing activity can be approximated

$$\varepsilon_\beta(\text{Unknown}) = \frac{BR(\text{Unknown})}{BR(In^{116m})} * \frac{\bar{E}_\beta(\text{Unknown})}{\bar{E}_\beta(In^{116m})} * \varepsilon_\beta(In^{116m})$$

where: BR = charged particle branching ratio
= fraction of decays giving rise to an electron, positron or conversion electron
$\bar{E}_\beta$ = average electron energy
$\varepsilon_\beta(In^{116m})$ = nominal beta detector efficiency for In^{116m} decay (0.56 from Chapter 5)

Using the conversion coefficient data and other decay data from Lederer (LED 78), the various efficiency values were calculated and are included in Table 4.C.2.

Table 4.C.2

Beta Detector Efficiency Results for Competing Reactions

Competing Activity	BR	$\bar{E}_\beta$(MeV)	Detector Efficiency
In^{113m}	0.35	0.355	0.28
In^{115m}	0.54	0.310	
-calculated			0.38
-measured			0.383
In^{114m}	0.78	0.165	0.29
In^{114}	0.98	0.660	1.00
In^{116m}	1.00	0.250	0.56

4.C.2c. Counting contributions

The counts associated with each competing reaction for each indium foil counting interval were

calculated using equation 4.C.2. Parameters in the equation not discussed in this chapter have been drawn from results documented in other chapters of this discussion. Flux calculations from Chapters 6 and 7, beta detector efficiencies from Chapter 5, foil masses from Chapter 3 and photoneutron source data from Chapter 2 were used.

The appropriate competing reaction counts and the foil backgrounds were subtracted from the detected counts to obtain just the In^{116m} counts. Table 4.C.3 contains the percent contribution of the various activities to the total counts. These data are taken from spacing #1 results. Extrapolating to the wider source-target spacings, the background fraction increased as the total activity decreased, due to the lower fluxes. The relative contributions of the non-background activities, however, remained about the same.

The uncertainties associated with the competing reaction counts were calculated from uncertainties in the foil efficiencies, flux, half lives, foil masses and cross sections. Uncertainties of 16%, 50%, and 8% of the calculated counts were obtained from the In^{113m}, In^{114m}+In^{114} and In^{115m} activities. These uncertainties were combined with the random statistical uncertainties associated with the background and the total counts to obtain the uncertainty in the calculated In^{116m} count data.

Table 4.C.3

Percent Contribution of the Various Activities to the Total Detected Counts

Activity	Percent Contribution Sb-Be	Na-D_2C	La-Be	Na-Be
In^{113m}	-	-	0.06	0.16
$In^{114m}+In^{114}$	0.02	0.01	0.01	0.01
In^{115m}	-	-	1.91	7.53
Background	2.30	10.50	40.93	3.89
In^{116m}	97.69	89.49	57.10	88.41

4.C.3. In^{116m} Saturated Activity

In section 4.C.2, the total detected counts from the indium foils were reduced to just the In^{116m} counts. Defining the In^{116m} counts as $C(\Delta t)$, equation 4.C.5 was used to calculate the In^{116m} saturated activities. Table 4.C.4 lists the spacing-dependent saturated activities for all four photoneutron sources. These values are A_∞ and not the A_∞/N' values calculated from equation 4.C.5. Although the specific values used in the later room-return corrections are A_∞/N', the A_∞ values in the table are more readily informative.

The uncertainties quoted with the saturated activities are also reported in units of becquerels. These values

Table 4.C.4

In^{116m} Saturated Activity Results (Bq)

Source-Target Spacing #	Sb-Be	Na-D_2C	La-Be	Na-Be
1	165.59±1.96	56.72±0.73	6.062±0.125	148.57±1.84
2	69.61±0.88	20.11±0.32	2.168±0.080	51.85±0.72
3	38.30±0.51	10.21±0.20	1.257±0.063	28.43±0.42
4	25.75±0.38	6.61±0.15	-	18.53±0.29
5	17.91±0.29	4.42±0.11	-	14.15±0.29
6	14.12±0.25	3.32±0.10	-	9.85±0.24
7	12.31±0.22	3.22±0.09	-	7.28±0.18

are based upon the primarily satistical uncertainty in $C(\Delta t)$ (as discussed in section 4.C.2c) and the systematic uncertainties listed in Table 4.C.5.

Table 4.C.5

Systematic Uncertainties in the In^{116m} Saturated Activity Results

Source	Maximum Uncertainty (%)
Half lives:	
- Photoneutron sources	0.1%
- In^{116m}	0.1%
Foil Masses	0.1%
Isotopic Abundance	0.1%
Detector Efficiencies (Table 5.D.2)	1.2%
Irradiation & Counting Timing	0.08%

CHAPTER 5

ABSOLUTE DETECTOR EFFICIENCY DETERMINATION

The absolute detector efficiency of the $4\pi\beta$ proportional counter was determined for each of the eight indium foils. Apparent detector efficiencies were obtained using $4\pi\beta$-γ coincidence counting techniques. A correction to these values was measured to account for the complex nuclear decay scheme effects of In^{116m}. This decay spectrum correction was derived from the results of an efficiency extrapolation experiment. The adjustment of the apparent detector efficiencies by this correction factor produced the absolute detector efficiency values. The internal consistency of the decay spectrum correction was investigated by re-performing the absolute detector efficiency determination using a different gamma channel counting window. Efficiency sensitivities to this activity distribution in the indium foils and foil thickness variations were examined with several experiments.

5.A. General Theory of Coincidence Counting

Coincidence counting is generally considered the most accurate technique for the absolute measurement of

radioactive disintegration rates. It is in theory, applicable to any isotope that decays by the emission of at least two radiation quanta in prompt time coincidence. In practice, however, the basic method is limited to the calibration of radionuclides with simple decay schemes. The In^{116m} decay is complex but the coincidence counting technique can be applied to measure the apparent beta detector efficiency for the decay of this isotope. A correction to this efficiency value for the complex decay scheme effects can then be measured and is the topic of section 5.C.

Consider the simple β-γ decay scheme diagram below:

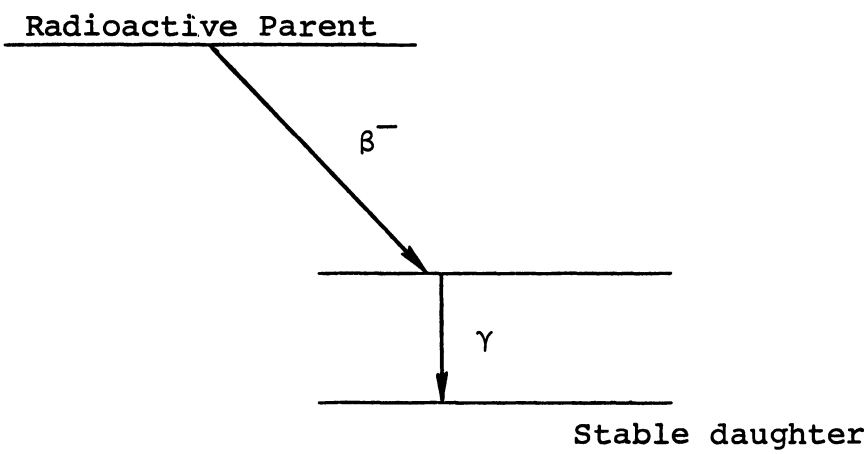

Assume that the beta detector is sensitive to only betas, the gamma detector is sensitive only to gamma rays and the coincidence unit records only simultaneous events from the two detectors. For a source of finite extent, such as the indium foils, the count rates observed from the

three channels (beta, gamma and coincidence) are

$$N_\beta = \bar{\varepsilon}_\beta N_o$$

$$N_\gamma = \bar{\varepsilon}_\gamma N_o \qquad 5.A.1$$

$$N_C = \overline{\varepsilon_\beta \varepsilon_\gamma} N_o$$

where N_o = absolute source disintegration rate

N_β, N_γ, N_C = beta, gamma and coincidence channel count rate

$\bar{\varepsilon}_\beta$ = beta detector efficiency averaged over the foil

$\bar{\varepsilon}_\gamma$ = gamma detector efficiency averaged over the foil

$\overline{\varepsilon_\beta \varepsilon_\gamma}$ = mean product of $\bar{\varepsilon}_\beta$ and $\bar{\varepsilon}_\gamma$ averaged over the foil

Putman (PUT 50) has shown that when at least one detector efficiency is constant over the foil extent, the mean product of the efficiencies is equal to the product of the mean efficiencies (i.e., $\overline{\varepsilon_\beta \varepsilon_\gamma} = \bar{\varepsilon}_\beta \bar{\varepsilon}_\gamma$). This condition can be adequately met with the judicious choice and use of the gamma detector. Equations 5.A.1 can then be reduced to obtain an expression for the beta detector efficiency as:

$$\bar{\varepsilon}_\beta = \frac{N_C}{N_\gamma} \qquad 5.A.2$$

In this expression, N_c and N_γ are assumed to be corrected for dead time, chance coincidence and background effects.

Though derived for the simple β-γ decay scheme and ideal detector response, equation 5.A.2 can be used for the complex decay scheme of In^{116m} and the non-ideal detector system of this work to obtain an estimate of the beta detector efficiency. This estimate will be referred to as the apparent beta detector efficiency, $\varepsilon_{\beta,ap}$. In order to obtain the absolute detector efficiency from $\varepsilon_{\beta,ap}$ corrections for factors such as beta detector sensitivity to gamma rays, conversion electron and auger electron production and γ-γ coincidences must be determined and applied to $\varepsilon_{\beta,ap}$.

5.B. Apparent Beta Detector Efficiency Determination

5.B.1. Coincidence Counting Configuration

Figure 5.B.1 is a block diagram of the electronic components in the $4\pi\beta$-γ coincidence counting system. The gamma channel is based on a NaI(Tℓ) gamma ray detector. The orientation of this detector with respect to the beta detector is depicted in figure 5.B.2. The plastic collar glued to the top half of the proportional counter served to position the two detectors throughout the efficiency measurements. The other components of the gamma channel were a linear amplifier, a single channel analyzer (SCA) and a scalar.

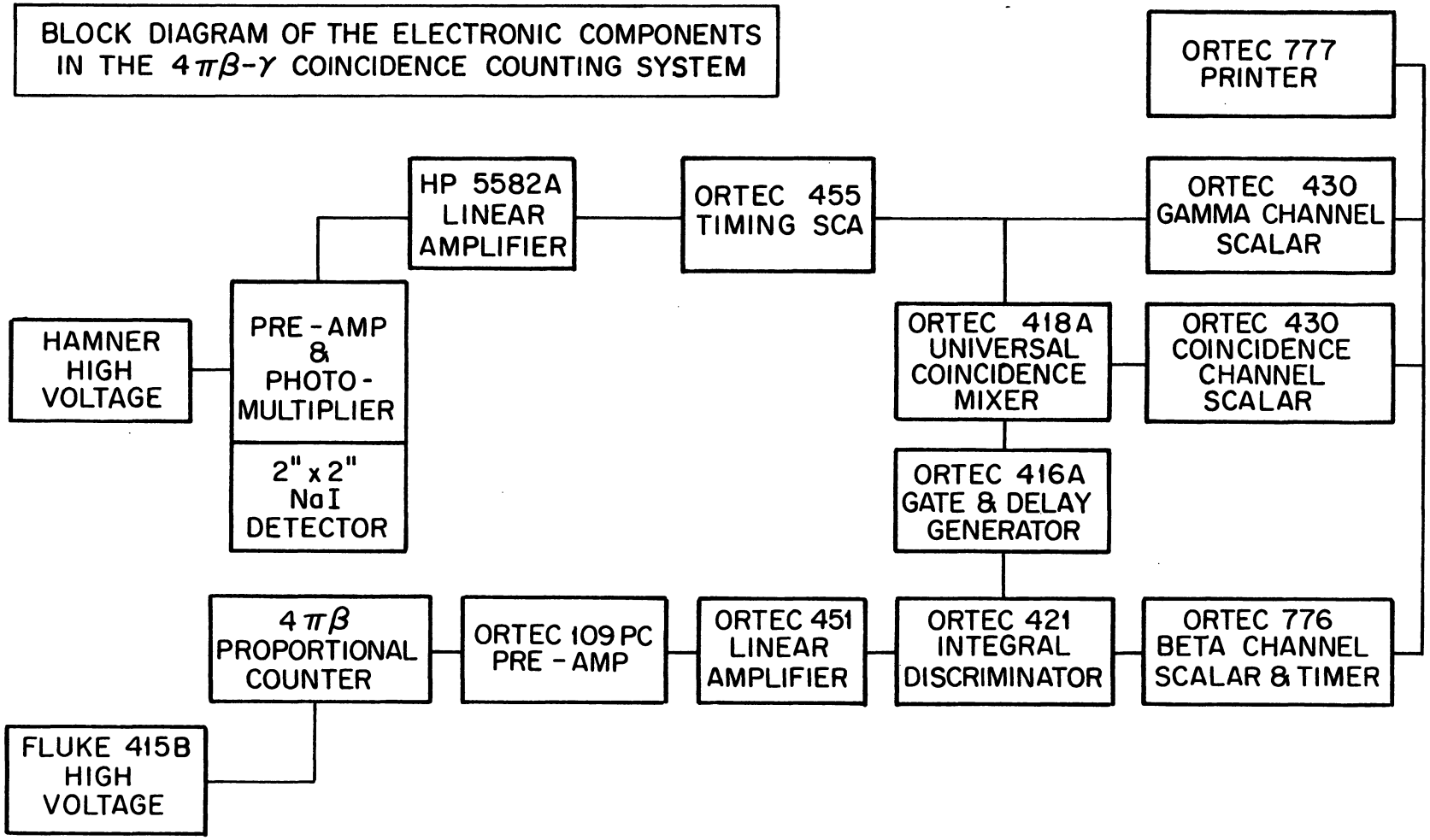

Figure 5.B.1. Block Diagram of the Electronic Components in the 4πβ-γ Coincidence Counting System

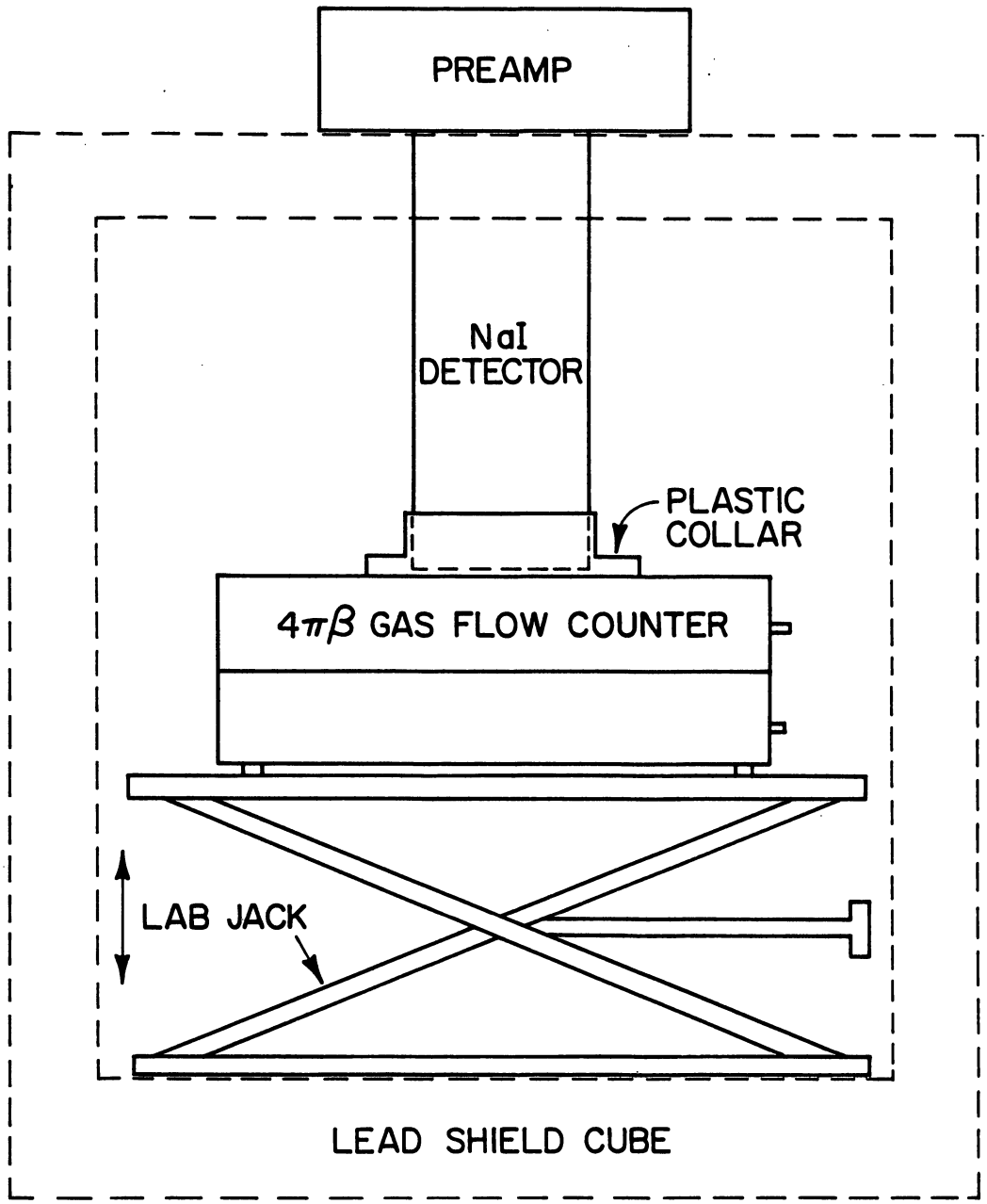

Figure 5.B.2. Beta-Gamma Detectors Orientation

The coincidence electronics consisted of the universal coincidence unit and a scalar. The coincidence mixer is a pulse overlap device. Input logic pulses from the beta and gamma channel discriminators are regenerated into fast rise and falltime current pulses of approximately 2 μs duration. These pulses are fed to an AND circuit that produces an output logic pulse when overlap occurs. These logic pulses are then accumulated in the coincidence channel scalar.

5.B.2. In^{116m} Nuclear Decay Scheme

Figure 5.B.3 is the In^{116m} decay scheme (LED 78). Beta endpoint energies for the three predominant branches are 1.0, 0.87 and 0.60 MeV. No isomeric transition decay has been observed and the K-shell conversion electron emission intensity is less than 1%.

Figure 5.B.4 is the NaI(Tℓ) detector differential pulse height spectrum for In^{116m}. The major peaks and intensities are labeled. All of the apparent beta detector efficiency was performed using the 1.293 MeV gamma photopeak. This gamma ray was chosen because of its high intensity (85% of In^{116m} decays give rise to this gamma ray) and isolation from other photopeaks in the pulse height spectrum (provides for a stable counting window).

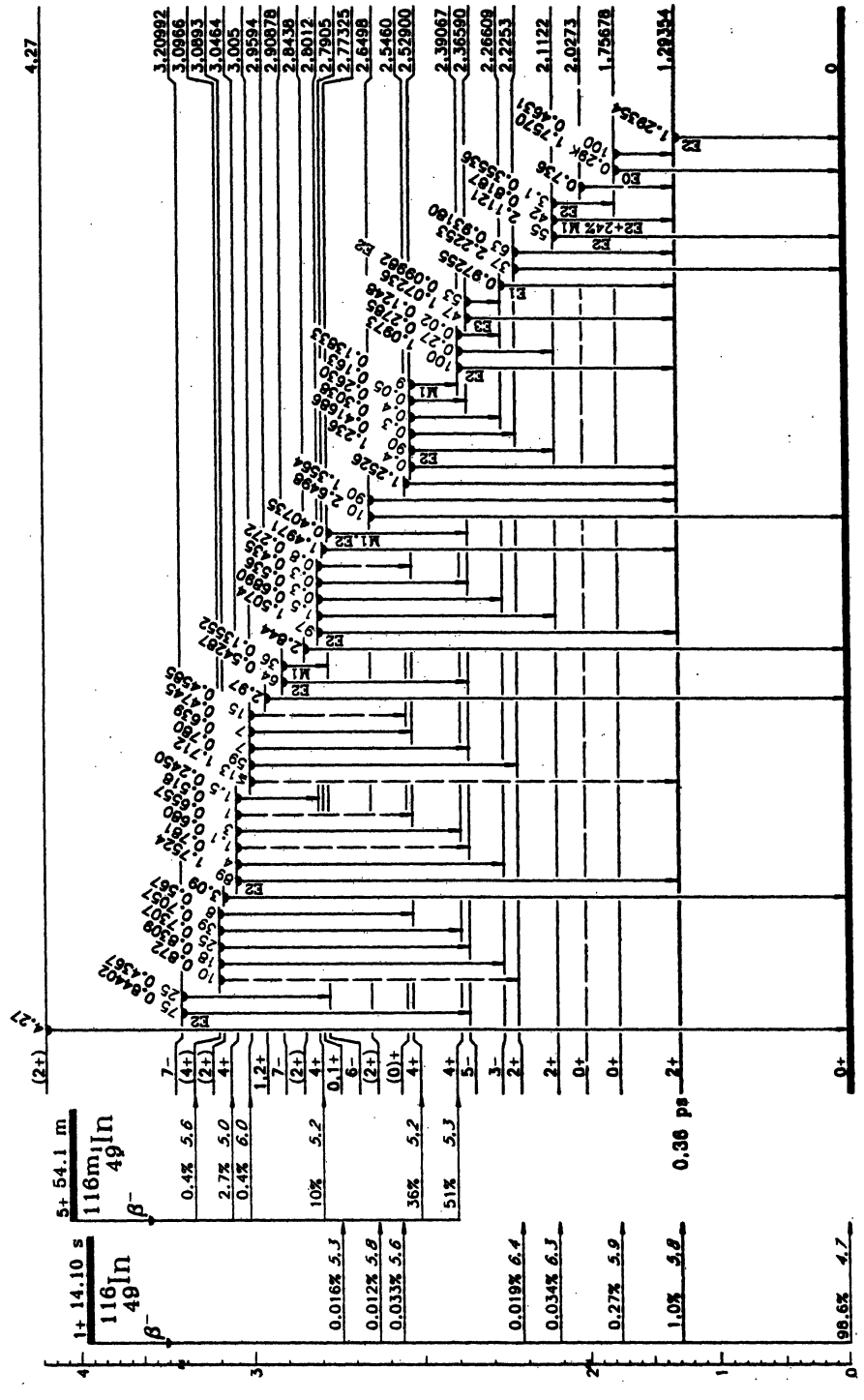

Figure 5.B.3. In^{116m} Nuclear Decay Scheme (LED 78)

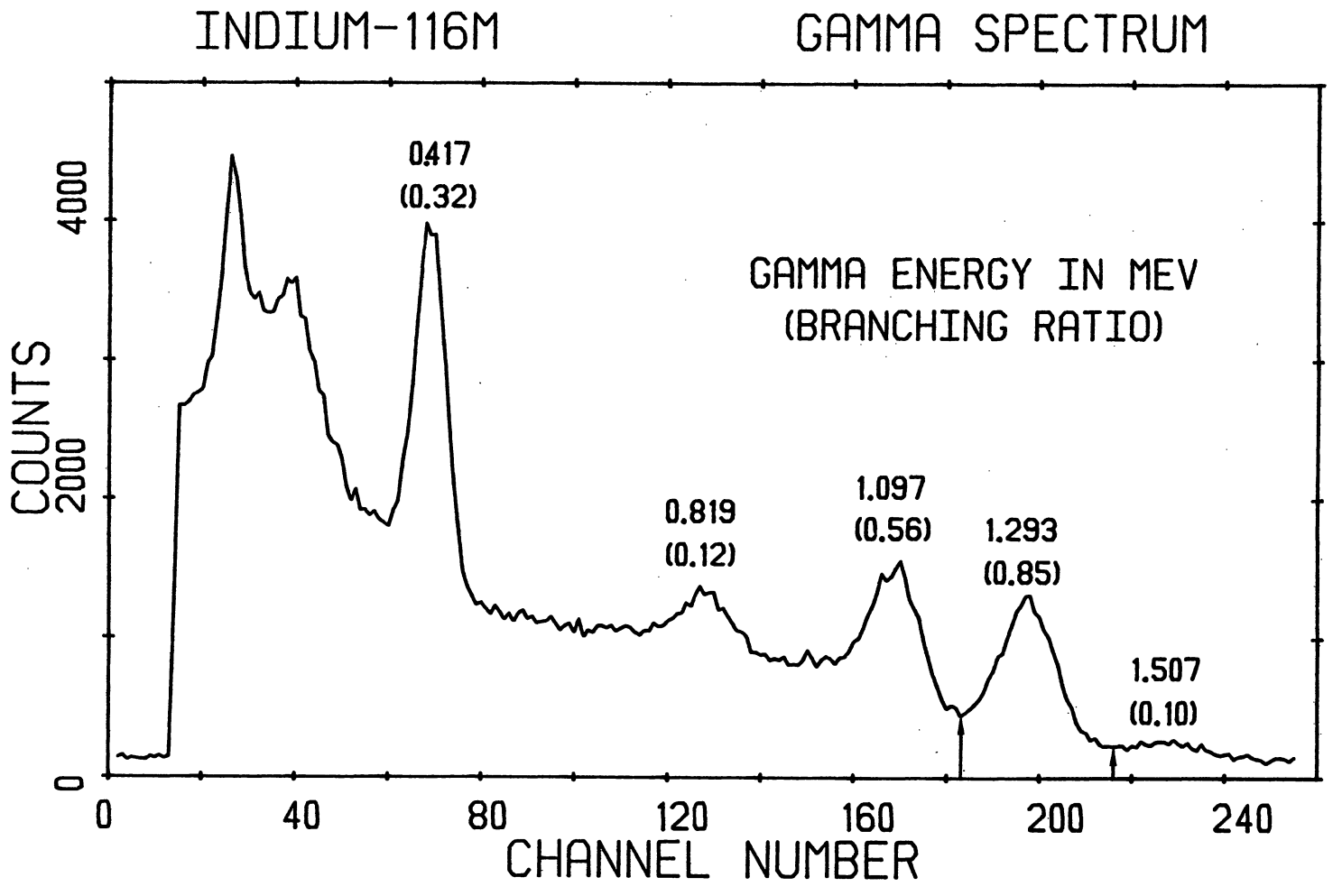

Figure 5.B.4. In^{116m} Differential Pulse Height Spectrum from the NaI Detector

5.B.3. Detector Systems Dead Time Measurements

Both the beta and gamma channel dead times were measured using the source-pulser method discussed in NCRP report #58 (NCR 78). Dead time losses are investigated by first determining the detector count rate for a radioactive source, n_s. A periodic chain of signals from a pulser is then applied to the test input of the preamp and the combined source plus pulser count rate, n_{sp}, is determined. The source is then removed and the pulser count rate, n_p, is measured. The dead time losses are reflected in the difference between n_s+n_p and n_{sp}. The expression for the system dead time, τ, is

$$\tau = \left[1 - \left[1 - \frac{n_s+n_p-n_{sp}}{n_p}\right]^{1/2}\right] \Big/ n_s \qquad 5.B.1$$

This technique assumes that the dead time is non-paralysable and rate independent. The first condition was verified for both detector systems using the decaying source method (KNO 79). The second condition was bypassed by performing the dead time analyses with count rates approximately equal to those encountered in the efficiency experiments. Dead times of 14.6 ± 0.3 and 7.7 ± 0.7 μs were obtained for the beta and gamma channels, respectively. The uncertainties quoted reflect propagation of counting statistics only.

5.B.4. Gamma Channel Counting Windows

Two gamma channel counting windows were used in this work. The first window was used to determine the absolute detector efficiencies for all eight foils. This window consisted of only the 1.293 MeV gamma photopeak, that area between the arrows in the pulse height spectrum of figure 5.B.4. The gamma channel SCA was adjusted to accept only pulses corresponding to this area. The second window contained all of the In^{116m} spectrum above the lower level discriminator of the first window. Only the detector efficiency for foil #8 was determined from the second gamma window.

This two window approach was used to verify the self-consistency of the absolute efficiency determination technique. Apparent beta efficiencies and decay spectrum corrections obtained with the two windows for any given foil (foil #8 in this work) should be different. The resulting absolute efficiencies, however, should be the same.

5.B.5. Coincidence-Delay Curve

Pulses that originate from coincident radiations may not reach the coincidence unit simultaneously due to different inherent pulse processing delays in the beta and gamma channels. A coincidence-delay curve may be measured to determine this fixed delay difference

between the two channels. This curve is obtained by measuring the coincidence count rate as a function of the variable delay inserted into each channel separately. That is, with the variable delay in the gamma channel set at no delay, the coincidence rate is determined as a function of the variable beta channel delay. The same procedure is repeated for no variable delay in the beta channel as the gamma channel variable delay is increased.

The In^{116m} coincidence-delay curve obtained with the first gamma counting window is found on figure 5.B.5. A beta channel delay of 5 μs corresponds to the center of the coincidence counting plateau. This delay was chosen as the operating point for all of the coincidence measurements. It should be noted that the gamma channel lagged the beta channel by only one microsecond. A 4 μs fixed delay was incorporated in the gamma channel to guarantee that the plateau of the coincidence-delay curve could be generated by varying only the beta channel delay.

Chance coincidence rates can be determined from the standard equation

$$N_{ch} = (h_\beta + h_\gamma) N_\beta N_\gamma \qquad 5.B.2$$

where: N_{ch} = chance coincidence rate

h_β, h_γ = current pulse regeneration widths (nominally 2 μs for this work).

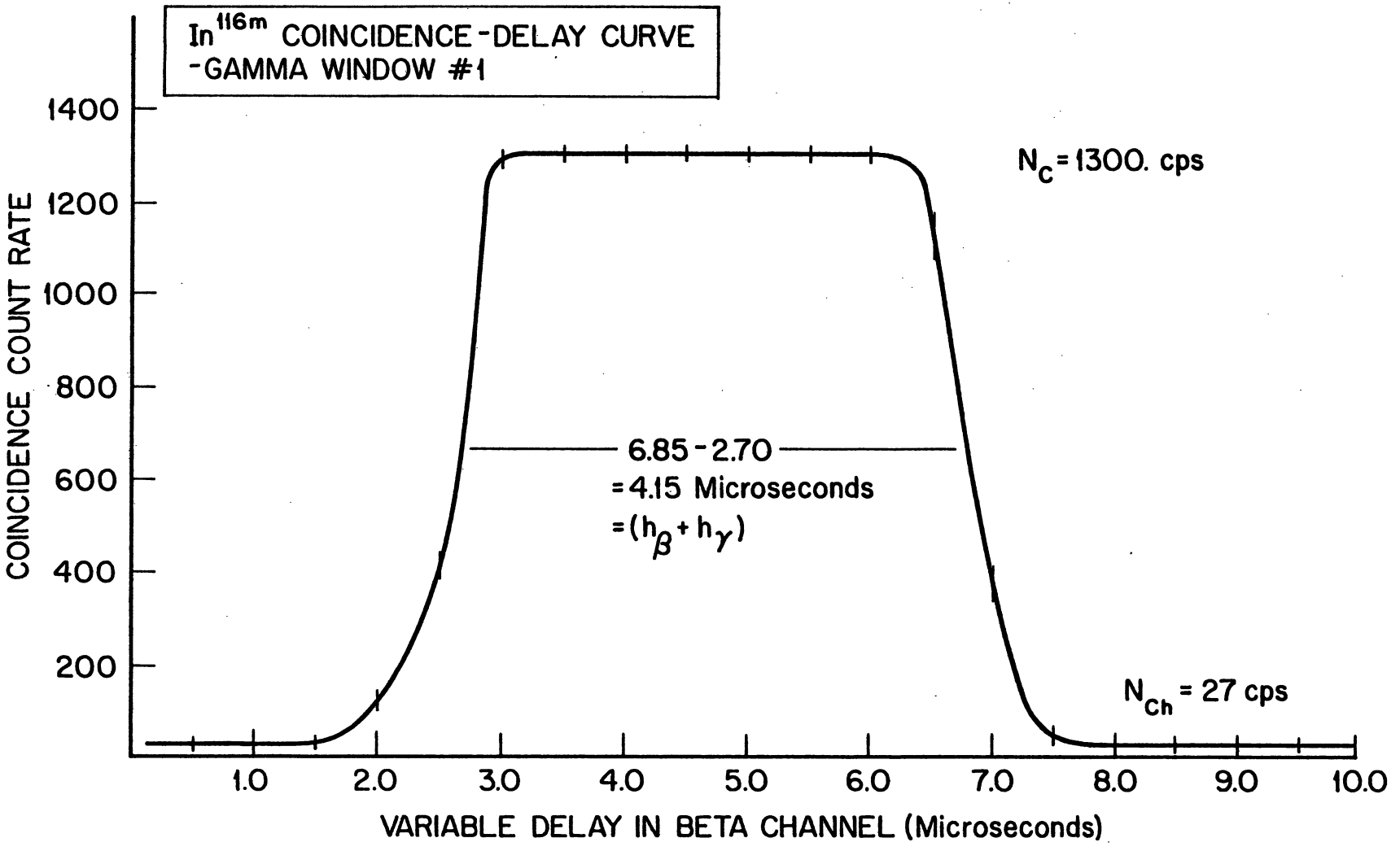

Figure 5.B.5. In^{116m} Coincidence-Decay Curve

An estimate of $(h_\beta + h_\gamma)$ can be taken as the full width at half maximum of the coincidence-delay curve plateau on figure 5.B.5. A more accurate determination can be made by measuring N_c, N_γ and N_β at a delay point on the coincidence-delay curve well away from the plateau. Any coincidences observed at this delay are the result of chance coincidences only. As a result, $N_{ch} = N_c$ here and with N_β and N_γ, equation 5.B.2 can be used to solve for $(h_\beta + h_\gamma)$. The measurement was performed at a beta channel delay of 10 μs. The value of $(h_\beta + h_\gamma)$ was determined as 4.86 ± 0.14 μs. During the coincidence experiments, the N_β and N_γ count rates were measured and the chance coincidence rates were calculated for the above $(h_\beta + h_\gamma)$ value using equation 5.B.2.

5.B.6. Apparent Efficiency Experiments

The indium foils were each irradiated in the 7 cm diameter vertical radiography beam of the Ford Nuclear Reactor. After a five minute irradiation in a thermal flux of 2×10^6 neutrons/cm^2·s and a 20 minute decay period, the activated foil was placed in the proportional counter. Initial count rates of 4000, 100 and 50 counts per second were observed for N_β, N_γ and N_c, respectively. Each foil was counted for 20 minutes in 300 second counting intervals.

5.C. Decay Spectrum Correction Determination

5.C.1. Theoretical Derivation of the Correction

Several decay processes give rise to radiations that are detectable in the proportional counter at the expense of the emission of a coincident gamma ray. As a result, the absolute beta detector efficiency for the In^{116m} decay will be underestimated by the β-γ coincidence experiment discussed in section 5.B. The decay spectrum correction factor is required to account for the non-ideal detector response and the complex decay scheme responsible for this efficiency underestimate.

Derivation of the decay spectrum correction begins with a set of equations analogous to 5.A.1. These count rate equations are functions of decay parameters and several detector efficiencies. Baerg (BAE 66) and Campion (CAM 59) discuss the various factors considered in the development of these equations. These factors can be summarized briefly as:

1. Conversion and auger electron production and detection in the beta detector when the associated beta would not be detected.
2. Gamma sensitivity of the beta detector that gives rise to a beta channel count when the associated beta would not be detected.
3. Complex decay schemes with multiple beta and gamma branches.

For a decay scheme of n beta branches with a branching ratio a_r for the r^{th} branch, the count rate equations are (BAE 66):

$$N_\beta = N_o \sum_{r=1}^{n} a_r \left[\varepsilon_{\beta r} + (1 - \varepsilon_{\beta r}) \left[\frac{\alpha \varepsilon_{ce} + \varepsilon_{\beta\gamma}}{1 + \alpha} \right]_r \right]$$

$$N_\gamma = N_o \sum_{r=1}^{n} a_r \varepsilon_{\gamma r} \qquad 5.C.1$$

$$N_C = N_o \sum_{r=1}^{n} a_r [\varepsilon_{\beta r} \cdot \varepsilon_{\gamma r} + (1 - \varepsilon_{\beta r}) \varepsilon_{cr}]$$

where: $\varepsilon_{\beta r}$ = r^{th} beta branch beta detector efficiency

ε_{ce} = conversion electron detection efficiency of the beta channel

$\varepsilon_{\beta\gamma}$ = intrinsic gamma sensitivity of the beta detector

$\varepsilon_{\gamma r}$ = effective gamma channel efficiency for the detection of a gamma associated with the r^{th} beta branch

ε_{cr} = γ-γ coincidence probability

α_r = r^{th} beta branch internal conversion coefficient

An accurate determination (1% uncertainty) of the absolute beta detector efficiency using these equations directly is not possible for the In^{116m} decay scheme. Large uncer-

tainties or simply a lack of data for most of the parameters in these expressions preclude a brute force approach.

Baerg has shown that for a coincidence counting system utilizing a $4\pi\beta$ gas flow proportional counter, equations 5.C.1 reduce to a simple expression

$$N_\beta = N_o \left[(1-K) + K\frac{N_c}{N_\gamma} \right] \qquad 5.C.2$$

which can also be written as

$$\frac{N_c}{N_\gamma} = \frac{N_\beta}{N_o K} + \left(\frac{K-1}{K}\right) \quad . \qquad 5.C.3$$

The quantity, K, is the decay spectrum correction factor of interest. The value of K is a function of the various beta branch dependent parameters, ε_γ, ε_c, ε_{ce}, and $\varepsilon_{\beta\gamma}$. In practice, the evaluation of K for a specific radioisotope and beta detector system does not require explicit knowledge of these parameters. The only requirement of the efficiency extrapolation experiment used to determine this correction factor is that the efficiency parameters be held constant. An inherent advantage of the $4\pi\beta$ gas proportional counter based coincidence system is that this criterion can be adequately achieved.

5.C.2. Efficiency Extrapolation Experiment

Determination of the decay spectrum correction factor involves the suitable variation of the beta detector efficiency. By artificially altering the efficiency, several sets of N_β, N_γ and N_c count rates can be obtained. Fitting these count rate results to equation 5.C.3 will yield the In^{116m} decay spectrum correction factor, K.

Baerg (BAE 73) points out that the primary criterion for choosing a variation technique is that it should be limited to a form of low-energy beta discrimination. Three possibilities which meet this criterion are:

1. Source self-absorption
2. Foil Absorption
3. Threshold level variation of the integral discriminator.

The third option is in general, limited to pressurized 4π proportional counters because of enhanced beta energy deposition in the detector active volume. Source self-absorption involves activated target foils of various thicknesses. This option was not pursued because of questions concerning uniform distribution of the foil activity. Foil absorption involved the placement of thin, aluminum foils above and below the activated indium foil. Efficiency variation was afforded by progressive attenuation of the beta flux to the detector active volume. This third technique was the one utilized for these extrapola-

tion experiments. A brief discussion of the experimental procedure employed is included here. Recall that two correction factors were measured, one for each of the two gamma windows discussed in section 5.B.4.

Indium foil #8 was irradiated under exactly the same conditions as were the foils in the apparent efficiency experiments of section 5.B.6. The activated foil was placed in the proportional counter and the three count rates were measured under the same counting conditions as in the apparent detector efficiency experiments. Once counted, the indium foil was covered with a 20 μm aluminum absorber foil. The detector was sealed, repositioned with respect to the gamma detector and the three count rates were again recorded. This procedure was repeated with additional aluminum foils alternately placed above and below the foil. In all cases, the absorber foil placement was accomplished without disturbing the indium foil position on the source holder. A total of five absorber foils (3 above and 2 below) were used to achieve a 35% reduction in the beta detector efficiency.

5.D. Data Reduction and Error Analysis

5.D.1. Dead Time Corrections

Corrections for dead time losses in all three counting channels were performed for the data of both the apparent efficiency and the spectrum correction

experiments. The standard equation for non-paralysable dead time behavior

$$n = \frac{m}{1-m\tau_{\beta,\gamma}}$$

where: n = dead time corrected count rate

m = observed count rate

$\tau_{\beta,\gamma}$ = beta or gamma channel dead time

was used for the beta and gamma channels. Justification for using this equation was obtained from results of the decaying source experiments used to determine system dead times. The data from these experiments are plotted in the standard, non-paralysable analysis (KNO 79). The linear slopes displayed in figures 5.D.1 (beta channel results) and 5.D.2 (gamma channel results) are indicative of non-paralysable detector behavior. Similar curves using the paralysable model did not demonstrate the same linear behavior. Maximum dead time corrections of 8% and 1% were observed for the beta and gamma channels, respectively. Uncertainties in the corrected count rates consisted of the dead time uncertainties discussed in section 5.B.3 and random statistical errors in the observed count rates.

Corrections for coincidence channel losses due to the dead time losses of the beta and gamma channels were calculated from expressions obtained by Smith (SMI 78).

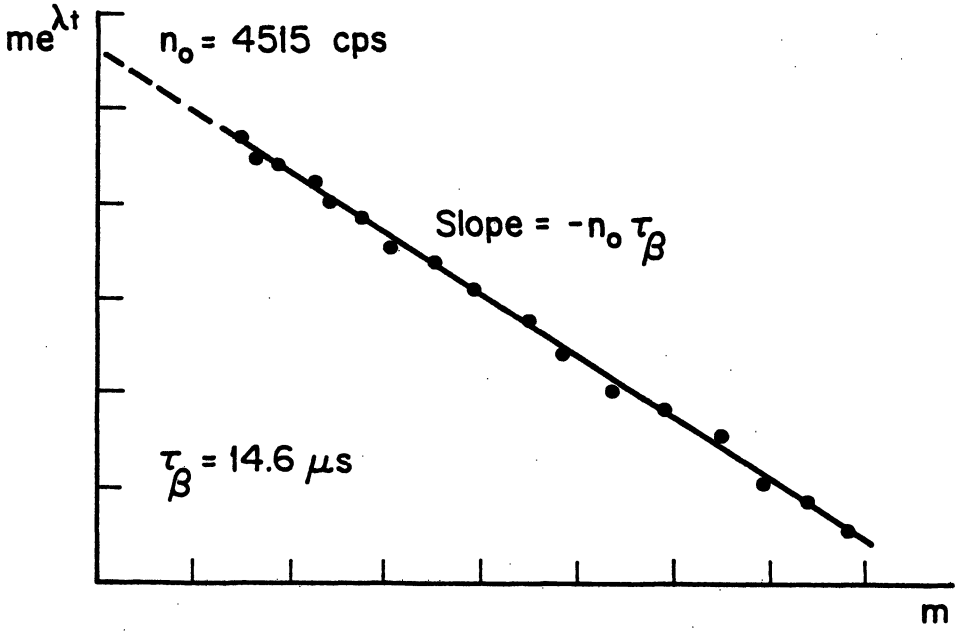

Figure 5.D.1. Decaying Source Analysis of Beta Channel Dead Time

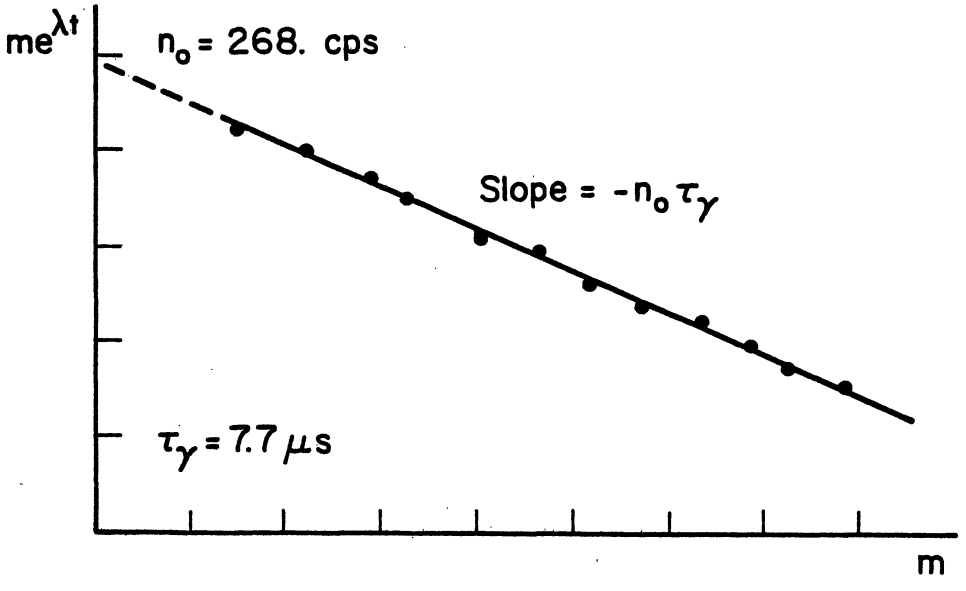

Figure 5.D.2. Decaying Source Analysis of Gamma Channel Dead Time

These equations have not been included here because of their length. Error analysis of these complicated equations was performed by an investigation of parametric dependence. The effects of uncertainties in the coincidence resolving times, beta and gamma channel dead times and count rates on the coincidence channel dead time correction were used to calculate the uncertainty associated with this correction. Maximum coincidence channel corrections were 9%.

5.D.2. Chance Coincidence Corrections

These corrections to the observed coincidence rates were calculated based upon the discussion in section 5.B.5. Uncertainties in the calculated chance rates were due to random statistical uncertainties associated with the beta and gamma channel count rates and the uncertainty (0.14 μs) in the quantity $(h_\beta + h_\gamma)$. Maximum chance rates corrections were about 4% of the total coincidence rates.

5.D.3. Decay Corrections

A basic assumption of the experimental technique to measure K, is that source decay over the course of the measurement is insignificant. Corrections to the beta channel count rates were required because the experiment extended over two In^{116m} half lives. Propagation of

a 0.1% In^{116m} half life uncertainty was the only additional error resulting from this correction.

5.D.4. Apparent Detector Efficiency Results

After correcting the N_β, N_γ and N_c data for dead time, background and chance coincidences, the apparent beta detector efficiency and uncertainty was obtained for each foil from equation 5.A.2.

$$\bar{\varepsilon}_{\beta,ap} = \frac{N_c}{N_\gamma}$$

The results are listed in Table 5.D.1. Uncertainties include those errors discussed for the correction factors, background and random statistics associated with observed counts. Recall that these results (with the exception of foil #8 which was used for both windows) were obtained using the first gamma window or only the 1.293 MeV photopeak.

Figure 5.D.3 is a plot of apparent detector efficiency versus foil mass for the eight target foils. Although some slight scattering is observed, the straight line observed is indicative of the mass-efficiency correlation expected. As foil mass decreases for a fixed diameter, foil thickness decreases and the corresponding efficiency for that foil should increase. The reason for this is that source self-absorption (the primary

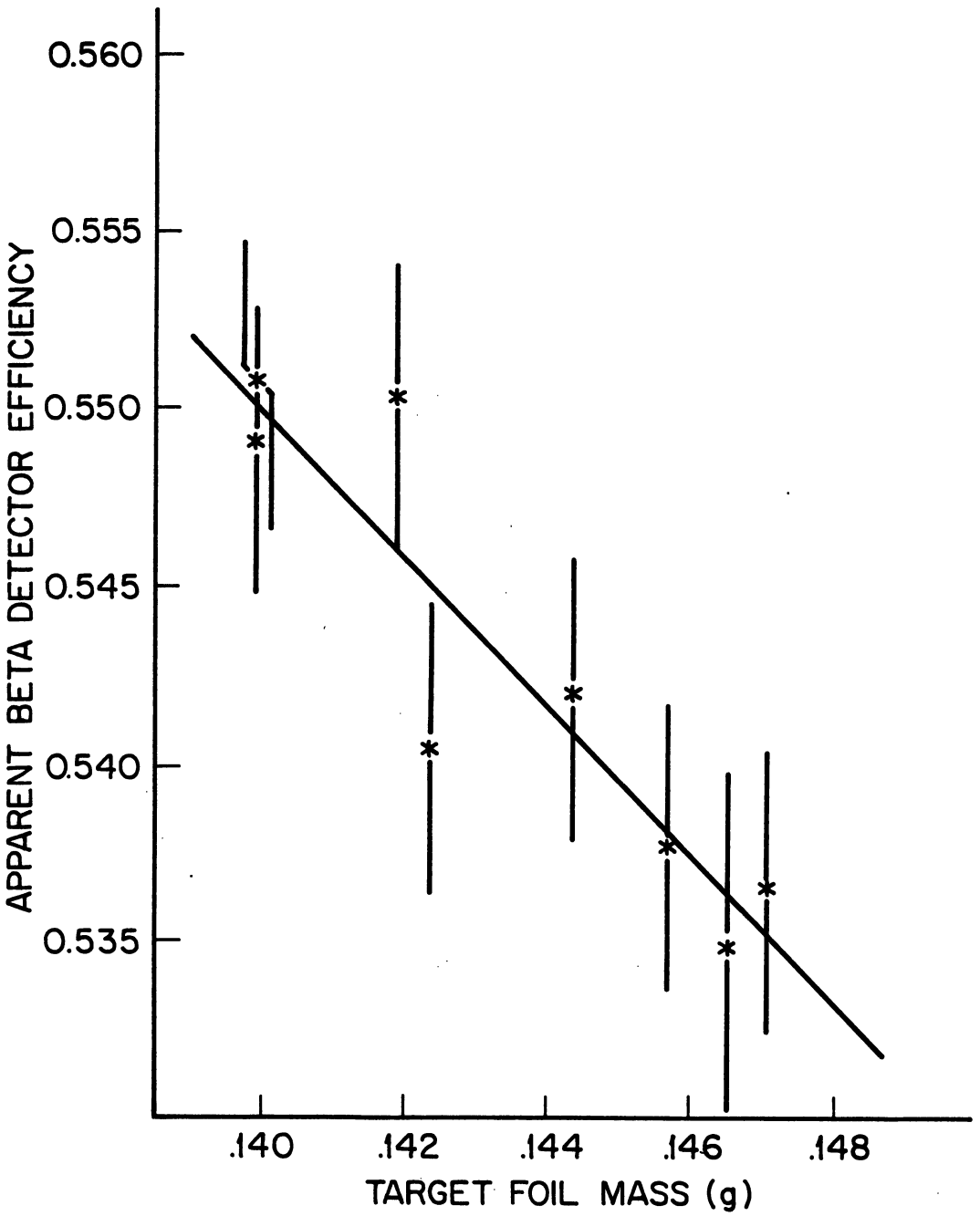

Figure 5.D.3. Detector Efficiency Versus Foil Mass Correlation

Table 5.D.1

Apparent Beta Detector Efficiency Results

Foil #	Efficiency*
1	0.5503 ± 0.0042 (0.76)
2	0.5489 ± 0.0043 (0.78)
3	0.5507 ± 0.0043 (0.78)
4	0.5367 ± 0.0041 (0.76)
5	0.5404 ± 0.0044 (0.81)
6	0.5377 ± 0.0049 (0.91)
7	0.5418 ± 0.0048 (0.89)
8	0.5348 ± 0.0062 (1.16)
8**	0.5247 ± 0.0047 (0.90)

* % errors in parentheses

**Apparent efficiency results obtained using the second gamma window

mechanism responsible for less than unit beta detector efficiency) decreases with decreasing thickness.

5.D.5. Decay Spectrum Correction Results

The decay spectrum correction factor was measured for both gamma windows. The following discussion applied for the analysis associated with each window. Six sets of N_β, N_γ and N_c counting data were obtained from the efficiency extrapolation experiment. All of these data

were first corrected for the appropriate dead time, background, chance coincidence and decay quantities. The $(N_\beta, N_\gamma/N_c)$ ordered pairs required for the graphical analysis of equation 5.C.3 were calculated along with associated uncertainties. A plot of this data for the first window can be found on figure 5.D.4.

A linear least squares regression analysis of the data was used to determine the intercept (K-1)/K. From this, the value of K. the decay spectrum correction factor was calculated. The results for the two gamma windows (#1 and #2 respectively) were 0.974 $\pm$ 0.008 and 0.953 $\pm$ 0.007. Quoted uncertainties include the contributions of the various correction factors, random statistics of the observed count rates and the fitting process used to obtain K from the efficiency variation results.

A significant difference between the two values of K is observed. Since a value of K=1, results in $\varepsilon_\beta = \varepsilon_{\beta,ap}$ (i.e., no decay correction), it is clear that a larger decay spectrum correction is required for the second window apparent efficiency data.

Robertson (ROB 80) measured the K correction value for In^{116m} under detector systems conditions very similar to those of this work. The major difference is that the foil absorption method of efficiency variation was used. Using only the 1.293 MeV gamma ray photopeak (gamma window #1 of this work), the following expression for K was obtained

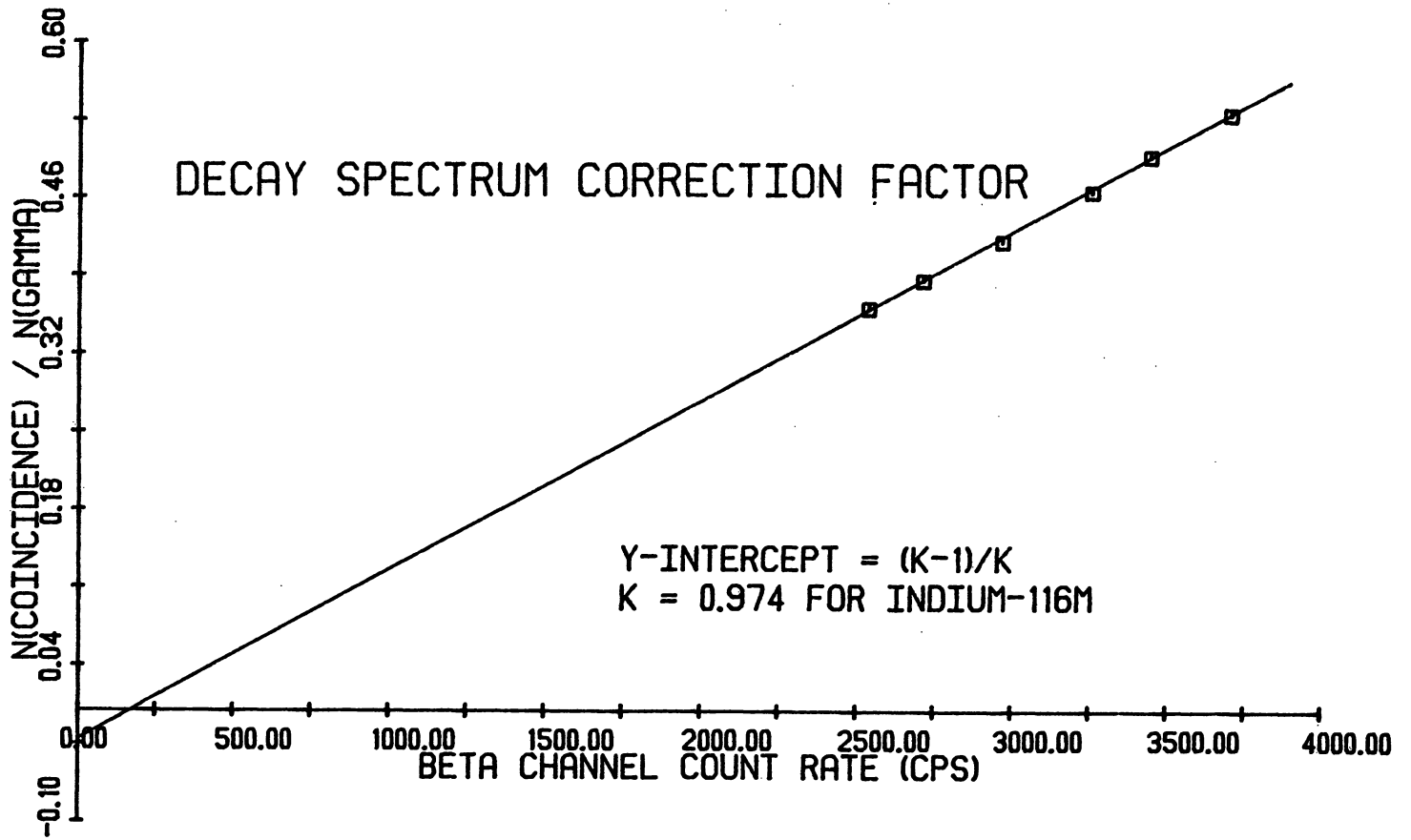

Figure 5.D.4. Decay Spectrum Correction Factor Determination for In^{116m} Using the First Gamma Window Data

$$(1 - K) = (.15)\left[\frac{1-\varepsilon_{\beta,ap}}{\varepsilon_{\beta,ap}}\right] + .007\ (\pm.006) \qquad 5.D.1$$

With the apparent efficiency for foil #8, Robertson's expression gives K = 0.980. The difference of less than 0.6% with the value obtained here is less than the uncertainties associated with either value. Robertson's result serves as independent verification of the result obtained here.

5.D.6. Absolute Beta Detector Efficiency Results

Recalling that

$$\frac{N_c}{N_\gamma} = \varepsilon_{\beta,ap} \qquad \text{and} \qquad \frac{N_\beta}{N_o} = \varepsilon_\beta$$

equation 5.C.3 can be rewritten to solve for the absolute detector efficiency, ε_β,

$$\varepsilon_\beta = 1 + K(\varepsilon_{\beta,ap} - 1). \qquad 5.D.2$$

With this equation, the K values of the last section and the apparent efficiency results in Table 5.D.1, the absolute detector efficiencies were calculated and are found in Table 5.D.2. The uncertainties quoted are the results of propagating K and $\varepsilon_{\beta,ap}$ uncertainties through the manipulations of equation 5.D.2.

Table 5.D.2

Absolute Beta Detector Efficiency Results

Foil #	Efficiency*
1	0.5620 ± 0.0064 (1.13)
2	0.5604 ± 0.0064 (1.14)
3	0.5622 ± 0.0064 (1.13)
4	0.5485 ± 0.0062 (1.13)
5	0.5522 ± 0.0064 (1.16)
6	0.5496 ± 0.0068 (1.23)
7	0.5535 ± 0.0067 (1.21)
8	0.5467 ± 0.0078 (1.42)
8**	0.5469 ± 0.0064 (1.17)

* % errors in parentheses

**Absolute efficiency result obtained using the second gamma window

---

The net effect of the decay spectrum correction factor was a 2% increase in the efficiency. More important, however, was the agreement in the ε_β values of foil #8. Effectively identical, these results atest to the self-consistency of the efficiency extrapolation technique. Work by Baerg (BAE 73) suggests that the two window approach is an effective method for investigating the presence of systematic errors in this efficiency analysis scheme. Although the agreement observed in this work does

not rule out the existance of systematic errors, it does suggest they are small.

An estimate of the systematic uncertainty was made with results of the absolute efficiency determination using Robertson's value of K and the apparent efficiency result of this work. The resulting absolute efficiency for foil #8 was 0.3% lower than the corresponding value in Table 5.D.2. Since Robertson used a different efficiency variation technique (self-absorption), the 0.3% difference mentioned above has been interpreted as the systematic uncertainty associated with the absolute efficiency determination. This contribution has been included in the uncertainties quoted in Table 5.D.2.

CHAPTER 6

NORMALIZED NEUTRON FLUX CALCULATION

A Monte Carlo computer program (VES) was used to model gamma and neutron transport in the photoneutron sources. An analytic expression for the scalar neutron flux averaged over the indium target surface was derived based upon the neutron emission angular distribution results of VES. The sensitivity of the flux calculation to VES related and experiment related uncertainties was investigated. The scalar neutron flux and associated uncertainty was calculated for all of the experimental source-target spacings.

6.A. Computer Model of Photoneutron Source

The only major quantity of the cross section measurements that was not experimentally determined was the normalized neutron flux, that is, the scalar neutron flux for a source emission rate of one neutron per second. Fashioned after the analysis of Davis (DAV 76), this analysis began by calculating the scalar neutron flux due to neutrons emitted from all points on the source surface which could contribute to the flux at a point exterior to the source. This calculation required a knowledge of

the neutron emission angular distribution from an arbitrary point of the source surface. This information was provided by the computer program, VES. Originally developed by Bensch and Vesely (BEN 69), this program models gamma transport, neutron production and neutron transport within the photoneutron source. Modifications of the code by Davis included the addition of two source regions and a substantial increase in the cross section data base library, VESLIB, to handle the complete set of photoneutron sources. Significant reworking, correcting and simplification of the program was performed by Baldwin (BAL 81). A brief description of the program is included here. More detailed discussion can be obtained from the above mentioned references.

VES is a two dimensional, R-θ, Monte Carlo program which follows the gamma and neutron transport histories through the four possible source regions discussed in section 2.A and diagrammed in figure 2.A.1. A particle history begins with the appearance of a gamma ray in this core region. An appropriately determined R_i-θ_i pair is calculated and gamma transport begins. The initial energy is taken as the primary (above the (γ,n) threshold) gamma energy of the core material. The gamma weight is immediately reduced by the large escape probability characteristic of the small physical size of the source. Cross section ratios are calculated for the four regions and

based upon these, a random number generator determines in which region the gamma will interact. The possible interaction mechanisms are:

i. Gamma absorption

ii. Compton scattering using the Klein-Nishina equation with new energy and direction sampled for continued transport

iii. Neutron production via the (γ,n) reaction in region three with reaction anisotropy included

Each process is accounted for by further reduction of the primary gamma weight. A gamma history is terminated when the photon is absorbed, it Compton scatters below the (γ,n) threshold (1.665 MeV for beryllium and 2.225 MeV for deuterium), its weight falls below the minimum value of 5×10^{-7} or when it gives rise to a neutron.

Once a neutron is produced, gamma transport is replaced by the nearly identical neutron transport scheme. The initial weight of the neutron is taken as the weight of the gamma photon which gave rise to it. Again, the escape probability is determined first. For the neutron weight that does escape, both the neutron energy and the cosine of the angle of emission relative to the surface normal are determined. The appropriate energy and angular distribution bins are incremented by the escaped neutron weight. Those neutrons which do not escape are forced to interact within the source. The region of interaction is

determined by cross section ratios with the possible mechanisms being:

i. Neutron absorption

ii. Neutron scattering with reaction anisotropies included in the calculation of new neutron energies and directions

Each process is also accounted for by further reduction of the neutron weight. A neutron history is terminated by neutron absorption, or the reduction of the weight below the minimum of 5×10^{-7}. Scattered neutrons are followed until one of the termination criteria is met or escape occurs. Upon escape, the appropriate neutron energy and angular distribution bins are incremented by the escaped neutron weight.

The output of the VES program contains the neutron emission angular distribution and the neutron energy distribution. In addition, regionwise scattering and absorption information for both gammas and neutrons are included.

VES was run for the four photoneutron sources employed in this work. The two distributions were obtained from the Monte Carlo code by following 34440 primary gamma histories per source. A histogram plot of the resulting emission angular distribution for the Na-Be photoneutron source is found in figure 6.A.1. The neutron energy distributions for all four sources are consolidated in figure 2.D.1. Finally, Table 6.A.1 is a summary of the photo-

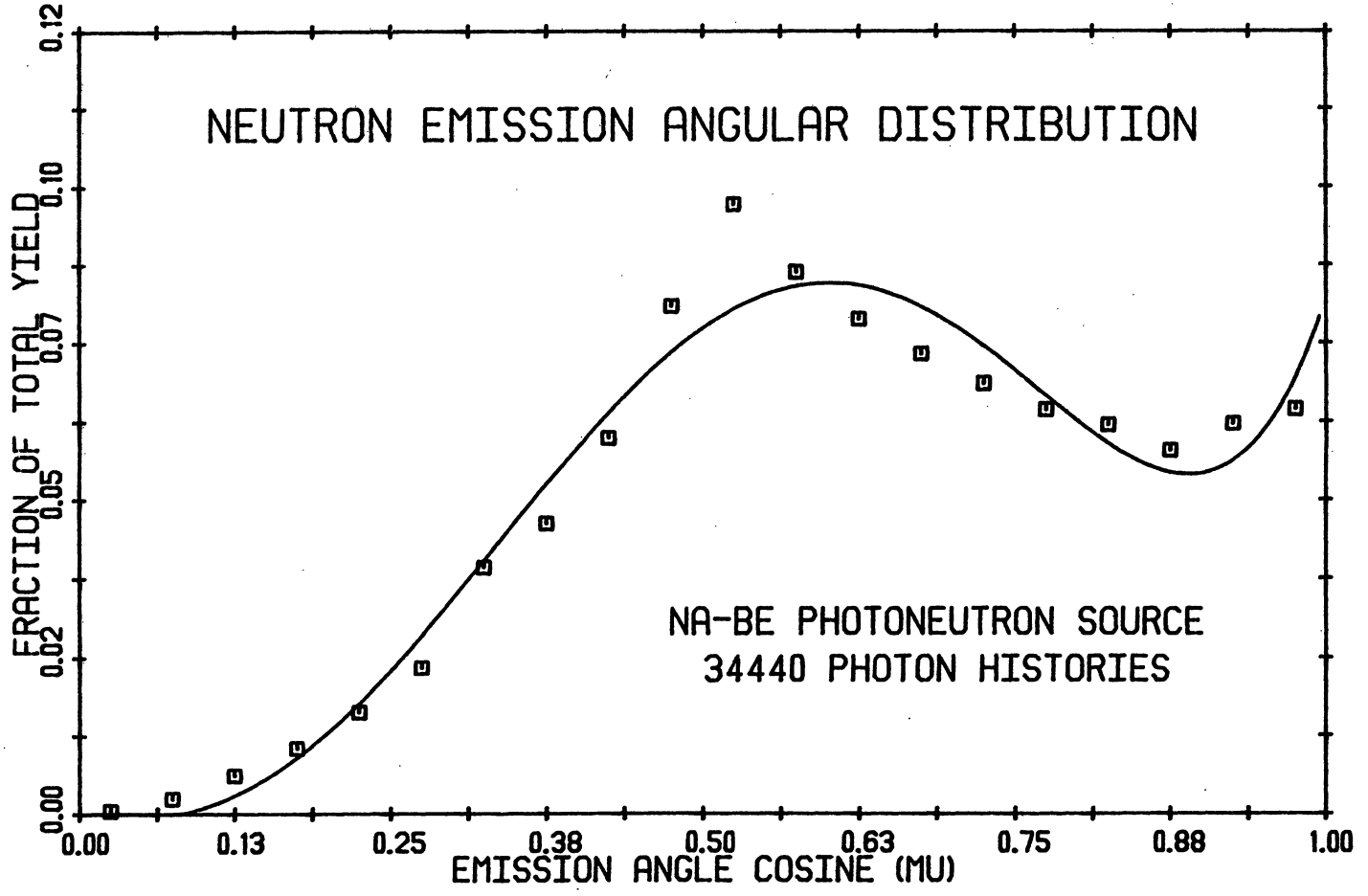

Figure 6.A.1. Neutron Emission Angular Distribution Obtained from the VES Monte Carlo Program for the Na-Be Photoneutron Source

neutron production efficiency for the four sources. The efficiency is defined as the ratio of neutrons produced to the number of gamma histories investigated. In addition, the table includes the percentage of neutrons which suffer at least one scatter within the source.

Table 6.A.1

Photoneutron Production Efficiency

Source	Energy (keV)	Efficiency ($\times 10^{-4}$)	Percent Scattered
Sb-Be	23	0.4306	38.41
Na-D_2C	265	0.3364	24.82
La-Be	770	0.1750	29.85
Na-Be	964	0.2700	26.75

6.B. Derivation of Flux Expression

The objective of this derivation was an analytic expression for the scalar flux per unit source strength averaged over the surface area of the target foil. The calculation was performed by integrating the neutron emission angular distribution, $F(\mu)$, from all points on the source surface that contributed to the flux at a point a distance "Z" away from the source center. The resulting scalar flux, $\phi(Z)$, was then averaged over the indium target to obtain $\bar{\phi}_A$. The calculation assumed one-speed neutron streaming in a vacuum so that inscatter and attenuation

considerations must be treated as additional corrections. The geometry of this flux calculation and the variables of interest are depicted in figure 6.B.1.

The neutron emission distribution from an arbitrary point on the source surface with respect to the surface normal can be described as:

$$\phi(\mu,\psi,S)\ d\mu\ d\psi\ dS$$

This quantity is the number of neutrons emitted in $d\mu$ about μ, $d\psi$ about ψ from the differential source surface element dS at S, per unit source strength. Here μ is the cosine of the angle between the neutron emission direction and the surface normal and ψ is the azimuthal rotation angle about the normal. The normalized scalar flux at a distance Z, is simply the integration of $\phi(\mu,\psi,S)$ over the three dependent variables with proper weighting for $1/r^2$ solid angle spreading. Here "r" is the distance from the source point dS, to the point at Z.

The spherical symmetry of this problem permits the following simplification:

$$\phi(\mu,\psi,S) = \frac{\phi(\mu,\psi)}{4\pi R_s^2} = \frac{\phi(\mu)}{(2\pi)(4\pi R_s^2)} \qquad 6.B.1$$

where R_s is the photoneutron source radius. $\phi(\mu)$ is the

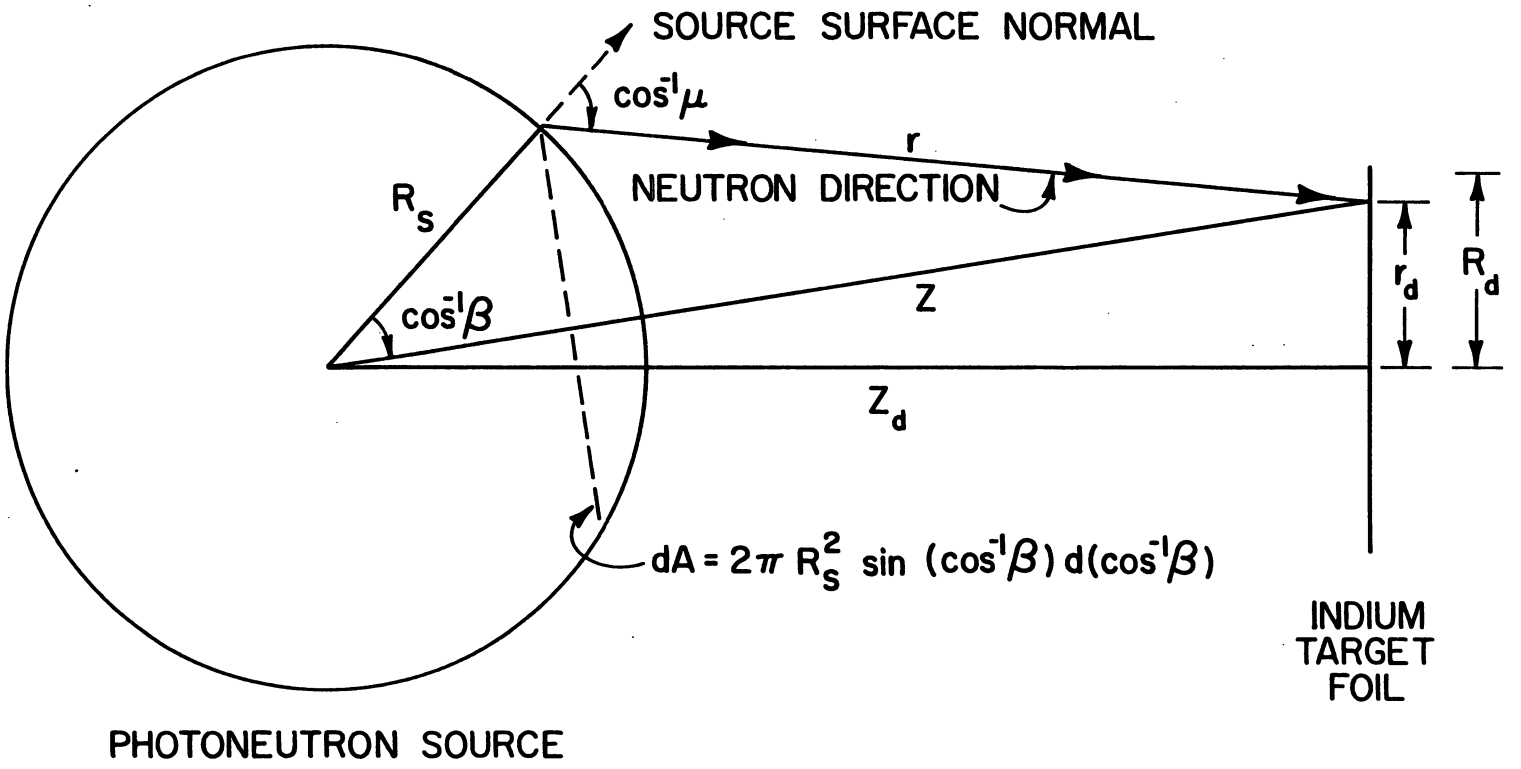

Figure 6.B.1. Geometry and Variables of the Scalar Flux Calculations

normalized number of neutrons emitted in $d\mu$ about μ integrated over all 2π azimuth angles and the source surface. Within a normalization constant, this is exactly what VES provides in the emission angular distribution. The discretized distribution, $F(\mu_i)$ for i = 1,2,...20, obtained from running VES was smoothed by fitting the data to a fifth order polynomial in μ, to obtain,

$$F(\mu) = \sum_{i=1}^{5} f_i \mu^i .$$

Normalization of $F(\mu)$ to a unit source strength requires that

$$\int_0^1 \phi(\mu)\,d\mu = \frac{1}{A_n} \int_0^1 F(\mu)\,d\mu = 1 \ \frac{\text{neutron}}{\text{second}} \qquad 6.B.2$$

giving rise to the normalization constant, A_n, with

$$A_n = \sum_{i=1}^{5} \frac{f_i}{(i+1)} \qquad 6.B.3$$

The smooth curve in figure 6.A.1 is the normalized $F(\mu)$.

The scalar flux, $\phi(Z)$, is calculated as the appropriately weighted integral of $\phi(\mu,\psi,S)$ over the three dependent variables. This can be equivalently written as

$$\phi(Z) = \int_S \frac{\phi(\mu,\psi,S)\,dS}{r^2} \qquad 6.B.4$$

where S is the surface area of the source that contributes to the flux at Z. The integration is performed as the sum of the flux contributions from equidistant (constant r) annulus rings of the neutron source surface. These rings are perpendicular to and centered about the line connecting the source center and the point at which the flux is being calculated. Referring to the problem geometry in figure 6.B.1, the following relationships and definitions are observed:

$$dS = 2\pi R_s^2 \sin(\cos^{-1}\beta)\, d(\cos^{-1}\beta) \qquad 6.B.5$$

$$= -2\pi R_s d\beta$$

$$Z = \sqrt{Z_d^2 + r_d^2} \qquad 6.B.6$$

$$r^2 = R_s^2 + Z^2 - 2R_s Z\beta \qquad 6.B.7$$

$$\mu = \frac{Z_\beta - R_s}{r} \qquad 6.B.8$$

The limits of integration are from normal to tangential neutron emission. In terms of the eventual variable of integration, β, the limits as calculated from equation 6.B.8 are from $\beta = 1$ to $\beta = R_s/Z$. Substituting the results of equation 6.B.2, 6.B.3 and 6.B.5 through 6.B.8, equation 6.B.3 becomes

$$\phi(Z) = \frac{1}{4\pi A_n} \sum_{n=1}^{5} f_n \int_{R_s/Z}^{1} \frac{(Z\beta - R_s)^n}{(R_s^2+Z^2-2R_sZ\beta)^{((n+2)/2)}} \, d\beta \qquad 6.B.9$$

A variable substitution suggested by Baldwin (BAL 80) reduced the above integrals to forms which were analytic. The resulting expression for the flux at a point a distance Z away from the source center is

$$\begin{aligned}\phi(Z) = \frac{1}{4\pi A_n} \Bigg\{ & \frac{1}{ZR_s^2} \left[Z - (Z^2 - R_s^2)^{1/2}\right] f_1 \\ & + \left[\frac{1}{2R_s^2} + \frac{(Z^2-R_s^2)}{4R_s^3 Z} \ln\left(\frac{Z-R_s}{Z+R_s}\right)\right] f_2 \\ & + \frac{1}{ZR_s^4} \left[ZR_s^2 - \frac{2Z^3}{3} + \frac{2}{3}(Z^2-R_s^2)^{3/2}\right] f_3 \\ & + \frac{1}{8R_s^2} \left[5 - \frac{3Z^2}{R_s^2} - \frac{3(Z^2-R_s^2)^2}{2ZR_s^3} \ln\left(\frac{Z-R_s}{Z+R_s}\right)\right] f_4 \\ & + \left[\frac{8Z^4}{15R_s^6} - \frac{4Z^2}{3R_s^4} + \frac{1}{R_s^2} - \frac{8}{15} \frac{(Z^2-R_s^2)^{5/2}}{ZR_s^6}\right] f_5 \Bigg\}\end{aligned} \qquad 6.B.10$$

The next step is the calculation of the area averaged scalar flux. Defining "T" and "dT" as the target area and differential target area respectively, with R_d the target disk radius, the area average flux "$\bar{\phi}_A$" is

$$\bar{\phi}_A = \frac{\int_T \phi(Z)\,dT}{\int_T dT} = \frac{\int_T \phi(Z)\,dT}{\pi R_d^2} \qquad 6.B.11$$

With "$dT = 2\pi r_d dr_d$" equation 6.B.11 becomes

$$\bar{\phi}_A = \frac{2}{R_d^2} \int_{Z_d}^{\sqrt{Z_d^2+R_d^2}} \phi(Z)\,Z\,dZ$$

Though tedious, this integration can be performed to obtain the desired closed form, analytic solution. No numerical integration is required in the evaluation of the area averaged flux. The result of the integration is included in figure 6.B.2. The limits of integration for $\bar{\phi}_A$ have not been included in equation 6.B.12. The evaluation of the expression at the two limits is left up to the computer program PHIBAR. A description of the input requirements and a listing of the program are included in Appendix A. The basic input parameters to the code are the five polynomial fit coefficients, f_i, and the source center-target center (more commonly referred to as the source-target) spacing.

One final point to be made about the PHIBAR calculations is that the code actually calculates the volume averaged scalar flux for the indium target foil. For the narrowest spacing, the flux at the surface of the foil closest to the source is 0.8% higher than that at the

$$\bar{\phi}_A = \frac{1}{2\pi A_n R_d^2} \left\{ \left[f_1 + \frac{f_2}{2} + f_3 + \frac{5f_4}{8} + f_5 \right] \frac{z^2}{2R_s^2} \right.$$

$$- \left(\frac{f_3}{6} + \frac{3f_4}{32} + \frac{f_5}{3} \right) \frac{z^4}{R_s^4} + \left(\frac{4f_5}{45} \right) \frac{z^6}{R_s^6}$$

$$+ \left(\frac{f_1}{2} + \frac{f_3}{4} + \frac{f_5}{6} \right) \left[\ln(z+(z^2-R_s^2)^{1/2}) - \frac{z}{R_s^2} (z^2-R_s^2)^{1/2} \right]$$

$$+ \left(\frac{f_3}{6} + \frac{f_5}{9} \right) \frac{z}{R_s^4} (z^2-R_s^2)^{3/2} - \left(\frac{4f_5}{45} \right) \frac{z}{R_s^6} (z^2-R_s^2)^{5/2}$$

$$+ \left[A(z^5-R_s^5) + B(z^3-R_s^3) + C(z-R_s) \right] \ln(z-R_s)$$

$$- \left[A(z^5+R_s^5) + B(z^3+R_s^3) + C(z+R_s) \right] \ln(z+R_s)$$

$$\left. - \left[\left(\frac{z^2}{2} + R_s^2 \right) A + B \right] z^2 R_s \right\} \Bigg|_{z_d}^{z_d^2+R_d^2}$$

where $A = -3f_4/80R_s^5$ 6.B.12

$B = (2f_2 + 3f_4)/24R_s^3$

$C = -(4f_2 + 3f_4)/16R_s$

$$A_n = \sum_{i=1}^{5} \frac{f_i}{(i+1)}$$

Figure 6.B.2. Equation 6.B.12, The Area Averaged Scalar Flux Expression

back surface. In light of this, PHIBAR was written to calculate the area averaged flux at a user specified number of slices through the foil. A Simpson's rule numerical integration was then performed to determine the volume averaged flux, $\bar{\phi}_v$. Experience showed that only three slices were required for convergence to better than 0.01%.

6.C. Flux Calculation Sensitivities

6.C.1. Simplified Flux Calculation Technique

Analyses of the flux calculation sensitivities were divided into VES related and experiment related quantities. For the VES related factors, the PHIBAR approach to the flux calculation (see section 6.B) required VES runs, polynomial fittings and the running of PHIBAR. This long process was circumvented with the development of a simplified flux calculation approach. A more detailed description of the analysis is found in Appendix B, but the approach and result are included here.

Using a method suggested by Baldwin (BAL 81), this simplified flux calculation technique required only the histogram data from the neutron emission angular distribution calculations of VES. A closed form, analytic solution for the flux at a point Z was obtained by summing the flux contribution from each μ_i bin for the twenty bin resolution provided by VES. The expression obtained was

$$\phi_H(Z) = \frac{-1}{4\pi A_n R_s Z} \sum_{i=1}^{20} F(\mu_i) \ln \frac{\sqrt{Z^2 - R_s^2(1-\mu_i^2)} - R_s\mu_i}{\sqrt{Z^2 - R_s^2(1-\mu_{i-1}^2)} - R_s\mu_{i-1}}$$

6.C.1

Although this equation cannot be area averaged to obtain a closed form, analytic solution for $\bar{\phi}_{A,H}$ (the criterion for the actual flux determinations), the expression provides a quick means of calculating the flux at a point. The result is exact within the inherent uncertainties of the $F(\mu_i)$ data on which it is based. Equation 6.C.1 was incorporated in the program FLUX, a listing of which is contained in Appendix A.

The sensitivity studies which follow in section 6.C.2 utilized the FLUX approach after a preliminary comparison with a point flux calculation of PHIBAR showed interchangeability of the two techniques. Extrapolation of sensitivities determined by FLUX, to the area and volume averaged calculations of PHIBAR were assumed to be one-to-one. All sensitivity studies were performed with the Na-Be photoneutron source as the reference. In general, Na-Be source-target spacings #1, 3, 5 and 7 were used to study the sensitivity with spacing.

6.C.2. VES Related Sensitivities

6.C.2a. PHIBAR versus FLUX

Two points were considered here. The first was how the flux calculations using PHIBAR vary with the

polynomial fit order of $F(\mu)$. A reference VES run for the Na-Be source was obtained and second through fifth order polynomial fits to the emission angular distribution were performed. Point flux calculations as performed by PHIBAR were obtained for the four reference spacings. The percent deviations from the fifth order fit results were determined and are summarized in Table 6.C.1.

Table 6.C.1

PHIBAR Versus FLUX Comparison

	% Deviation for Spacing #			
Calculation	1(2.1 cm)	3(4.7 cm)	5(7.2 cm)	7(9.7 cm)
PHIBAR-2*	1.43	0.18	0.08	0.04
PHIBAR-3	0.39	0.06	0.02	0.01
PHIBAR-4	-0.14	-0.02	-0.01	0.00
FLUX	-0.06	-0.02	-0.02	0.00

*Refers to polynomial fit order

The second point of interest concerned the interchangeability of PHIBAR and FLUX for these sensitivity studies. Equivalence of the two techniques had to be demonstrated in order for the FLUX approach to be used in the rest of the studies. The $F(\mu_i)$ data was obtained from the reference VES run and FLUX was run with this

data. Table 6.C.1 also contains the percent deviation from the fifth order PHIBAR results.

These results verify that the fifth order PHIBAR and the FLUX approaches are essentailly equivalent. Sensitivities arrived at with FLUX will be used for the final flux uncertainties as if they had been determined from a PHIBAR analysis.

These data also show that the flux calculation becomes nearly insensitive to the emission angular distribution fit as the source-target spacing increases. This can be predicted because the photoneutron source looks more like an isotropic point source as the source-target spacing increases. Not so predictable is that at just three millimeters off the source, a crude, second order fit gives rise to a flux only 1.43% below the actual quantity. A point source approximation here would be 18.8% below the actual value.

6.C.2b. Statistical variation

VES is a Monte Carlo based program and as such is subject to statistical variation. In general, the more gamma and neutron histories followed, the smaller the statistical uncertainty in the quantities calculated. In order to quantify this effect, Baldwin (BAL 81) modified VES to print out pertinent quantities at fixed gamma history intervals. In the reference VES run three of

these intermediate output reports in addition to the final output were obtained. The fluxes as calculated from the intermediate results were obtained after 5740, 11480, and 17220 gamma histories. Using the reference case results for 22960 gammas, the percent deviations were calculated for the three intermediate flux results and are summarized in Table 6.C.2.

Table 6.C.2

Statistical Variation Uncertainties

Gamma Histories	% Deviation for Spacing # 1	3	5	7
5740	-0.09	-0.01	-0.01	0.00
11480	0.02	0.00	0.00	0.00
17220	-0.08	-0.01	-0.01	0.00

The statistical sensitivities as depicted in the percent deviation results above, continue to show a minimum of flux dependence on small changes in the emission angular distribution. The trend of decreasing sensitivity with increasing source-target spacing is also observed, as expected.

The final VES runs for the four photoneutron sources each analyzed 34440 gamma histories. In light of this

larger sampling and with the trend of the statistical variation results just discussed, a conservative 0.1% uncertainty in the flux calculation will be attributed to statistics for all spacings and all sources.

6.C.2c. Scattering cross sections

Uncertainties in the cross section data base, VESLIB, that affect all cross sections equally will have a minimal impact on VES results. The code performs most calculations based upon cross section ratios. Consequently, across the board cross section changes will give little information about the cross section sensitivity of VES.

Changes in absorption and (γ,n) cross sections simply alter the photoneutron source efficiency and have little effect on the emission angular distribution results. A meaningful study of the flux dependence on VES input cross sections reduces to flux dependence on the scattering reaction probabilities. Scattering is by far the major interaction mechanism for both neutrons and gamma rays.

With respect to changes in the gamma scattering cross section, calculations from the VES reference run showed that only 5% of the Na^{24} gammas survived a compton scattering event (remained above the beryllium (γ,n) threshold of 1.665 MeV). Of these, less than one percent gave rise to neutrons. Clearly this will have a minimal impact on the emission angular distribution. Consequently, only changes in the neutron scattering (and total) cross section

will be considered. Here again, across the board changes would not be as meaningful as select changes. The average neutron energy after a typical scattering event was determined to be 0.84 MeV. Since most neutrons produced are above this energy, the maximum effect of a scattering cross section change would be observed by modifying the VESLIB scattering data base in this energy region. The VESLIB neutron scattering cross sections for all of the source components from 0.84 MeV and above were increased by 10%. VES was run with reference case input parameters and the modified VESLIB data base. The FLUX program was run for the four usual spacings and the percent deviations from the reference fluxes were determined. Percent deviations for the other three spacings were interpolated from these results. The uncertainties in the flux determinations due to the cross section sensitivities of VES are assumed to be source-independent and are summarized in Table 6.C.3.

An interesting addition to the above discussion on neutron scattering sensitivities can be obtained from the VES output. The emission angular distribution for neutrons which do not scatter in the source is also maintained by VES. FLUX calculations using this data produces point fluxes which are 1.89, 0.27, 0.11 and 0.06 percent higher than the references case for the four usual spacings. Recalling from section 6.A that 27% of the Na-Be neutrons suffer a scatter, it appears that the effect of neutron

Table 6.C.3

Cross Section Dependent Uncertainties

Spacing #	Uncertainty %
1	0.05
2	0.03
3	0.01
4	0.01
5	0.00
6	0.00
7	0.00

scattering within the source is the reduction of the source surface area that contributes to the flux at a point. In other words, neutron scattering shifts the neutron emission distribution toward more normal escape.

6.C.2d. Number densities

Although each component of the photoneutron sources was weighed in the construction stage, some mass uncertainties should be expected. An error had been made in computing the number densities for a VES run with the Na-Be source. The results of VES for these errors were used in this number density sensitivity study. All three component number densities of the Na-Be source were over-estimated by 35%. FLUX analysis and comparison with

reference case fluxes gave percent deviations of 0.57, 0.08, 0.03, and 0.02 for the four usual spacings. A more realistic but still conservative estimate of the number density uncertainty was taken to be 7%. Scaling the above results down and interpolating for the other three spacings, the flux uncertainties due to VES number density sensitivities were determined. The results are summarized in Table 6.C.4 and are assumed to be source independent.

Table 6.C.4

Number Density Uncertainties

Spacing #	Uncertainty %
1	0.11
2	0.07
3	0.02
4	0.02
5	0.01
6	0.01
7	0.00

6.C.2e. Source region size

The sensitivity of the VES calculations to source region sizes was investigated by reducing the gamma emitting core radius by about 3%. The beryllium was assumed to fill the gap and the overall source radius

remained fixed. This 10% decrease in the core volume resulted in percent deviations from the reference case of 1.28, 0.16, 0.06, and 0.04 for the four spacings. Since all components of the sources were very accurately machined, a more realistic uncertainty of one tenth of the above results will be used. Scaling and interpolating the above data gives rise to the source independent source region size uncertainties in Table 6.C.5.

Table 6.C.5

Source Region Size Uncertainties

Spacing #	Uncertainty %
1	0.13
2	0.08
3	0.02
4	0.02
5	0.01
6	0.01
7	0.00

6.C.3. Experiment Related Sensitivities

6.C.3a. Source-target spacing

The sensitivity of the volume averaged scalar flux calculations of PHIBAR to source-target spacing uncertainties were investigated. Using the same VES reference

case as in section 6.C.2, the $\bar{\phi}_v$ values of PHIBAR were determined for six source-target spacing uncertainties around the Na-Be spacings #1, 3, 5 and 7. The six uncertainties bracketed the range of the root mean square spacing deivations discussed in section 3.B.2. Typical RMS deviations fell between 0.002 cm and 0.008 cm and the six uncertainties investigated were 0.001, 0.003, 0.005, 0.007, 0.009, and 0.015 cm. Percent deviations from the reference case fluxes were calculated and the results are plotted in figure 6.C.1. This analysis was intended only as a demonstration of the flux sensitivity to source-target spacing uncertainties.

The uncertainty applied to an actual flux calculation result was based upon the specific RMS spacing value obtained for each spacing and each source. With the fifth order polynomial fits obtained from the final VES runs for each of the four photoneutron sources, PHIBAR was run for all of the experimental source-target spacings listed in Table 3.B.2 to obtain the $\bar{\phi}_v$ values. In addition, a $\bar{\phi}_v(Z_d\text{-RMS})$ value was obtained by calculating the volume averaged flux at each of the source-target spacings reduced by its associated RMS uncertainty. The percent deviation between these two sets of values are summarized in Table 6.C.6. These deviations have been taken as the uncertainty in the flux calculations due to source-target spacing uncertainties.

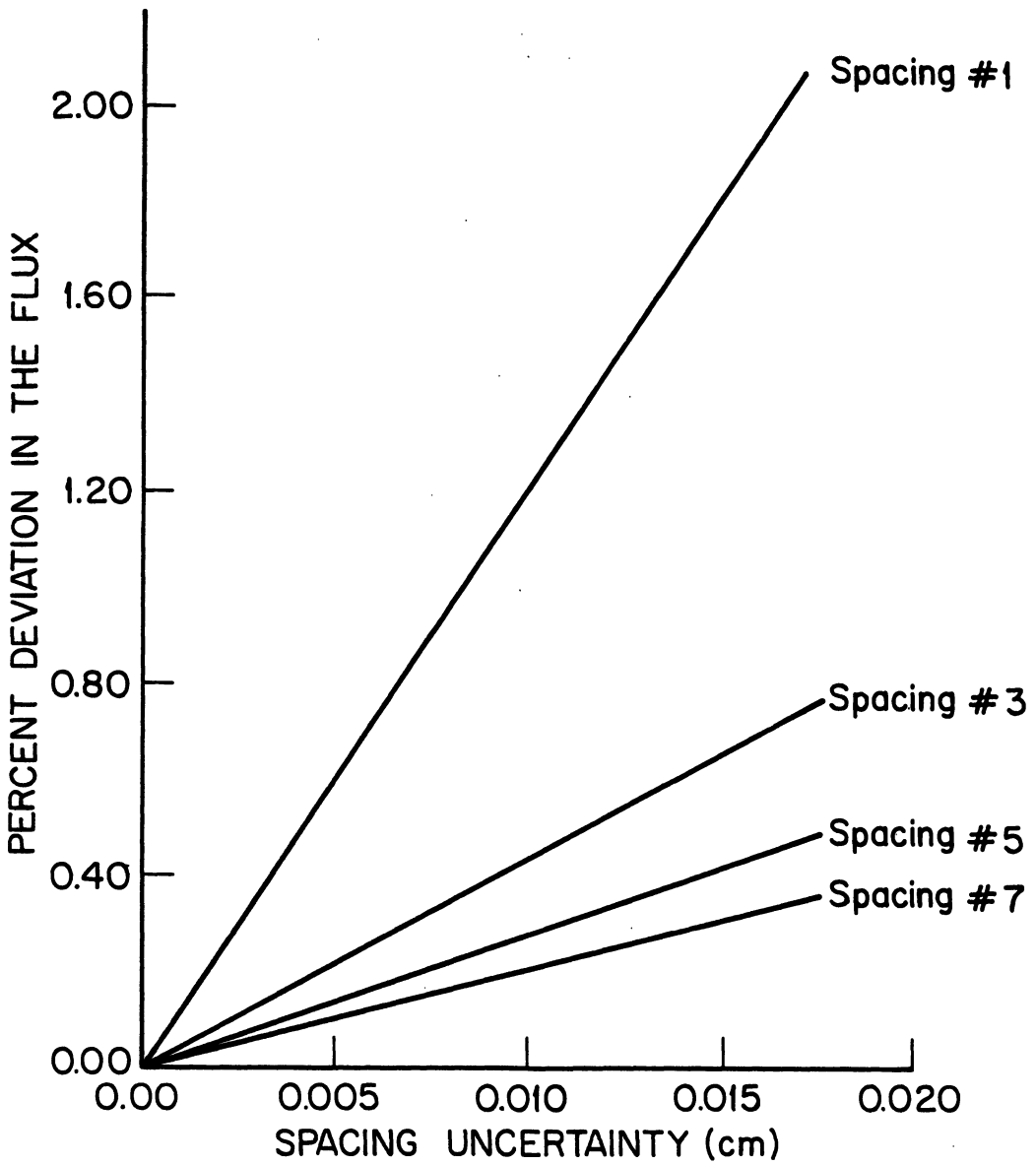

Figure 6.C.1. Flux Calculation Sensitivity to Source-Target Spacing Uncertainties

Table 6.C.6

Source-Target Spacing Uncertainties (%)

	Source			
Spacing #	Sb-Be	Na-D_2C	La-Be	Na-Be
1	0.09	0.41	0.18	0.17
2	0.25	0.26	0.27	0.12
3	0.13	0.11	0.13	0.05
4	0.14	0.25	-	0.07
5	0.06	0.10	-	0.10
6	0.05	0.04	-	0.04
7	0.06	0.06	-	0.05

6.C.3b. Target foil diameter

Although a precision punch and die were used to produce the indium foils, there is a possibility of some uncertainty in the foil diameter. A very conservative uncertainty of 1% was assumed and PHIBAR was run for all seven spacings of the Na-Be source. The fractional deviations from the reference case were calculated and taken as the flux uncertainties due to target foil diameter errors. The results in Table 6.C.7 are assumed to be source independent.

6.C.3c. Target foil thickness

All of the final flux calculations were run with a nominal foil thickness of 0.00674 cm, the average

Table 6.C.7

Target Foil Diameter, Thickness and Misalignment Uncertainties (%)

Spacing #	Diameter	Thickness	Misalignment
1	0.23	0.04	0.18
2	0.08	0.02	0.07
3	0.04	0.01	0.04
4	0.03	0.01	0.03
5	0.01	0.02	0.02
6	0.01	0.01	0.02
7	0.01	0.01	0.01

thickness of the eight foils. Foil thicknesses ranged 5% about this value. A determination of the flux calculation uncertainty due to foil thickness variations was performed. PHIBAR was run for the seven Na-Be spacings assuming a 10% increase in the nominal foil thickness. Percent deviation results were again taken as the flux uncertainties due to this factor. Summarized in Table 6.C.7, these sensitivities are assumed to be spacing-dependent only.

6.C.3d. Target foil misalignment

All of the flux calculations are based on two assumptions:

i. The plane of the target foil surface is parallel to the plane of the source well bottom plate on which the source rests.

ii. The perpendicular dropped from the source center intersects the target foil at its center.

The first factor can be reasonably well achieved by the accurate machining of the upper stainless steel spacers. An attempt to minimize deviation from the geometry of factor two was provided by the source positioning device and the special jig utilized in machining the source-foil alignment equipment. Uncertainties here were considered significant.

In order to investigate the flux sensitivity to foil misalignment, the computer program HISTO.FLUX was written. Based upon the histogram flux calculation approach of FLUX, this program goes two steps further. It is capable of calculating the area averaged flux for a foil horizontally displaced a distance "δ" from the ideal geometry of factor two. A listing of HISTO.FLUX along with the input requirements and variable descriptions can be found in Appendix A.

Figure 6.C.2 depicts the geometry and variables of interest in this analysis. The area averaged flux of interest is

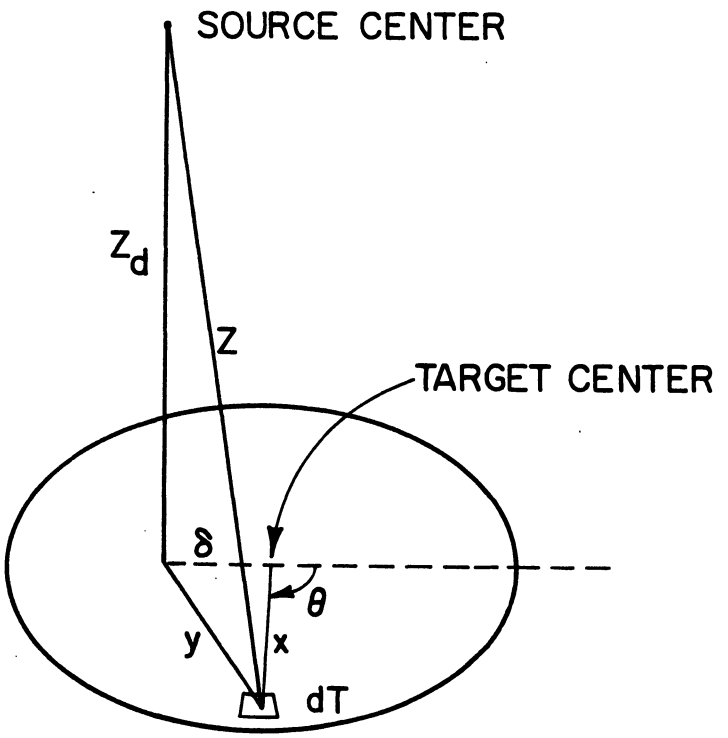

Figure 6.C.2. Geometry and Variables of the Foil Misalignment Flux Calculations

$$\bar{\phi}_{A,H} = \frac{\int_T \phi_H(Z)\,dT}{\int_T dT} \qquad 6.C.2$$

where T = target area = πR_d^2

dT = differential target area = xdxdθ

$\phi_H(Z)$ = histogram method flux calculation at a point

= Equation 6.C.1.

In this misalignment study, $Z = f(x,\theta,\delta)$. From the geometry of the problem, this functional dependence can be

written

$$Z = \sqrt{z_d^2 + \delta^2 + x^2 + 2\delta x\cos\theta} \quad . \qquad 6.C.3$$

Substituting equation 6.C.3 for Z into 6.C.1 for $\phi_H(Z)$ and then into equation 6.C.2, produces a double integral over x and θ which cannot be analytically reduced. The program HISTO.FLUX performed this double integration numerically using the trapezoidal rule discussed by Bjork (BJO 74).

The general misalignment sensitivity of the flux calculation was performed by running HISTO.FLUX for the four usual spacings with "δ" values of 0.005, 0.015, 0.030, 0.060 and 0.120 cm. Plots of the results of the percent deviation calculations are found in figure 6.C.3.

Within 5%, these same results could have been obtained using the source-target spacing sensitivity analysis results of section 6.C.3a. The difference between the source center-target center spacings for the aligned and misaligned foils gives rise to a percent deviation in the flux which is nearly identical to the results achieved here. This was expected and suggests that factor one sensitivities tend to be self-cancelling.

The uncertainties in the flux calculation attributed to foil misalignment are in Table 6.C.7. Theyare assumed to be source independent and were interpolated for a "δ = 0.075 cm". This is the maximum misalignment attainable

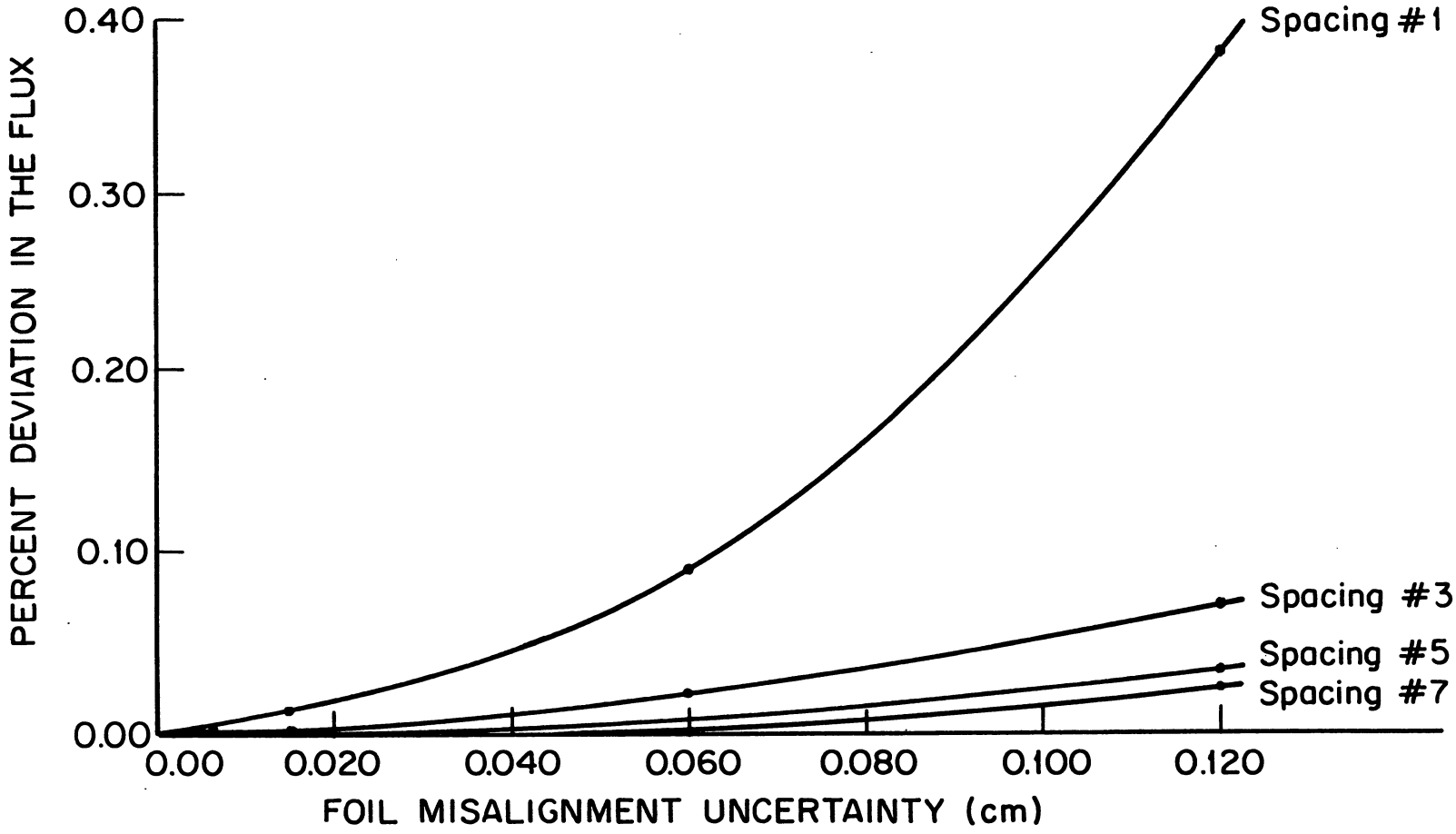

Figure 6.C.3. Flux Calculation Sensitivity to Foil Misalignment Uncertainties

in light of the foil and target foil holder recess radii. This does assume that the target foil rests completely within the recess and that the ideal activation geometry exists for the source and foil holder. Even so, this is still considered a conservative estimate of the uncertainty contribution.

6.D. Flux Results and Uncertainties

VES was run with 34440 gamma histories for each photoneutron source. Fifth order polynomial fits to the emission angular distributions were performed. The volume averaged scalar flux calculations were calculated by PHIBAR. Source-target spacing data and RMS spacing deviations were obtained from Table 3.B.2.

The uncertainties associated with these flux results were taken as the quadrature sum of the VES and experiment related factors of section 6.C. The results of the flux calculations and the associated uncertainty determinations have been summarized in Table 6.D.1. Note that these flux quantities are volume averaged over the target foil, normalized to a unit source strength and uncorrected for the neutron scattering factors in the experiment.

One final point of interest concerns the need for this complicated technique for calculating the flux. How accurately would a simple point source approximation be in determining the neutron flux? Figure 3.D.1 is a plot of

Table 6.D.1

Volume Averaged Scalar Neutron Flux Results*

Spacing #	Source: Sb-Be	Na-D_2C	La-Be	Na-Be
1	0.01512 ±0.37%	0.02127 ±0.58%	0.02080 ±0.42%	0.02077 ±0.43%
2	0.006133±0.31%	0.007444±0.32%	0.007331±0.33%	0.007350±0.22%
3	0.003307±0.20%	0.003770±0.16%	0.003740±0.18%	0.003762±0.13%
4	0.002074±0.19%	0.002299±0.28%	-	0.002282±0.13%
5	0.001434±0.13%	0.001556±0.14%	-	0.001550±0.15%
6	0.001048±0.12%	0.001126±0.11%	-	0.001124±0.11%
7	0.000795±0.12%	0.000845±0.12%	-	0.000843±0.12%

*Flux in units of neutrons/cm^2·s for a source strength of 1 neutron/second. Uncertainties quoted in percent.

the percent increase in the flux from the PHIBAR technique with respect to a point source determination as a function of source-target spacing. This particular graph is for the Na-Be photoneutron source. Clearly, the additional effort of the PHIBAR approach was warranted.

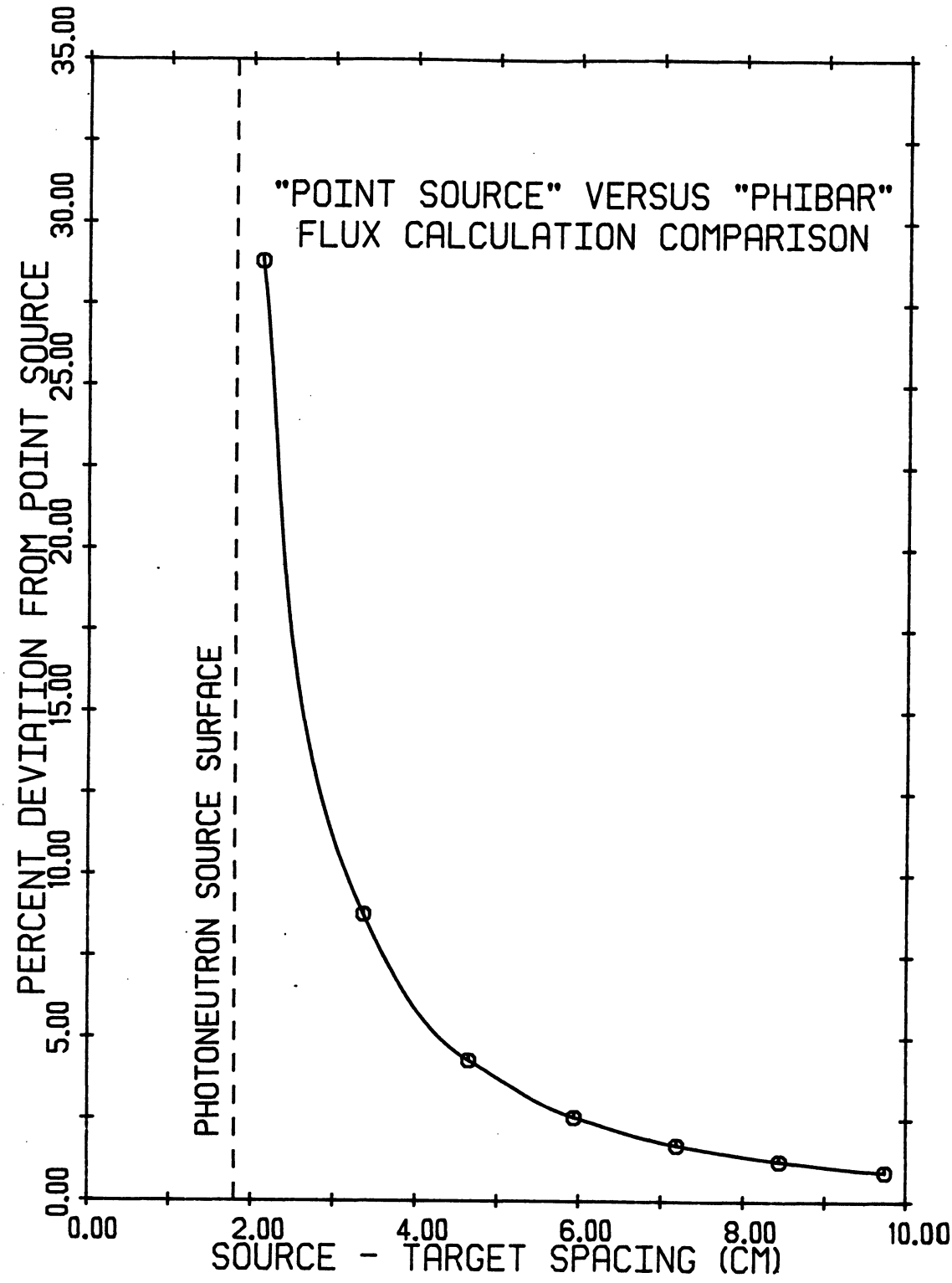

Figure 6.D.1. Deviation of PHIBAR Flux from a Point Source Flux

CHAPTER 7

MAJOR CORRECTION FACTORS

Four major corrections were required before the final cross sections could be calculated. The neutron flux at the indium targets was increased over the results of Chapter 6 due to neutron scattering from the experiment support structures and the foil holder plate. Scattering from the support structures was treated with a point scattering approximation. Foil holder scattering was simulated by using a Monte Carlo program to calculate the average path length factor through the target foil for neutrons backscattered in the holder plate. The room-return induced In^{116m} activity was determined from an analysis of saturated In^{116m} activity (per target atom) as a function of spacing-dependent neutron flux. Neutron energy spectrum correction factors for the photoneutron sources were deduced from the calculated energy distributions and cross section shape data from ENDF/B-IV.

7.A. Neutron Scattering From Support Structures

A point source-point scatterer-point target approximation was used to determine the neutron inscatter contri-

butions at the target. Scattering from the experiment chamber, the source well, the source positioning-device and the foil holder assembly (except for the foil holder plate) were considered. The generalized geometry and variables of interest for the scattering problem are found on figure 7.A.1. Assuming an isotropic source and isotropic scattering, the expression for the fractional increase in the flux at the target due to inscatter was

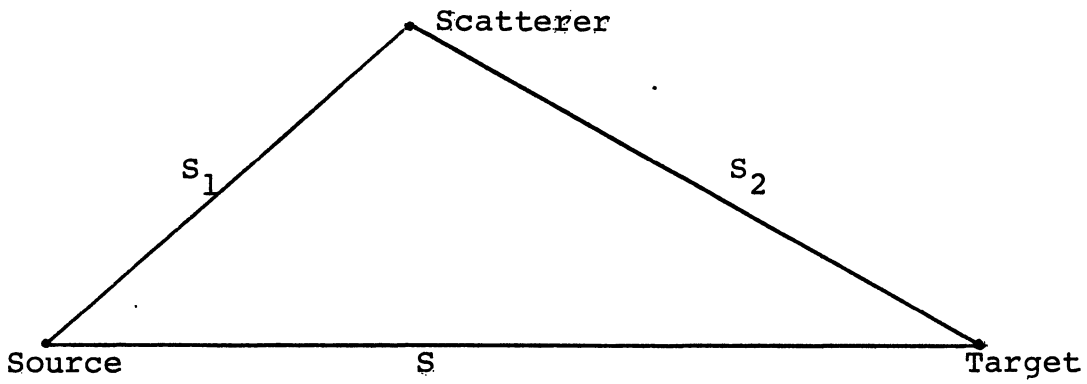

Figure 7.A.1. Generalized Scattering Geometry for the Point Approximation

derived as:

$$\frac{d\phi_o}{\phi_o} = \frac{\Sigma_s}{4\pi} \left(\frac{S}{S_1 S_2}\right)^2 \cdot dA \qquad 7.A.1$$

with $\Sigma_s = \sigma_s N \gamma$

where: $\frac{d\phi_o}{\phi_o}$ = differential fractional increase in the flux

σ_s = microscopic scattering cross section

N = number density of scattering nuclei

γ = thickness of the scatterer

The scattering correction, $\frac{\delta\phi_o}{\phi_o}$, was obtained by integrating equation 7.A.1 over the surface area of the scatterer.

Scattering from each of the components of the support structures could be described by one of four possible geometries. The four geometries and the appropriate variables are drawn in figures 7.A.2 through 7.A.5. The results of the integration of equation 7.A.1 over the four scattering geometries are presented here.

Geometry #1 - Cylindrical scatterer with axis perpendicular to the source-target axis

$$\frac{\delta\phi_o}{\phi_o}(\#1) = \frac{\Sigma_s S^2 R}{2} \int \frac{dz}{(R^2+z^2)\left((z^2+S^2+R^2)^2 - 4S^2R^2\right)^{1/2}}$$

Geometry #2 - Disk scatterer with source-disk axis perpendicular to the source-target axis

$$\frac{\delta\phi_o}{\phi_o}(\#2) = \frac{\Sigma_s S^2}{2} \int \frac{rdr}{(r^2+y^2)\left((y^2+S^2+r^2)^2 - 4r^2S^2\right)^{1/2}}$$

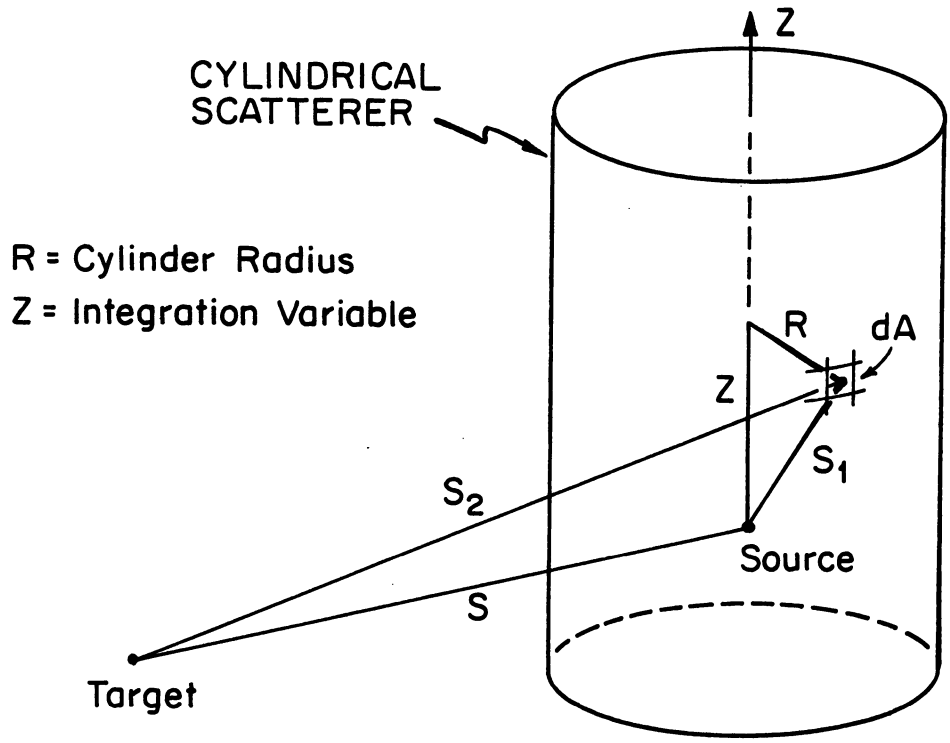

Figure 7.A.2. Scattering Geometry #1

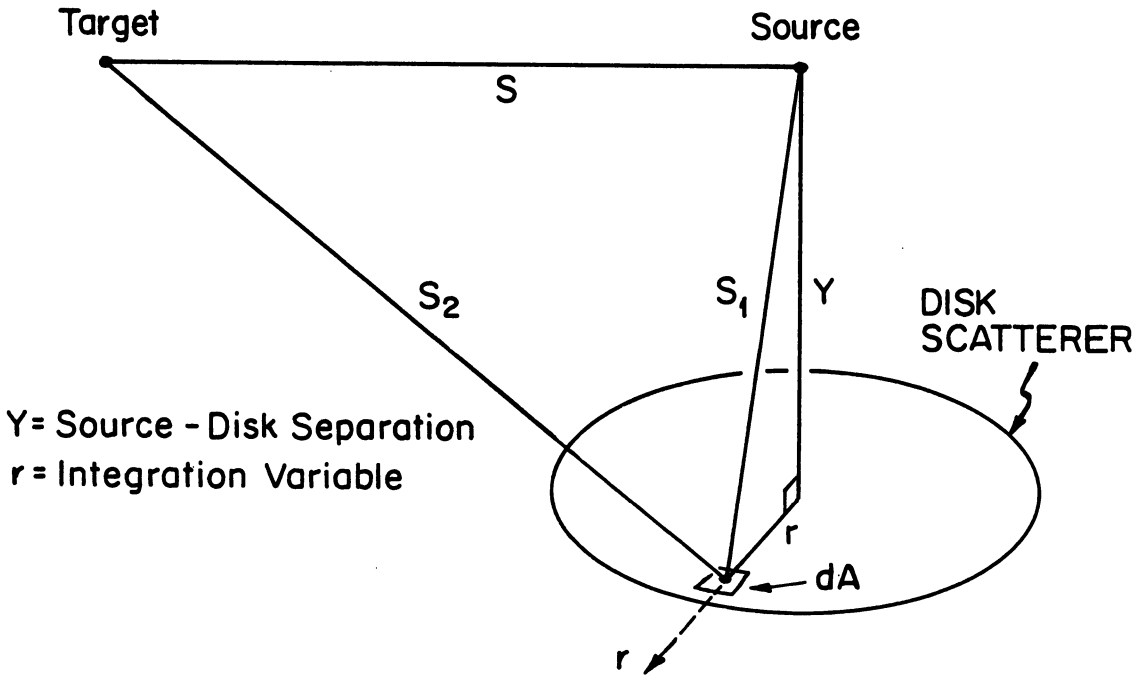

Figure 7.A.3. Scattering Geometry #2

Geometry #3 - Cylindrical scatterer with axis colinear with the source-target axis

$$\frac{\delta\phi_o}{\phi_o}\ (\#3) = \frac{(\Sigma_s S^2 R)}{2} \int \frac{dz}{(R^2+(S-z)^2)(R^2+z^2)}$$

Geometry #4 - Disk scatterer with source-disk axis colinear with the source-target axis

$$\frac{\delta\phi_o}{\phi_o}\ (\#4) = \frac{\Sigma_s S^2}{2} \int \frac{rdr}{(r^2+zz^2)(r^2+(S-zz)^2)}$$

The computer program PT-SCAT.A was written to evaluate these integrals numerically. A listing of the program and a description of the input variables is included in Appendix A. The program was run for each component of the experimental package (except for the foil holder plate) and the spacing-dependent results are reported in Table 7.A.1. Uncertainties in these corrections have been taken as 15% and 25% of the correction applied for the Sb-Be source and the other three sources, respectively. These errors reflect cross section data uncertainty and the effects of the error made in assuming a point source. The additional uncertainty applied to the Na-D_2C, La-Be and Na-Be sources accounts for the potential inaccuracy in assuming isotropic scattering.

The contribution of air scatter has been included in the results of Table 7.A.1. Net increases in the flux

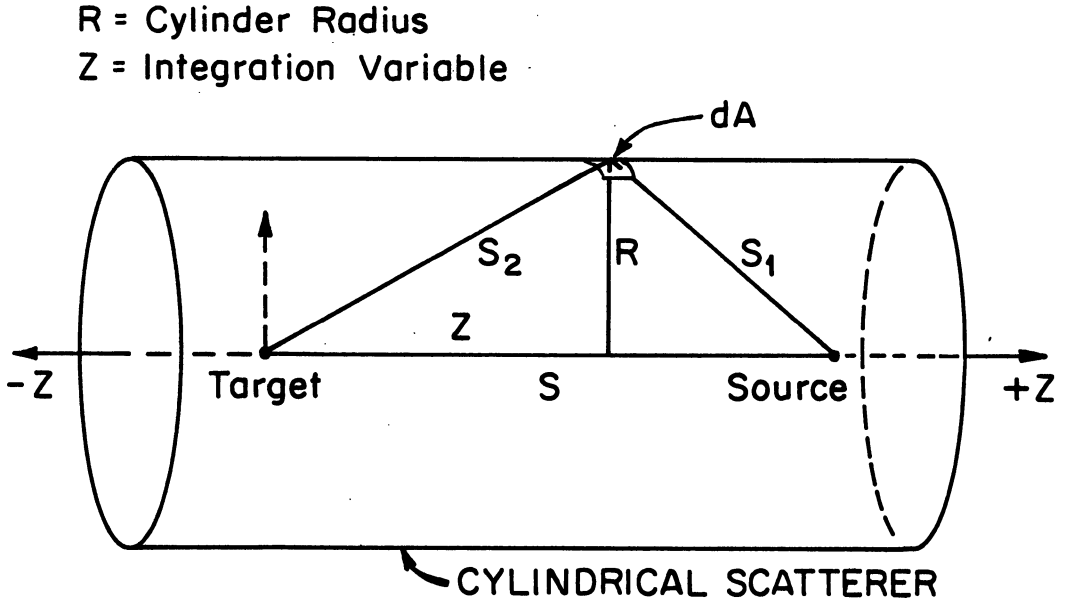

Figure 7.A.4. Scattering Geometry #3

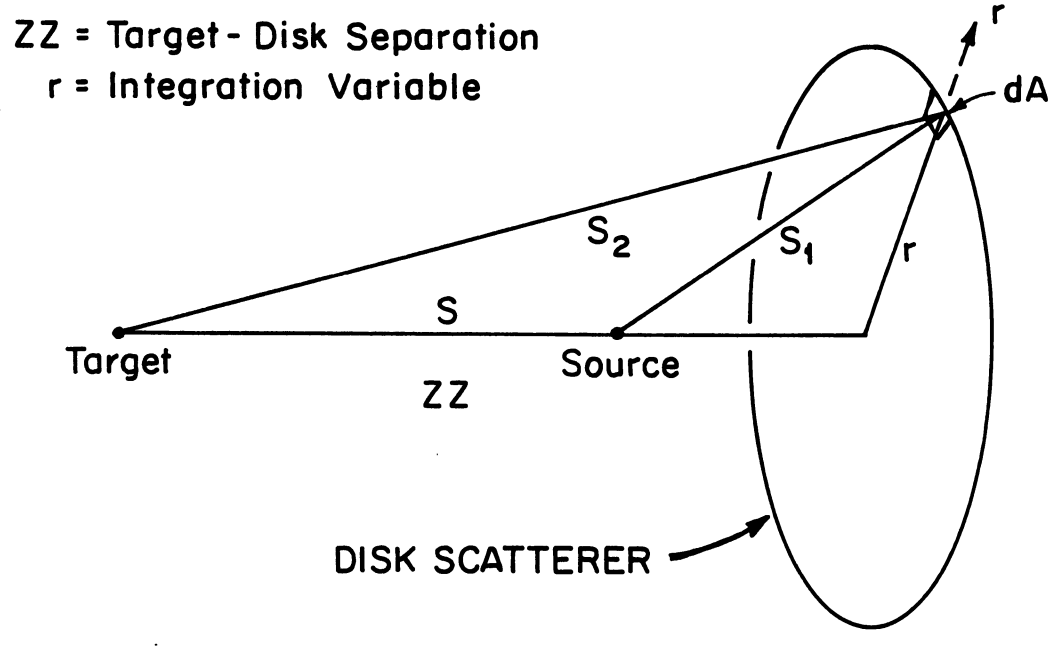

Figure 7.A.5. Scattering Geometry #4

Table 7.A.1

Support Structure and Foil Holder Scattering Corrections

Neutron* Source	Spacing Number 1	2	3	4	5	6	7
Sb-Be							
a	0.042	0.063	0.072	0.076	0.079	0.083	0.088
b	0.058	0.060	0.060	0.061	0.061	0.061	0.061
Na-D_2C							
a	0.024	0.038	0.045	0.048	0.050	0.053	0.056
b	0.028	0.030	0.030	0.030	0.030	0.030	0.030
La-Be							
a	0.017	0.028	0.033	0.036	0.039	0.041	0.045
b	0.021	0.022	0.022	0.022	0.023	0.023	0.023
Na-Be							
a	0.015	0.024	0.029	0.031	0.032	0.034	0.036
b	0.012	0.012	0.013	0.013	0.013	0.013	0.013

*a - Support structure results for $\delta\phi_o/\phi_o$ (uncertainty = 15% (Sb-Be), 25% (others) of correction)

b - Foil holder results for $\delta\phi_o/\phi_o$ (uncertainty - 20% of correction)

due to this effect ranged from 0.03% to 0.15% for spacing #1 (2.1 cm) to spacing #7 (9.8 cm). These values were calculated from the analysis by Mosburg (MOS 60).

7.B. Neutron Scattering from Foil Holder Plate

Scattering in the foil holder plate cannot be accurately accounted for using the point approximation of the last section because the target foil actually rests on the holder plate. Neutrons backscattered from the plate can have very large path lengths through the indium. Consequently, the approach to the calculation of this scattering correction was to determine the average path length through the foil for neutrons backscattered by the foil holder. The actual quantity measured is the path length factor which is the average of $1/\cos(\theta)$ for all of the neutrons scattered in the holder. With this

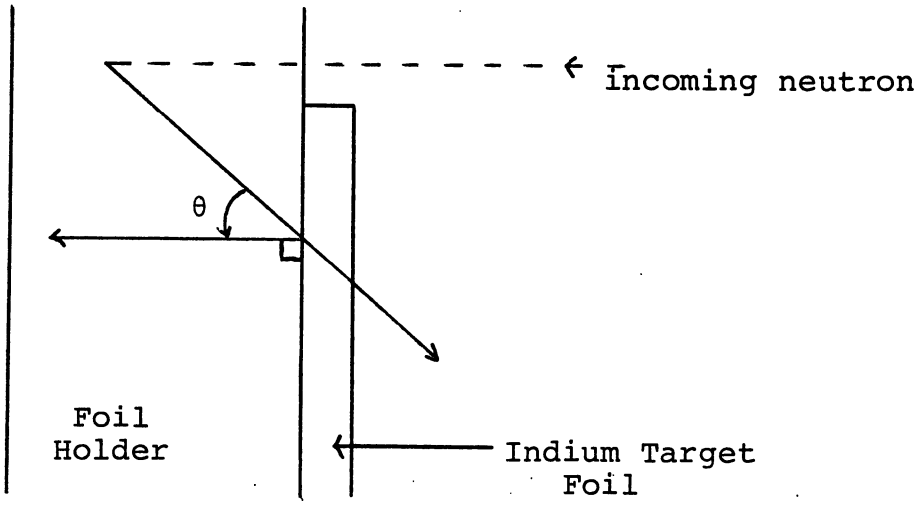

path length factor, the fractional increase in the flux at the target was calculated from

$$\frac{\delta\phi_o}{\phi_o} = \Sigma_s^H \gamma^H \left[\frac{A^H}{A^F} * \bar{\ell} * f \right] \qquad 7.B.1$$

where: Σ_s^H = macroscopic scattering cross section of the stainless steel foil holder

γ^H = thickness of foil holder plate

A^H = surface area of foil holder

A^F = surface area of the foil

$\bar{\ell}$ = average path length factor through the foil

f = fraction of neutrons backscattered

The determination of the average path length factor was performed using the Monte Carlo program AVEPATH.FB. A listing and description of input variables is included in Appendix A. In the program, neutrons normally incident on the foil holder were forced to backscatter at randomly chosen points in the holder through a series of user defined scattering angles. The average path length factor through the foil as a function of the backscattering angle was determined. Figure 7.B.1 is the path length factor distribution as a function of scattering angle for the Na-Be photoneutron source. This distribution was then weighted with the normalized scattering angular distribution (BNL-400) to obtain $\bar{\ell}$ as a function of neutron energy.

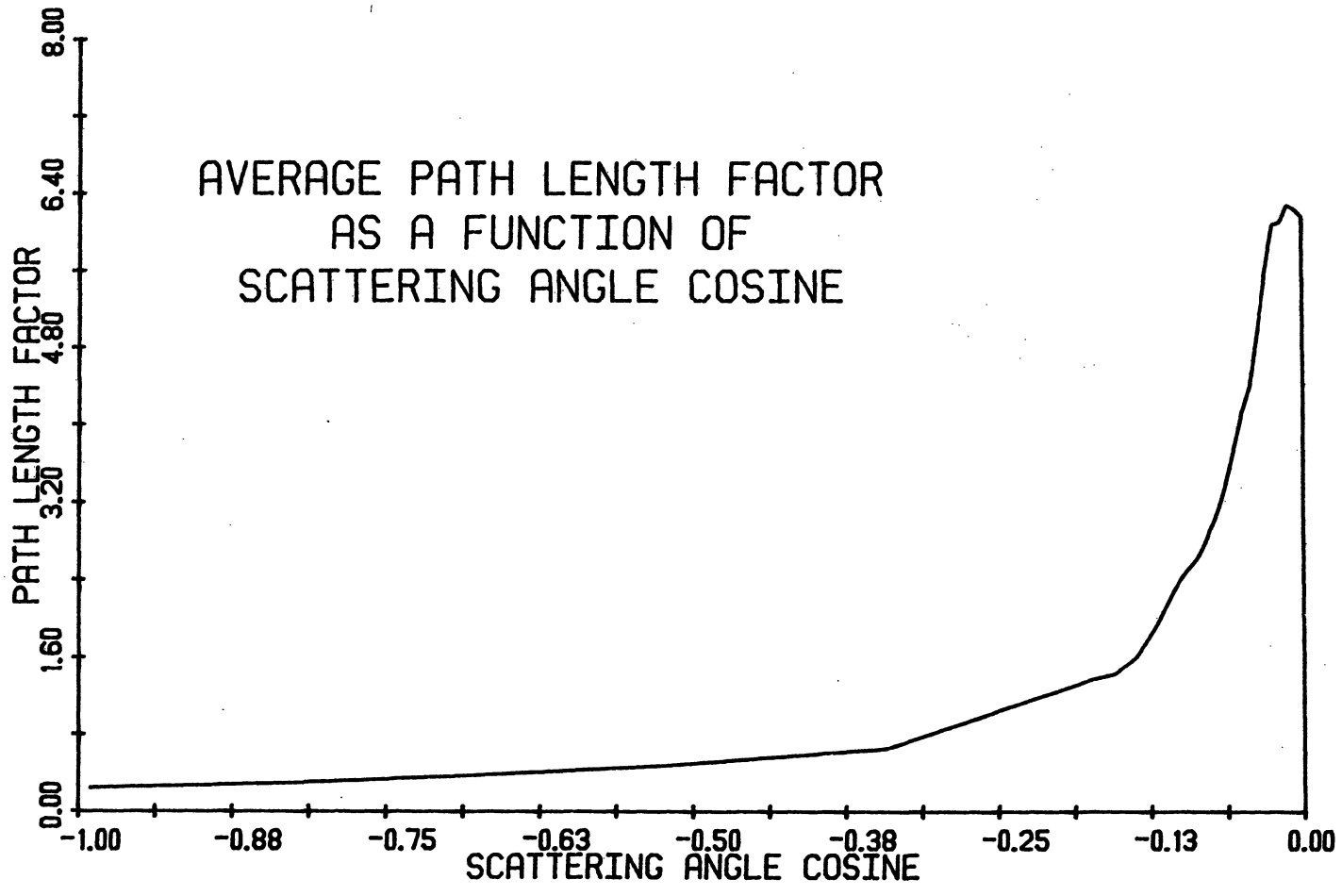

Figure 7.B.1. Average Path Length Distribution as a Function of Scattering Angle

With cross section data from BNL-325, the foil holder scattering correction was calculated for the four photoneutron sources. The results are included in Table 7.A.1. An uncertainty of 20% of the correction applied was taken from these results, reflecting potential cross section and angular distribution errors.

The inscatter increases in the flux at the target due to the factors of this and the proceding section were added to the original flux calculation results in Table 6.D.1. The final normalized neutron fluxes and associated uncertainties are summarized in Table 7.B.1. The uncertainties (in %) are the quadrature sum of the two scattering effect errors and the initial flux uncertainties in Table 6.D.1.

7.C. Room-Scattered Neutrons

The (n,γ) measurements were carried out at the center of the low-albedo laboratory. The room-return flux due to neutrons scattered in the walls was assumed to be spatially flat in the region of the indium foil activations. The total saturated In^{116m} activity per target atom can then be written as

$$\frac{A_\infty}{N'} = \bar{\sigma}\phi(r) + \overline{\sigma\phi}_{RR} \qquad 7.C.1$$

Table 7.B.1

Normalized Neutron Flux Results with Uncertainties*

Neutron Source	Spacing Number 1	2	3	4	5	6	7
Sb-Be	0.0166 (0.86)	0.00689 (1.05)	0.00374 (1.11)	0.00236 (1.15)	0.00164 (1.18)	0.00120 (1.21)	0.000913 (1.27)
Na-D_2C	0.0224 (0.85)	0.00795 (1.99)	0.00405 (1.09)	0.00248 (1.18)	0.00168 (1.20)	0.00122 (1.26)	0.000917 (1.32)
La-Be	0.0216 (0.63)	0.0070 (0.78)	0.00395 (0.84)	-	-	-	-
Na-Be	0.0213 (0.58)	0.00762 (0.64)	0.00392 (0.72)	0.00238 (0.76)	0.00162 (0.80)	0.00118 (0.83)	0.000884 (0.88)

*Uncertainties are in the parentheses below the flux and are reported in %.

where $\phi(r)$ = spacing-dependent flux

$= (\phi_o + \delta\phi_o)S_o$

$\bar{\sigma}$ = $In^{115}(n,\gamma)$ cross section averaged over the neutron energy spectrum

N' = number of In^{115} target nuclei (units of 10^{24})

$\overline{\sigma\phi}_{RR}$ = room-return induced saturated activity per target atom

= constant for a particular source

The spacing-independent room-return activity is the intercept of a plot of the A_∞/N' data versus the spacing-dependent flux, $\phi(r)$.

This graphical analysis was performed for the spacing data of each of the four sources. Figure 7.C.1 is the plot obtained for the data of the Sb-Be source. The straight line through the data is the result of the linear least squares regression performed to determine the saturated activity intercepts. The linear correlation coefficient for all four fits was greater than $r^2 = 0.999$, suggesting virtually perfect linearity.

Room-return saturated activity results are most informatively presented as the fraction of the total activity observed at each spacing. These results are summarized in Table 7.C.1. The uncertainty associated with the room-return activity results was investigated parametrically. Uncertainties associated with both the

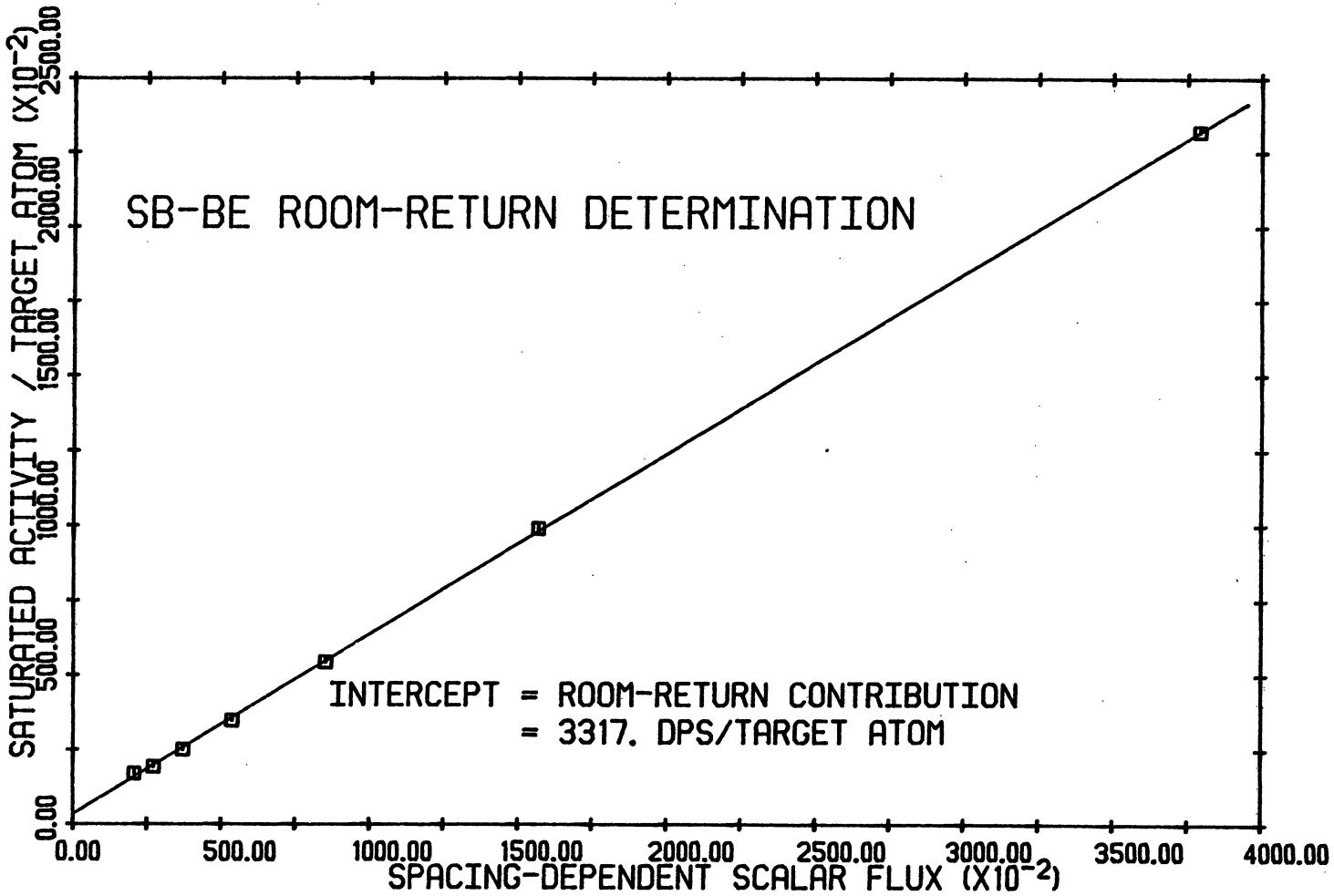

Figure 7.C.1. Sb-Be Room-Return Determination

Table 7.C.1

Fraction of Total In^{116m} Activity Due to Room-Return Contribution

Spacing #	Sb-Be	Na-D_2C	La-Be	Na-Be
1	0.014	0.008	0.029	0.010
2	0.034	0.023	0.079	0.029
3	0.061	0.045	0.136	0.053
4	0.095	0.074	-	0.086
5	0.132	0.107	-	0.109
6	0.172	0.145	-	0.160
7	0.195	0.159	-	0.214

ordinate and abscissa values of the plots precluded the use of error weighted, linear least squares regression for the error propagation analysis of the intercept. Regression techniques handle uncertainties in only one variable. The approach used here was to determine the intercept (room-return activity) sensitivity to changes in $\phi(r)$, the abscissa. Individual spacing fluxes were modified by up to two of their associated standard deviations. Least squares regressions were run for a variety of combinations of these modified fluxes. The result was a set of $\overline{\sigma\phi}_{RR}$ values. Uncertainty in room-return correction was then taken as the maximum deviation from the mean value of the set of $\overline{\sigma\phi}_{RR}$ activities. Resulting

uncertainties are quoted in terms of the percent of the room-return correction and were 15%, 20%, 14% and 12% for Sb-Be, Na-D_2C, La-Be and Na-Be, respectively.

All of the quantities of equation 7.C.1, except for $\bar{\sigma}$, the indium capture cross section, are now known. A set of seven (three for La-Be) cross sections, one for each spacing, was calculated for each source. A single cross section for each source was then calculated as an error weighted average. The resulting $In^{115}(n,\gamma)In^{116m}$ apparent cross sections are listed in Table 7.C.2. Uncertainties reflect propagation of error for all of the terms in equation 7.C.1.

Table 7.C.2

Apparent $In^{115}(n,\gamma)In^{116m}$ Cross Section Results

Source	Cross Section (mb)*
Sb-Be	592. ± 12. (2.01%)
Na-D_2C	206. ± 4. (1.92%)
La-Be	281. ± 10. (3.58%)
Na-Be	203. ± 3. (1.58%)

*Values in parentheses are the percent error in the cross section result.

7.D. Neutron Energy Spectrum

The measured indium capture cross sections were averages over the neutron energy spectra of the photoneutron sources. A normalization of these experimental values, $\bar{\sigma}$, to the cross section, σ, at the median neutron energy of the sources (23, 265, 770 and 964 keV) was performed. The source-dependent correction required to reduce $\bar{\sigma}$ to σ was calculated from

$$CF_s = \frac{\sigma}{\bar{\sigma}} = \frac{1}{\sum_i \frac{\sigma(E_i)}{\sigma(E_I)} f_i} \qquad 7.D.1$$

where: $\frac{\sigma(E_i)}{\sigma(E_I)}$ = (n,γ) cross section in the i^{th} energy bin relative to the cross section in energy bin I, which contains the source median energy

f_i = fraction of source neutrons in the i^{th} energy bin

The correction factor is simply a weighting of the $In^{115}(n,\gamma)In^{116m}$ cross section shape data from ENDF/B-IV with the calculated neutron energy distribution results of VES.

The correction factors calculated were 0.994, 0.945, 1.025 and 0.999 for the Sb-Be, Na-D_2C, La-Be and Na-Be source, respectively. An uncertainty of 10% of the correction (i.e. 0.945 ± 0.006 for Na-D_2C) was assigned. This reflects uncertainty in the cross section shape data (~3%)

and the slight sensitivity of the correction to the calculated neutron energy spectrum uncertainty (ENG 78).

Although not included in the VES analysis of the Sb-Be source, approximately 4.4% (ENG 78) of the neutrons are produced with an energy of about 375 keV. The effect of these neutrons have been included in the spectrum correction analysis.

The final $In^{115}(n,\gamma)In^{116m}$ cross sections were calculated from the results in Table 7.C.2 corrected for the energy spectrum effects of this section. These derived cross section values and associated uncertainties are summarized in Table 7.D.1.

Table 7.D.1

Derived $In^{115}(n,\gamma)In^{116m}$ Cross Section Results

Source	Energy (keV)	Cross Section (mb)
Sb-Be	23	588. ± 12. (2.02%
Na-D_2C	265	196. ± 4. (1.98%)
La-Be	770	288. ± 10. (3.59%)
Na-Be	964	203. ± 3. (1.58%)

CHAPTER 8

CONCLUSIONS

8.A. Comparison with Other Measurements

The $In^{115}(n,\gamma)In^{116m}$ absolute cross sections measured here are 588±12, 196±4, 288±10 and 203±3 millibarns at the neutron energies 23, 265, 770 and 964 keV, respectively. These values are absolute in that they do not depend upon any other cross section data, except for the correction factors amounting to less than 10%. The significance of these measurements is that they provide several accurate reference points to locate the absolute value of the more easily generated relative cross section data. In addition, these results provide absolute cross section data at neutron energies where no other absolute measurements have been performed.

In the energy region covered by this work, only two other absolute measurements have been performed. These data, the results of the present work and the ENDF/B-IV evaluation are plotted in figure 8.A.1. The 154 and 195 keV results of Ryves, et.al. (RYV 73) and the 265 keV result of this work are in close agreement with the ENDF evaluation. The 231 keV measurement of Ryves, however, is about 10% below ENDF and the three remaining higher energy measurements are all about 20% lower than the

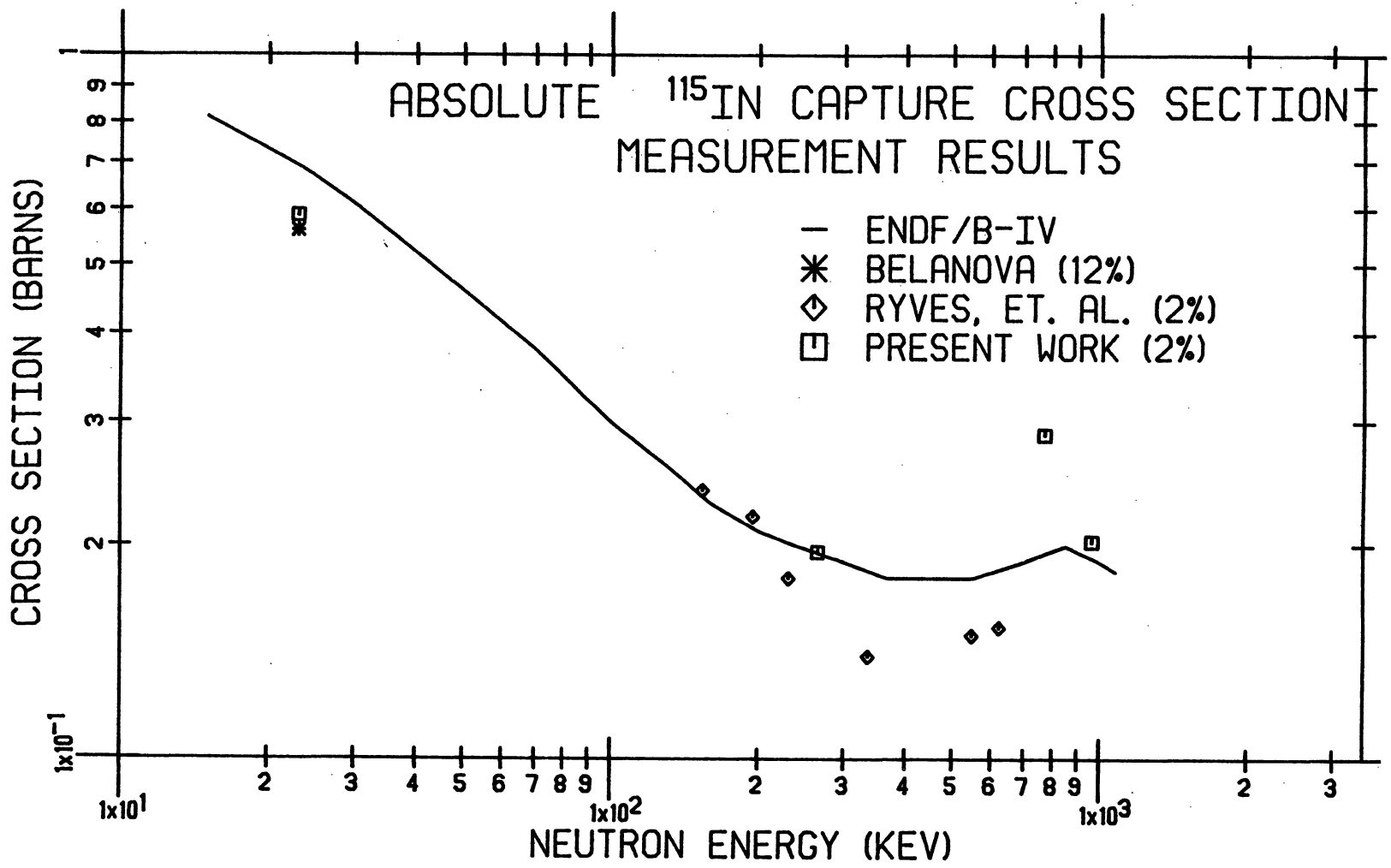

Figure 8.A.1. Absolute $In^{115}(n,\gamma)In^{116m}$ Cross Section

evaluation. These discrepancies suggest the possibility of a systematic error in the flux determinations of Ryves. The fluxes were measured with a long counter calibrated with Sb-Be (23 keV), Ra-Be (260 keV) and Na-Be (964 keV) photoneutron sources. The area of cross section disagreement falls between the last two calibration points where the long counter efficiency increases by over 10%.

The other absolute measurement was made by Belanova, et. al. (BEL 66) using an Sb-Be photoneutron source and the transmission beam method in spherical geometry. Direct comparison of results of the present work with the Belanova value is difficult. The transmission technique results in the absorption cross section of indium (i.e., $In^{115}(n,\gamma)$ $In^{116m} + In^{116g}$). An estimate of the $In^{115}(n,\gamma)In^{116m}$ cross section from the Belanova work can be made using the 220 $\pm$30 mb $In^{115}(n,\gamma)In^{116g}$ cross section of Chaubey and Sehgal (CHA 65). The resulting Belanova value of 560$\pm$66 mb is in very good agreement with the result of this work.

A number of relative measurements have been performed and are compiled in figure 8.A.2. Around 23 keV, three measurements are directly applicable. Kononov, et. al. (KON 59) and Chaubey and Sehgal (CHA 65) have obtained cross sections of 590$\pm$20 mb and 580$\pm$40 mb, respectively, using Sb-Be photoneutron sources and activation techniques with $I^{127}(n,\gamma)I^{128}$ as the reference cross section. Rimawi and Chrien (RIM 75) measured a value of 582$\pm$32 mb utilizing

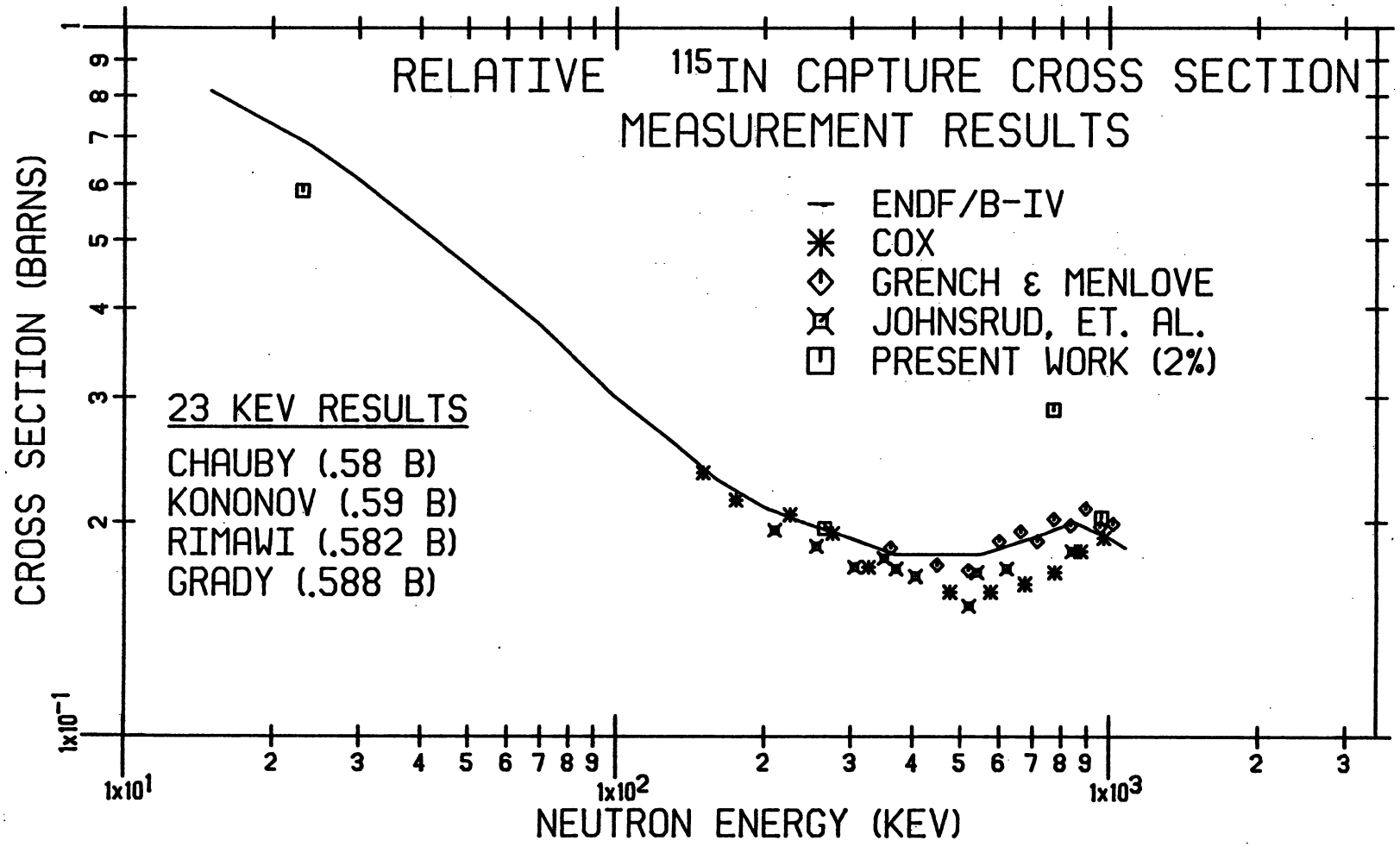

Figure 8.A.2. Relative $In^{115}(n,\gamma)In^{116m}$ Cross Sections

an iron filtered beam and activation techniques with dependence upon the $B^{10}(n,\alpha)$ cross section in the flux determination. These results were obtained using different approaches and different cross section references but are in excellent agreement with the 588±12 mb result of this work. All four results, however, are about 12% below the ENDF/B-IV value of 690 mb suggesting the need for re-evaluation of this data base in the 23 keV energy region.

Over the energy range of the three remaining measurements of this work (265 to 964 keV), three sets of relative data are available. The most recent work is by Grench and Menlove (GRE 68) and was performed relative to the $Au^{197}(n,\gamma)$ capture reaction. Cox (COX 64) made measurements on the interval from 150 to 975 keV relative to the $U^{235}(n,f)$ cross section. Johnsrud, et. al. (JOH 59) also performed measurements on this same interval. Dependence upon both the indium thermal capture cross section and the U^{235} fission cross section in addition to a neutron energy spread of ± 0.1 MeV, however, makes direct comparison with this data set difficult.

At 265 keV, the Cox result (193 mb) agrees very well with the results of this work (196±4 mb) and the ENDF evaluation of 194 mb.

At 964 keV, the Grench value of 205 mb and the results of this work (203±3 mb) are in excellent agreement. The

Cox value (190 mb) and the ENDF evaluation of 190 mb are 6% lower.

The result from this work at 770 keV is about 30% above the ENDF value and that of both Cox and Grench. An explanation for the difference is not readily apparent. Re-examination of the experimental data did reveal inconsistencies in the counting data. Competing reaction corrected counts from the beta detector did not fit the In^{116m} decay half life. The possibility of a systematic error in the counting or activation (unaccounted competing reactions or radioactive contamination) was investigated and no self-consistent mechanism was defined. Although maximum indium foil activities were less than one count per second, this activity would be sufficient to obtain a cross section within an error of about 3.5%. A discrepancy with ENDF/B-IV and other experimental results is not grounds for dismissing this result. The decay inconsistency does, however, strongly suggest the presence of some undetermined systematic error.

8.B. Suggestion for Further Improvements

Some reduction in the systematic error associated with the source strength determination could be achieved with a recalibration of this Cf standard against NBS-II. The source half life uncertainty is a major contribution to the source strength error.

A measurement of the neutron energy spectrum for the photoneutron sources would provide a valuable test of the VES Monte Carlo program used to model the sources.

A measurement of the capture cross section using the La-Be and Ga-D_2C (140 keV) sources could be performed by wrapping the photoneutron sources with indium targets. Sufficient activities would be produced to make the measurements feasible. Performing a similar experiment with the Na-Be source could provide information about the neutron flux in this geometry. The resulting measurements would not be by definition, absolute, but they would be valuable additions to the $In^{115}(n,\gamma)In^{116m}$ cross section data base and interesting experiments to perform.

APPENDIX A

COMPUTER PROGRAM LISTINGS

A.1. STRENGTH

The program calculates the photoneutron source strength (with associated uncertainty) from the SAT2 saturated activity results for the photoneutron source and up to two standard calibrations. Input to the program is done through the namelist INPUT. The input variables and their default values are described in the comment cards at the beginning of the program listing which begins on the following page.

```
C   PROGRAM "STRENGTH"   OBJ:STRENGTH.O    AUTHOR:D. GRADY    MARCH 1979
C   PROGRAM CALCULATES THE PHOTONEUTRON SOURCE STRENGTH (WITH ERROR)
C   FROM THE "SAT2" ACTIVITY RESULTS FOR THE PHOTONEUTRON SOURCE
C   AND UP TO TWO "STANDARD" CALIBRATION RUNS.  INPUT ALSO REQUIRES
C   THE TIME AND DATE INFORMATION FOR EACH OF THE "SAT2" RUNS.
C
C    ** INPUT VARIABLE DEFINITION AND DESCRIPTION **
C
C       -UNNOWN :  2X2 MATRIX WITH ROW #1 CONTAINING "SAT2" ACTIVITY VALUES FOR
C                  COMPLETE (BUILD-UP,DECAY) FOR THE UNKNOWN P.N. SOURCE.
C                  ROW #2 CONTAINS THE ASSOCIATED ERRORS.
C
C       -CAL    :  2X4 MATRIX WHICH IS THE SAME AS "UNNOWN" EXCEPT THAT IT IS
C                  FOR ONE OR TWO STANDARD CALIBRATION RUN RESULTS.
C
C       -DATE   :  4X3 MATRIX CONTAINING DATE OF EACH OF THE SOURCE RUNS AND THE
C                  DATE OF THE ORIGINAL CALIBRATION.  ORDER IS UNKNOWN,
C                  STANDARD #1, STANDARD #2, ORIGINAL CALIBRATION.
C                    * DEFAULT FOR ORIG. CALIB.: 12:00:00 ON 8/21/77 *
C
C       -TIME   :  4X3 MATRIX WHICH IS THE SAME AS "DATE" EXCEPT THAT IT
C                  CONTAINS TIME DATA.
C
C       -NCAL   :  THE NUMBER OF STANDARD CALIBRATION RUNS PROVIDED.
C                  (NCAL=0  -TERMINATES THE PROGRAM)
C                    * DEFAULT: NCAL=0 *
C
C       -NS     :  THE NUMBER OF THE PHOTONEUTRON SOURCE BEING CALIBRATED.
C                    * DEFAULT: NS=3 *
C                       NUMBERING SCHEME IS AS FOLLOWS:
C                             NS= 1   SOURCE= NBS-II
C                             NS= 2   SOURCE= CF-252
C                             NS= 3   SOURCE= NA-BE
C                             NS= 4   SOURCE= LA-BE
C                             NS= 5   SOURCE= NA-D2C
C                             NS= 6   SOURCE= GA-D2C
C                             NS= 7   SOURCE= SB-BE
C                             NS= 8   SOURCE= PU-BE
C
C       -NSCAL  :  THE NUMBER OF THE STANDARD SOURCE USING THE ABOVE SCHEME.
C                    * DEFAULT: NSCAL=2 *
C
C       -CF     :  8X2 MATRIX CONTAINING THE CORRECTION FACTORS AND THEIR
C                  ERRORS (%) FOR THE SEVEN SOURCES ABOVE.
C                    * DEFAULT: SEE PAGE 21 OF BOOK #15 *
C
C       -ADDERR :  THE ADDITIONAL ERROR ASSOCIATED WITH THE ORIGINAL SAT2 RESULTS.
C                    * DEFAULT: ADDERR=.27% *
C
C       -DECAY  :  VECTOR CONTAINING EFFECTIVE DECAY CONSTANT, INSTANTANEOUS
C                  DECAY CONSTANT AND THE % ERROR IN BOTH VALUES.  IF "NSCAL"=2,
C                  ALL THREE VALUES ARE PROGRAM CALCULATED.
C                    * DEFAULT: DECAY=0.,0.,0. *
C
C       -SO     :  VECTOR CONTAINING STANDARD NEUTRON SOURCE STRENGTH AND
C                  ITS PERCENT ERROR.
C                    * DEFAULT: SO=6.7879E6 +/- 0.58% (CF-252) *
C
C   ***NOTE: COMMENT CARDS IN THE PROGRAM REFER TO STEPS "1-8.  THESE COINCIDE
C            EXACTLY WITH THE STEPS DETAILED ON PAGES 34-38 OF BOOK #15.
C
      INTEGER DATE,TIME
      DIMENSION DATE(4,3),TIME(4,3),CAL(2,4),UNNOWN(2,2),CF(8,2),
     1          DECAY(3),SO(2),SU(2),CSA(3,2),DT(2),F(4),ID(2),TYPE(8,2)
      NAMELIST/INPUT/DATE,TIME,UNNOWN,CAL,NCAL,NS,NSCAL,CF,ADDERR,
     1               DECAY,SO,ID
C
C   DEFINE DEFAULT VALUES
```

```
C
      DATA CF/1.00814,1.01086,0.99445,0.99667,0.99818,1.00011,1.01361,1.00220,
     1        0.124,0.204,0.119,0.149,0.129,0.148,0.184,0.308/
      DATA TYPE/'NBS-','CF-2','NA-B','LA-B','NA-D','GA-D','SB-B','PU-B',
     1          'II  ','52  ','E   ','E   ','2C  ','2C  ','E   ','E   '/
      DATA DATE,TIME,NCAL,NS,NSCAL,ADDERR,DECAY,SO,CAL,UNNOWN,F/
     1     3*0,8,3*0,21,3*0,77,3*0,12,9*0,3,2,0.27,3*0.,6.7879E6,
     2     0.58,16*0./
    1 READ(5,INPUT)
      IF(NCAL.EQ.0)GO TO 999
C
C   *** STEP #1 ***
C

      CALL WEIGHT(CSA(1,1),CSA(1,2),2,1,UNNOWN)
        DO 10 I=1,NCAL

   10   CALL WEIGHT(CSA(I+1,1),CSA(I+1,2),4,I,CAL)
      NCAL1=NCAL+1
C
C   *** STEP #2 ***
C
        DO 20 I=1,NCAL1
   20   CSA(I,2)=SQRT((CSA(I,2)*100./CSA(I,1))**2+ADDERR**2)
C
C   *** STEP #3 ***
C
      CSA(1,1)=CSA(1,1)*CF(NS,1)
      CSA(1,2)=SQRT(CSA(1,2)**2+CF(NS,2)**2)
        DO 30 I=2,NCAL1
        CSA(I,1)=CSA(I,1)*CF(NSCAL,1)
   30   CSA(I,2)=SQRT(CSA(I,2)**2+CF(NSCAL,2)**2)
C
C   *** STEP #4 ***
C
        DO 40 I=1,NCAL1
   40   CALL YEARS(DATE,TIME,I,F)
        CALL YEARS(DATE,TIME,4,F)
      T=F(1)-F(4)
      IF(NSCAL.EQ.2)CALL LAMBDA(DECAY,T)
      F(2)=F(1)-F(2)
      IF(NCAL.EQ.2)F(3)=F(1)-F(3)
      CSA(2,1)=CSA(2,1)*EXP(-DECAY(2)*F(2))
      IF(NCAL.EQ.2)CSA(3,1)=CSA(3,1)*EXP(-DECAY(2)*F(3))
C
C   *** STEP #5 ***
C
      IF(NCAL.EQ.1)GO TO 50
      CSA(2,1)=(CSA(2,1)+CSA(3,1))/2.
      CSA(2,2)=SQRT(CSA(2,2)**2+CSA(3,2)**2)/2.
C
C   *** STEP #6 ***
C
   50 R=CSA(1,1)/CSA(2,1)
      DR=SQRT(CSA(1,2)**2+CSA(2,2)**2)
C
C   *** STEP #7 ***
C
      SO1=SO(1)*EXP(-T*DECAY(1))
      SO2=SQRT(SO(2)**2+(T*DECAY(3)*DECAY(1))**2)
C
C   *** STEP #8 ***
C
      SU(1)=R*SO1
      SU(2)=SQRT(SO2**2+DR**2)
C
C   *** WRITE OUT THE INPUT AND RESULTS OF THE PROGRAM ***
C
```

```
      WRITE(6,100) TYPE(NS,1),TYPE(NS,2),TYPE(NSCAL,1),TYPE(NSCAL,2),ID(1),ID(2)
  100 FORMAT('1CALCULATION OF THE PHOTONEUTRON SOURCE STRENGTH'/
     1       'O',7X,'P.N. SOURCE : ',2A4/
     2       ' ',10X,'STANDARD : ',2A4/
     3       ' ',5X,'SOURCE TAPE # : ',I2,'-',I2/
     4       'O  "SAT2" SATURATED ACTIVITY RESULTS ARE INPUTS :')
      WRITE(6,101)
  101 FORMAT('O',20X,'SATURATED ACTIVITY',3X,'ERROR',5X,'TIME',
     1       6X,'DATE'/'O   P.N. SOURCE :')
      WRITE(6,102) (UNNOWN(1,I),UNNOWN(2,I),(TIME(1,J),J=1,3),
     1             (DATE(1,J),J=1,3), I=1,2)
  102 FORMAT(' ',25X,F8.3,7X,F7.5,2X,I2,':',I2,':',I2,I4,'/',I2,'/',I2)
      K=2
        DO 80 I=1,NCAL
        J=(I-1)*2+1
        JJ=J+1
        WRITE(6,103)
        WRITE(6,102) (CAL(1,M),CAL(2,M),(TIME(K,L),L=1,3),
     1               (DATE(K,L),L=1,3), M=J,JJ)
   80   K=3
  103 FORMAT('O      STANDARD :')
      WRITE(6,104) (DECAY(I), I=1,3)
  104 FORMAT('O  QUANTITIES CALCULATED BY THE PROGRAM'/
     1       'O      EFFECTIVE DECAY CONSTANT :',E13.6/
     2       '   INSTANTANEOUS DECAY CONSTANT :',E13.6/
     3       '      % ERROR IN DECAY CONSTANT :',E13.6)
      WRITE(6,105) SU(1),SU(2),SO1,SO2,(TIME(1,J),J=1,3),
     1             (DATE(1,J),J=1,3)
  105 FORMAT('-***CALCULATED NEUTRON SOURCE STRENGTHS***'/
     1       'O  P.N. SOURCE :',E12.5,' +/-',F7.4,' %'/
     2       'O     STANDARD :',E12.5,' +/-',F7.4,' %'/
     3       'O  **SOURCE STRENGTHS AT',I3,':',I2,':',I2,'  ON',I3,
     4       '/',I2,'/',I2)
      GO TO 1
  999 CONTINUE
      END


C
C   THE SUBROUTINE "YEARS" CALCULATES THE RELATIVE TIME GIVEN THE DATE
C   AND THE TIME OF A MANGANESE BATH RUN.  THIS VALUE WILL BE USED LATER
C   TO DETERMINE THE VARIOUS TIME DIFFERENCES NEEDED IN THE DETERMINATION
C   OF THE NEUTRON SOURCE STRENGTHS.
C
      SUBROUTINE YEARS(DATE,TIME,I,F)
      INTEGER DATE,TIME
      DIMENSION DATE(4,3),TIME(4,3),F(4)
      IF(DATE(I,1).LE.2)GO TO 20
      INT1=.4*DATE(I,1)+2.3
      INT2=(1900+DATE(I,3))/4
      F(I)=365*(1900+DATE(I,3))+DATE(I,2)+31*(DATE(I,1)-1)-INT1+INT2-15
      GO TO 30
   20 INT1=(1899+DATE(I,3))/4
      F(I)=365*(1900+DATE(I,3))+DATE(I,2)+31*(DATE(I,1)-1)+INT1-15
   30 F(I)=(F(I)+TIME(I,1)/24.+TIME(I,2)/24./60+TIME(I,3)/24./3600)/365.25
      RETURN
      END


C
C   THE SUBROUTINE "LAMBDA" IS USED ONLY WHEN THE CF-252 SOURCE IS USED
C   AS THE CALIBRATION SOURCE OR STANDARD.  THE ROUTINE CALCULATES THE
C   EFFECTIVE DECAY CONSTANT, THE INSTANTANEOUS DECAY CONSTANT AND THE
C   PERCENT ERROR IN BOTH VALUES.
C
      SUBROUTINE LAMBDA(DECAY,T)
      DIMENSION DECAY(3)
C
```

```
C   *** CALCULATE THE EFFECTIVE DECAY CONSTANT FOR THE CF-252 SOURCE ***
C
      DCO=.052993
      DC2=.262755
      ALPHA=2.6495E-3
      C=(1.+ALPHA)/(((1.-EXP(-DC2*T))/DC2+ALPHA*(1.-EXP(-T*DCO))/DCO))
      DECAY(1)=DC2
        DO 10 I=1,5
   10   DECAY(1)=C*(1.-EXP(-DECAY(1)*T)*(1.+T*DECAY(1)))/
     1            (1.-C*T*EXP(-DECAY(1)*T))
      DECAY(3)=.013*DECAY(1)/ALOG(2.)*100.
C
C   *** CALCULATE THE INSTANTANEOUS DECAY CONSTANT FOR THE CF-252 SOURCE ***
C
      A=EXP(-T*(DCO-DC2))
      DECAY(2)=(DC2+DCO*A*ALPHA)/(1.+ALPHA*A)
      RETURN
      END
C
C
C     SUBROUTINE WEIGHT WAS DERIVED FROM SAT2 AND TAKES THE WEIGHTED
C     SUM OF THE UNKNOWN "ACTIVITY" AS WELL AS THE CALIBRATION
C     "ACTIVITY"
C
C
      SUBROUTINE WEIGHT(CSA1,CSA2,NCOL,I,INFO)
      REAL INFO
      DIMENSION INFO(2,NCOL)
      SUMACT=0.
      SUMSIG=0.
      SIG=0.
      NLOW=I*3/2
      NHIGH=I*2
      DO 1  J=NLOW,NHIGH
        SIG=1./(INFO(2,J)*INFO(2,J))
        SUMSIG=SUMSIG+SIG
    1   SUMACT=SUMACT+INFO(1,J)*SIG
      CSA1=SUMACT/SUMSIG
      CSA2=1./SQRT(SUMSIG)
      RETURN
      END
```

A.2. PHIBAR

The program calculates the area averaged flux over the surface of a disk target, a distance ZD away from the center of the photoneutron source. The flux calculation is based upon the fifth order polynomial expansion of the neutron emission angular distribution from the surface of the source. The program also calculates the volume average scalar flux using a Simpson's Rule numerical integration. Input to the program is provided through the namelist INPUT. A description of the input variables is included below:

F = the coefficients of the fifth order polynomial fit

RS = photoneutron source radius

RD = indium foil radius

ZD = source-target spacing

NS = number of horizontal slices through the target foil for the volume integration

TD = indium foil thickness

A1 = the fit normalization constant, A_n

```
C    PROGRAM "PHIBAR"    D. GRADY     DEC., 1980
C    THE PROGRAM CALCULATES THE AVERAGE SCALAR FLUX AT A DISK TARGET,
C    A DISTANCE 'ZD' AWAY FROM THE CENTER OF THE PHOTONEUTRON SOURCE.
C    IN ADDITION, IT CALCULATES A NUMERICALLY VOLUME AVERAGED SCALAR
C    FLUX FOR THE SAME DISK WITH THICKNESS 'TD'.
C    THE PROGRAM UTILIZIES ONE OF THE TWO METHODS BELOW:
C       1. FIFTH ORDER POLYNOMIAL FIT TO F(MU)
C       2. TWO PIECE - THIRD ORDER POLYNOMIAL FIT TO F(MU)   .
C    WHERE F(MU) IS OBTAINED FROM THE "VES" MONTE CARLO PROGRAM.
C
      IMPLICIT REAL*8 (A-H,O-Z)
      REAL*8 MUO
      LOGICAL*1 TITLE(50),BLANK
      EXTERNAL PHI2N
      DIMENSION F(5),G(3),H(4),ZL(2),PHI(21)
      COMMON /DATA/A,ATA,AA,BB,CC,RS2
      EQUIVALENCE (F(1),F1),(F(2),F2),(F(3),F3),(F(4),F4),(F(5),F5)
      EQUIVALENCE (G(1),G1),(G(2),G2),(G(3),G3)
      EQUIVALENCE (H(1),HO),(H(2),H1),(H(3),H2),(H(4),H3)
      NAMELIST /INPUT/F,G,H,RS,MUO,RD,ZD,NC,RERR,TITLE,TD,NS
      DATA MUO,RD,PI,RERR,NC,IER/0.57D0,0.9525D0,3.1415927D0,1.D-7,1,0/
      DATA BLANK/' '/
C
C    FUNCTION STATEMENTS
C
      PHI1(X)=((C1*ZDRS2-C2)*ZDRS2+C3)*ZDRS2+
     1         C4*(DLOG(X+QSR)-X/RS2*QSR)+
     2         C5*X*Q**1.5D0/(3.D0*RS3*RS)
     3        -C1*X*Q**2.5D0/(RS5*RS)+
     4         (AA*(Z5-RS5)+BB*(Z3-RS3)+CC*(X-RS))*DLOG(ZMRS)
     5        -(AA*(Z5+RS5)+BB*(Z3+RS3)+CC*(X+RS))*DLOG(ZPRS)
     6        -(AA*(Z2*0.5D0+RS2)+BB)*Z2*RS
C
      PHI2A(X)=(((C1*ZDRS+C2)*ZDRS-C3)*0.5D0*ZDRS+C4)*X+
     1          (G1+G3*(0.5D0-Q/(3.D0*RS2)))*X*QSR/(2.D0*RS)+
     2          (H0*ZMRS-H2/(2.D0*RS2)*(Z3/3.D0-X*RS2+2.D0*RS3/3:D0))*
     3          DLOG(ZMRS)-G2*RS/6.D0*DLOG(ZPRS/ZMRS)+
     4          G2*X/(4.D0*RS2)*(Z2/3.D0-RS2)*DLOG(Q)
     5         -C5*RS/2.D0*DLOG(X+QSR)+C6/RS*(X*DSQRT(Q+ATA)+
     6          (ATA-RS2)*DLOG(X+DSQRT(Q+ATA)))
C
C    READ THE NAMELIST DATA
C
    1 READ(5,INPUT)
      IF(NC.LT.1.OR.NC.GT.2)GO TO 999
      N=NS/2
      CHCK=DFLOAT(NS)/2.D0-DFLOAT(N)
      IF(CHCK.GT.0.1D0.OR.NS.LT.2.OR.NS.GT.20)GO TO 998
      IF(NC.EQ.2)GO TO 10
      A1=F1/2.D0+F2/3.D0+F3/4.D0+F4/5.D0+F5/6.D0
      RS5=RS**5.D0
      RS3=RS**3.D0
      AA=-3.D0*F4/(8.D1*RS5)
      BB=(2.D0*F2+3.D0*F4)/(2.4D1*RS3)
      CC=-(4.D0*F2+3.D0*F4)/(1.6D1*RS)
      C1=4.D0*F5/4.5D1
      C2=F3/6.D0+3.D0*F4/3.2D1+F5/3.D0
      C3=(F1+0.5D0*F2+F3+0.625D0*F4+F5)*0.5D0
      C4=(F1+0.5D0*F3+F5/3.D0)*0.5D0
      C5=0.5D0*F3+F5/3.D0
      GO TO 20
   10 A2=((((G3-H3)*MUO/4.D0+(G2-H2)/3.D0)*MUO+(G1-H1)/2.D0)*MUO
     1    -H0)*MUO+H0+H1/2.D0+H2/3.D0+H3/4.D0
      RS2=RS*RS
      RS3=RS2*RS
      AA=-H0
      BB=(G2-H2)/(4.D0*RS2)
      CC=(G3-H3)/(8.D0*RS3)
      C1=H3/3.D0
      C2=(H2-G2)/9.D0
```

```
      C3=H1+H2/3.DO+H3
      C4=(G2-3.DO*HO-H2)/3.DO
      C5=G1+G3/2.DO
      C6=(H1-G1)*O.5DO
   20 RS2=RS*RS
      RS5=RS**5.DO
      A=RS*MUO
      ATA=A*A
      DH=TD/DFLOAT(NS)
      NS1=NS+1
        DO 8O I=1,NS1
   80   PHI(I)=O.DO
      DO 6O J=1,NS1
      ZL(1)=DABS(ZD)+DFLOAT(J-1)*DH
      ZL(2)=DSQRT(ZL(1)**2.DO+RD**2.DO)
      SIGN=-1.DO
        DO 3O I=1,2
        Z=ZL(I)
        Z2=Z*Z
        Z3=Z2*Z
        Z5=Z3*Z2
        ZDRS=Z/RS
        ZDRS2=ZDRS*ZDRS
        Q=Z2-RS2
        QSR=DSQRT(Q)
        ZMRS=Z-RS
        ZPRS=Z+RS
        IF(NC.EQ.2)GO TO 4O
        PHI(J)=PHI(J)+PHI1(Z)*SIGN/A1
        GO TO 3O
   40   PHI(J)=PHI(J)+PHI2A(Z)*SIGN/(-A2*RS)
   30   SIGN=1.DO
      IF(NC.EQ.2)PHI(J)=PHI(J)+QNCS(PHI2N,ZL(1),ZL(2),RERR,ERROR,IER)/(-A2*RS)
   60 CONTINUE
      PHIV=PHI(1)+PHI(NS1)+4.DO*PHI(2)
      IF(NS.EQ.2)GO TO 9O
        DO 7O I=3,NS,2
   70   PHIV=PHIV+2.DO*PHI(I)+4.DO*PHI(I+1)
   90 PHIV=PHIV*DH/(6.DO*PI*RD*RD*TD)
      PHI(1)=PHI(1)/(2.DO*PI*RD*RD)
      WRITE(6,200)
  200 FORMAT('1AREA AVERAGED SCALAR FLUX DETERMINATION:'/'+',
     1       39('_')/
     2       'O    - NORMALIZED TO UNIT SOURCE STRENGTH'/
     3       '     - SPHERICAL NEUTRON SOURCE - PERPENDICULAR',
     4       ' DISK TARGET GEOMETRY'/
     5       '     - MONTE CARLO GENERATED NEUTRON EMISSION',
     6       ' ANGULAR DISTRIBUTION')
      WRITE(6,201) (TITLE(I), I=1,5O),NC,MUO,RS,RD,TD,ZD,ZL(2),ZL(1)
  201 FORMAT('-  INPUT PARAMETERS:  (FIT CODE -  1 = FIFTH',
     1       ' ORDER,  2 = TWO PIECE, THIRD ORDER)'/
     2       'O',2OX,'TITLE : ',5OA1/
     3       ' ',12X,'FIT TECHNIQUE : ',I1/
     4       ' ',11X,'FIT TRANSITION : ',F9.6/
     5       ' ',12X,'SOURCE RADIUS : ',F1O.7,' CM'/
     6       ' ',12X,'TARGET RADIUS : ',F1O.7,' CM'/
     6       ' ',9X,'TARGET THICKNESS : ',F1O.7,' CM'/
     7       ' ',4X,'SOURCE-TARGET SPACING : ',F1O.7,' CM'/
     8       'O',7X,'INTEGRATION LIMITS -   UPPER : ',F1O.7,
     9       ' CM'/' ',3OX,'LOWER : ',F1O.7,' CM')
      IF(NC.EQ.1)WRITE(6,202) (F(I), I=1,5)
      IF(NC.EQ.2)WRITE(6,203) (G(I), I=1,3),(H(I), I=1,4)
  202 FORMAT('O',9X,'FIT COEFFICIENTS -   F1 :',E14.6/31X,
     1       'F2 :',E14.6/31X,'F3 :',E14.6/31X,'F4 :',E14.6/
     2       31X,'F5 :',E14.6)
  203 FORMAT('O',9X,'FIT COEFFICIENTS -   G1 :',E14.6/31X,
     1       'G2 :',E14.6/31X,'G3 :',E14.6//31X,'HO :',E14.6/
     2      31X,'H1 :',E14.6/31X,'H2 :',E14.6/31X,'H3 :',E14.6)
      WRITE(6,204) PHI(1),IER
  204 FORMAT('- AREA AVERAGED SCALAR FLUX =',E14.7,' CM**(-2)',
```

```
     1       '  (IER =',I3,')')
      WRITE(6,205) PHIV,NS
  205 FORMAT('- NUMERICALLY VOLUME AVERAGED SCALAR FLUX =',E14.7,
     1       ' CM**(-2)  (NS =',I3,')')
      IF(ZD.LT.0.DO)GO TO 1
        DO 50 I=1,50
   50   TITLE(I)=BLANK
      GO TO 1
  998 WRITE(6,206)
  206 FORMAT(' THE VALUE OF "NS" MUST BE EVEN AND BETWEEN 2 AND 20.')
  999 CONTINUE
      END


      FUNCTION PHI2N(Z)
      REAL*8 A,AA,ATA,BB,CC,Q,PHI2N,Z
      COMMON /DATA/A,ATA,AA,BB,CC,RS2
      Q=Z**2.DO-RS2
      QATAS=DSQRT(Q+ATA)
      PHI2N=(AA-2.DO*BB*Q)*DLOG(QATAS-A)+
     1      (BB*0.5DO-CC*(QATAS-A)/3.DO)*(QATAS-A)**2.DO
     2     -(BB*0.5DO+CC*Q/(3.DO*(QATAS-A)))*Q*Q/(QATAS-A)**2.DO+
     3      CC*6.DO*Q*QATAS
      RETURN
      END
```

A.3. HISTO.FLUX and FLUX

The program calculates the area averaged scalar flux over the surface of a disk target using only the emission angular distribution histogram results from VES. The program can also calculate the area averaged flux for target displacements away from the center-center configuration normally assumed. This calculation is also performed with the histogram data but requires an expensive double numerical integration. Input to the program is provided through the namelist INPUT. A description of the input variables is included below.

RS = photoneutron source radius

RD = indium foil radius

ZD = source-target spacing

DELTA = indium foil misalignment from the normal center-center configuration

N = number of angular integration steps

M = number of radial integration steps

F = emission angular distribution histogram data

ISTOP = 2 - read in the emission angular distribution

= 0 - terminate the program after this run

- otherwise, use the previous emission angular distribution data

```
C  PROGRAM "HISTO.FLUX"  OBJ:"HISTO.FLUX.O"  AUTHOR: D. GRADY  MARCH, 1981
C   PROGRAM CALCULATES AREA AVERAGED SCALAR FLUX FOR A DISK
C   PERPENDICULAR TO THE SOURCE-TARGET AXIS USING ONLY THE EMISSION
C   ANGULAR DISTRIBUTION HISTOGRAM.  CODE ALSO CALCULATES THE AREA AVERAGED
C   SCALAR FLUX FOR TARGET DISPLACEMENTS AWAY FROM CENTER-CENTER
C   CONFIGURATIONS BY DOUBLE NUMERICAL INTEGRATION.
C
      IMPLICIT REAL*8 (A-H,O-Z)
      DIMENSION F(20),AMU(21),R(21)
      LOGICAL*1 TITLE(60)
      NAMELIST /INPUT/RS,RD,ZD,DELTA,N,M,ISTOP,TITLE
      ISTOP=2
    5 READ(5,INPUT)
      IF(ISTOP.EQ.2)READ(4,100) (F(I), I=1,20)
  100 FORMAT(10X,E13.5)
      PI=3.14159265DO
C   CALCULATE THE 21 "MU" VALUES FOR THE HISTOGRAM INTEGRATION.
C
      DO 10 I=1,21
   10 AMU(I)=DFLOAT(I-1)*0.05DO
C
C   CALCULATE THE FLUX NORMALIZATION CONSTANT "A" AND THE ANGULAR AND
C   RADIAL INTEGRATION STEP SIZES.
C
      A=0.DO
      DO 11 I=1,20
   11 A=A+F(I)
      A=A*.05DO
      DX=RD/DFLOAT(M-1)
      DP=PI/DFLOAT(N-1)
      SUM=0.DO
      W=1.DO
C
C   CALCULATE THE RELATIVE FLUX ON A RECTANGULAR "R-THETA" GRID
C   WITH THE PROPER POINT WEIGHTING OF 1., 0.5, OR 0.25.
C
      DO 20 I=1,M
      IF(I.EQ.1.OR.I.EQ.M)W=W*.5DO
      X=DFLOAT(I-1)*DX
      DO 30 J=1,N
      WW=W
      IF(J.EQ.1.OR.J.EQ.N)W=W*.5DO
      P=DFLOAT(J-1)*DP
      Z2=ZD*ZD+DELTA**2.DO+X*X+2.DO*DELTA*X*DCOS(P)
      Z=DSQRT(Z2)
      DO 40 K=1,21
   40 R(K)=DSQRT(Z2-RS*RS*(1.DO-AMU(K)**2))-RS*AMU(K)
      DO 50 K=2,21
   50 SUM=SUM+F(K-1)*DLOG(R(K)/R(K-1))*X*W/Z
   30 W=WW
   20 W=1.DO
C   CALCULATE THE ACTUAL FLUX AND WRITE OUT THE APPROPRIATE
C   INFORMATION ABOUT THE PROBLEM.
C
      SUM=SUM*DX*DP/(-2.DO*PI*PI*A*RS*RD*RD)
      WRITE(6,200) TITLE,RS,RD,ZD,DELTA,M,N,SUM
  200 FORMAT('2AREA AVERAGED FLUX BY THE INTEGRATED HISTOGRAM ',
     1       'APPROACH:'/'+',56('_')/'-',13X,'TITLE: ',60A1/
     2       '       SOURCE RADIUS: ',F8.4,' CM'/
     3       '         DISK RADIUS: ',F8.4,' CM'/
     4       '       SOURCE-TARGET: ',F8.4,' CM'/
     5       '     ALIGNMENT DELTA: ',F8.4,' CM'/
     6       '        RADIUS STEPS: ',I4/
     7       '       ANGULAR STEPS: ',I4/
     8       '0     AREA AVERAGED SCALAR FLUX = ',E14.7,
     9       ' (CM**2)**(-1)')
      IF(ISTOP.EQ.0)GO TO 60
      GO TO 5
   60 CONTINUE
      END
```

A.4. PT-SCAT.A

The program calculates the return flux at the indium target due to neutrons scattered by experimental rig components. The program assumes a point source-point scatterer-point target simplification with an isotropic source and isotropic scattering (some scattering anisotropy can be included). The four possible scattering geometries discussed in section 7.A are available. A default library of cross sections and angular distribution data from BNL-325 and BNL-400, respectively, are included in the data file DFAULT at the end of the program listing. Input to the program is provided through the namelists INPUT and DFAULT. A description of the input variables is included below.

GEOM = 1 - cylindrical scatterer with axis perpendicular to source-target axis
= 2 - disk scatterer with source-disk axis perpendicular to source-target axis
= 3 - cylindrical scatterer with axis colinear with source-target axis
= 4 - disk scatterer with source-disk axis colinear with source-target axis

BACK = anisotropy option swith (1 = on)

NREG = number of regions into which the scatterer is divided (materials changes)

LEAD = 1 - read in cross section data from namelist DFAULT
- others, use old cross section data

RS = photoneutron source radius

Y = source-disk perpendicular distance

S = source-target spacing

ZD = target-disk perpendicular distance

NEN = number of neutron energies investigated

EN = neutron energies for which scattering contributions are calculated

A = molecular weight of scatterer

SIGS = macroscopic scattering cross sections

MATID = scattering material identification

F = Legendre polynomial expansion coefficients of the differential scattering cross sections

TGEOM = geometry titles

TSCAT = scatterer type (cylinder or disk)

```
C  PROGRAM "PT-SCAT.A"   OBJ: PT-SCAT.A.O   AUTHOR: D. GRADY    JAN., 1980
C   PROGRAM CALCULATES THE RETURN FLUX AT THE TARGET DUE TO NEUTRONS
C   SCATTERED BY EXPERIMENTAL RIG COMPONENTS.  THE PROGRAM ASSUMES A
C   POINT, ISOTROPIC SOURCE; A POINT SCATTERER (WITH USER OPTIONED
C   SCATTERING ANISOTROPY CAPABILITY); AND A POINT TARGET.
C   FOUR POSSIBLE GEOMETRIC SCATTERING CONFIGURATIONS ARE AVAILABLE
C   AND ARE DESCRIBED LATER IN THE PROGRAM.
C
C   A DEFAULT LIBRARY OF CROSS SECTIONS AND LEGENDRE COEFFICIENTS
C   FOR THE FOLLOWING MATERIALS:
C         CADMIUM
C         ALUMINUM
C         IRON
C         BRASS
C        .STAINLESS STEEL
C   ARE AVAILABLE TO THE USER IN THE FILE "PT-DFAULT".
C   THIS LIBRARY CONTAINS DATA BASE INFORMATION FOR ALL FIVE PHOTONEUTRON
C   SOURCE ENERGIES: 23, 140, 265, 770, 964 KEV.
C
C   $RUN PT-SCAT.A.O+NAAS:NAL 4=PT-DFAULT 5=USER INPUT 6=PROGRAM OUTPUT
C
      IMPLICIT REAL*8 (A-H,O-Z)
      DIMENSION EN(5),DELPHI(5),DEL(14,5),TS(14),NMAT(14),SIGS(5,6),
     1          Z(15),F(6,5,6),A(6)
      EXTERNAL GEOM1,GEOM2,GEOM3,GEOM4,FSCAT
      INTEGER GEOM,BACK
      LOGICAL*1 HEAD(80),MATID(15,6),TGEOM(52,4),TSCAT(8,4)
      COMMON /DATA/S,S2,RS2,Y2,ZD2,ZD,BACK
      COMMON /COEF/F,NMAT,I,J
      COMMON DELPHI,DEL
      NAMELIST /DFAULT/EN,A,SIGS,MATID,F,TGEOM,TSCAT
      NAMELIST /INPUT/GEOM,BACK,NREG,LEAD,RS,Y,S,ZD,RERR,NEN,NSKIP
C
C   INITIALIZE SOME VARIABLES & PROGRAM CONTROL PARAMETERS.
C
      BACK=1
      LEAD=1
      NSKIP=0
      NEN=5
      RERR=1.D-6
      RS=0.0D0
      Y=0.0D0
      S=0.0D0
      ZD=0.0D0
    1 DO 2 I=1,75
    2 DELPHI(I)=0.0D0
C
C   READ THE SCATTERING PROBLEM DEFINITION.  IF THE CONTROL PARAMETER
C   "LEAD"=1, EITHER CHANGES IN OR ADDITIONS TO THE CROSS SECTION LIBRARY
C   ARE TO BE READ IN FROM I/O UNIT #4.
C
      READ(5,INPUT)
      IF(LEAD.EQ.1)READ(4,DFAULT)
      IF(GEOM.LT.1.OR.GEOM.GT.4)GO TO 999
      S2=S*S
      Y2=Y*Y
      RS2=RS*RS
      ZD2=ZD*ZD
      NREG1=NREG+1
C
C   THE VARIOUS SCATTERING REGIONS ARE DEFINED.
C
      IF(NSKIP.EQ.1)GO TO 3
      READ(5,100) (Z(I),NMAT(I),TS(I), I=1,NREG1)
      READ(5,101) (HEAD(I), I=1,80)
  100 FORMAT(F10.5,I2,F10.5)
  101 FORMAT(80A1)
C
C   IF THIS IS THE FIRST PASS THROUGH THE PROGRAM OR IF THE DATA BASE
C   HAS JUST BEEN CHANGED, A BRIEF PROGRAM DESCRIPTION AND THE DATA BASE
```

```
C   INFORMATION IS PRINTED OUT.
C
    3 IF(LEAD.EQ.0)GO TO 19
      WRITE(6,200)
  200 FORMAT('1POINT APPROXIMATION SCATTERING CALCULATIONS'/
     1       '+',43('_')/'-     PROGRAM "PT-SCAT.A" UTILIZES:'/
     2       '          - POINT SOURCE'/
     3       '          - POINT SCATTERER'/
     4       '          - POINT TARGET'/
     5       '          - ISOTROPIC SOURCE'/
     6       '          - ANISOTROPIC SCATTERING (LIMITED)'/
     7       '- BASIC CODE PARAMETERS:'/'0      UNTIL RESTATED,',
     8       ' THE SCATTERING CALCULATIONS'/
     9       '       UTILIZED THE FOLLOWING DATA SETS-'/
     1       '-    MACROSCOPIC SCATTERING CROSS SECTIONS:'/
     1       '0       NEUTRON ENERGY',4X,'MATERIAL #1',4X,
     2       'MATERIAL #2',4X,'MATERIAL #3',4X,'MATERIAL #4',4X,
     3       'MATERIAL #5',4X,'MATERIAL #6'/' ')
        DO 10 I=1,NEN
   10   WRITE(6,201) EN(I),(SIGS(I,J), J=1,6)
  201 FORMAT(11X,F5.1,' KEV',6(8X,F7.5))
      WRITE(6,202)
  202 FORMAT('-    DIFFERENTIAL SCATTERING CROSS SECTION ',
     1       'LEGENDRE COEFFICIENTS:'/'0       NEUTRON ENERGY',
     2      4X,'MATERIAL #1',4X,'MATERIAL #2',4X,'MATERIAL #3',
     3      4X,'MATERIAL #4',4X,'MATERIAL #5',4X,'MATERIAL #6')
        DO 11 I=1,NEN
        WRITE(6,203) EN(I),(F(1,I,K), K=1,6)
        DO 12 J=2,6
   12   WRITE(6,204) (F(J,I,K), K=1,6)
   11   CONTINUE
  203 FORMAT('0',10X,F5.1,' KEV',6(8X,F7.2))
  204 FORMAT(20X,6(8X,F7.2))
      WRITE(6,205)
  205 FORMAT('-    SCATTERING MATERIAL IDENTIFICATION:'/' ')
        DO 13 I=1,6
   13   WRITE(6,206) I,(MATID(J,I), J=1,15),A(I)
  206 FORMAT(' ',7X,'MATERIAL #',I1,' - ',15A1,5X,'A =',F7.2)
C
C   THE RUN SPECIFIC INPUT PARAMETERS ARE PRINTED OUT.
C
   19 WRITE(6,207) HEAD,GEOM,(TSCAT(I,GEOM), I=1,8),
     1             (TGEOM(I,GEOM), I=1,52),S,RS,Y,ZD,NREG,RERR
  207 FORMAT('1 RUN SPECIFIC INPUT PARAMETER VALUES:'/
     1       '0          TITLE: ',80A1/
     2       '          "GEOM": ',I1/
     3       '       SCATTERER: ',8A1/
     4       '        GEOMETRY: ',52A1/
     5       '0             SOURCE-TARGET SPACING: ',F8.4,' CM'/
     6       '       CYLINDRICAL SCATTERER RADIUS: ',F8.4,' CM'/
     7       '                 SOURCE-DISK SPACING: ',F8.4,' CM'/
     8       '                 TARGET-DISK SPACING: ',F8.4,' CM'/
     9       '       NUMBER OF SCATTERING REGIONS: ',I2/
     1       '           RELATIVE ERROR PARAMETER: ',E12.4/
     1       '- RELATIVE SCATTERING RESULTS BY REGION:'/
     2       '0',13X,'INTEGRATION LIMITS',37X,'RELATIVE'/
     3       '   REGION       LOWER     UPPER        MATERIAL',7X,
     4       'SCATTERER     SCATTERING'/
     5       '   NUMBER        LIMIT     LIMIT          TYPE',9X,
     6       'THICKNESS    CONTRIBUTION'/' ')
C
C   LINES 92-101 HANDLE THE FIRST AND THIRD SCATTERING GEOMETRIES.
C
      GO TO (20,30,20,30),GEOM
   20   DO 40 I=1,NREG
        IF(TS(I).EQ.0.0D0)GO TO 40
        IF(GEOM.EQ.3)GO TO 45
   43   DO 44 J=1,NEN
        DEL(I,J)=QNCS(GEOM1,Z(I),Z(I+1),RERR,ERROR,IER)
   44   IF(BACK.EQ.1)DEL(I,J)=DEL(I,J)*FSCAT(-1.D0)
```

```
      GO TO 40
   45 DO 46 J=1,NEN
   46 DEL(I,J)=QNCS(GEOM3,Z(I),Z(I+1),RERR,ERROR,IER)
   40 IF(IER.NE.1)TS(I)=-TS(I)
      GO TO 50
C
C    LINES 103-112 HANDLE THE SECOND AND FOURTH SCATTERING GEOMETRIES.
C
   30 DO 60 I=1,NREG
      IF(TS(I).EQ.0.0D0)GO TO 60
      IF(GEOM.EQ.4)GO TO 65
   63 DO 64 J=1,NEN
      DEL(I,J)=QNCS(GEOM2,Z(I),Z(I+1),RERR,ERROR,IER)
   64 IF(BACK.EQ.1)DEL(I,J)=DEL(I,J)*FSCAT(-1.D0)
      GO TO 60
   65 DO 66 J=1,NEN
   66 DEL(I,J)=QNCS(GEOM4,Z(I),Z(I+1),RERR,ERROR,IER)
   60 IF(IER.NE.1)TS(I)=-TS(I)
C
C    THE RETURN FLUX AS A FUNCTION OF NEUTRON ENERGY IS SUMMED OVER
C    ALL THE REGIONS IN THE SCATTERING PROBLEM.
C
   50 DO 61 J=1,NEN
      DO 62 I=1,NREG
      DEL(I,J)=DEL(I,J)*S2*DABS(TS(I))/2.D0
      IF(GEOM.EQ.1.OR.GEOM.EQ.3)DEL(I,J)=DEL(I,J)*RS
   62 DELPHI(J)=DELPHI(J)+DEL(I,J)*SIGS(J,NMAT(I))
   61 CONTINUE
C
C    THE RESULTS OF THE RETURN FLUX CALCULATION ARE PRINTED OUT.
C
      WRITE(6,208) (I,Z(I),Z(I+1),(MATID(J,NMAT(I)), J=1,15),
     1              TS(I),DEL(I,1), I=1,NREG)
  208 FORMAT(5X,I2,7X,F8.4,2X,F8.4,3X,15A1,5X,F7.4,6X,F10.8)
      WRITE(6,209) HEAD,(EN(J),DELPHI(J), J=1,NEN)
  209 FORMAT('0'/'- TITLE: ',80A1/'- TOTAL SCATTERING CORRECTION BY ENERGY:'/
     1       '0    NEUTRON ENERGY     DELTA (PHI)'/'+',23X,11('_')/
     2       '     (UNITS OF KEV)        (PHI)'/' '/
     3       (10X,F5.1,10X,F9.7/))
      LEAD=0
      GO TO 1
  999 CONTINUE
      END


C    THE FOLLOWING FUNCTIONS HANDLE ONE EACH OF THE FOUR SCATTERING
C    GEOMETRIES:
C
C       GEOM1- CYLINDRICAL SCATTERER WHOSE AXIS IS PERPENDICULAR TO
C              THE SOURCE-TARGET AXIS.
C
C       GEOM2- DISK SCATTERER WHOSE SOURCE-DISK AXIS IS PERPENDICULAR
C              TO THE SOURCE-TARGET AXIS.
C
C       GEOM3- CYLINDRICAL SCATTERER WHOSE AXIS IS COLINEAR WITH
C              THE SOURCE-TARGET AXIS.
C
C       GEOM4- DISK SCATTERER WHOSE SOURCE-DISK AXIS IS COLINEAR WITH
C              THE SOURCE-TARGET AXIS.
C
      FUNCTION GEOM1(X)
      IMPLICIT REAL*8 (A-H,O-Z)
      INTEGER BACK
      EXTERNAL FSCAT
      COMMON /DATA/S,S2,RS2,Y2,ZD2,ZD,BACK
C
      X2=X*X
      GEOM1=1.D0/((RS2+X2)*DSQRT((X2+S2+RS2)**2-4.D0*S2*X2))
      RETURN
      END
```

```
      FUNCTION GEOM2(X)
      IMPLICIT REAL*8 (A-H,O-Z)
      INTEGER BACK
      EXTERNAL FSCAT
      COMMON /DATA/S,S2,RS2,Y2,ZD2,ZD,BACK
C
      X2=X*X
      GEOM2=X/((X2+Y2)*DSQRT((Y2+S2+X2)**2-4.DO*S2*X2))
      RETURN
      END


      FUNCTION GEOM3(X)
      IMPLICIT REAL*8 (A-H,O-Z)
      INTEGER BACK
      EXTERNAL FSCAT
      COMMON /DATA/S,S2,RS2,Y2,ZD2,ZD,BACK
C
      X2=X*X
      S12=RS2+(S-X)**2
      S22=RS2+X2
      GEOM3=1.DO/(S12*S22)
      IF(BACK.EQ.O)RETURN
      SMU=(S2-(S12+S22))/(2.DO*DSQRT(S12*S22))
      GEOM3=GEOM3*FSCAT(SMU)
      RETURN
      END


      FUNCTION GEOM4(X)
      IMPLICIT REAL*8 (A-H,O-Z)
      INTEGER BACK
      EXTERNAL FSCAT
      COMMON /DATA/S,S2,RS2,Y2,ZD2,ZD,BACK
C
      X2=X*X
      S12=(ZD-S)**2+X2
      S22=X2+ZD2
      GEOM4=X/(S12*S22)
      IF(BACK.EQ.O)RETURN
      SMU=(S2-(S12+S22))/(2.DO*DSQRT(S12*S22))
      GEOM4=GEOM4*FSCAT(SMU)
      RETURN
      END


C     THE FUNCTION "FSCAT" CALCULATES THE RATIO OF THE DIFFERENTIAL
C     SCATTERING CROSS SECTION TO THE ISOTROPIC SCATTERING CROSS SECTION.
C     THE FUNCTION TAKES THE SCATTERING ANGLE COSINE AS INPUT TO
C     DETERMINE THE EFFECTS OF SCATTERING ANISOTROPY.
C     THE FUNCTION IS UTILIZED ONLY IF THE CONTROL PARAMETER "BACK"=1.
C     THE ANISOTROPY CORRECTION IS LIMITED IN THAT ONLY 180 DEGREE
C     BACKSCATTERING CAN BE ACCOUNTED FOR IN THE CASES OF GEOM1 AND GEOM2
C     DUE TO THE COMPLEXITY OF THE EXPRESSION FOR THE SCATTERING ANGLE.
C
       FUNCTION FSCAT(SMU)
       IMPLICIT REAL*8 (A-H,O-Z)
       DIMENSION F(6,5,6),NMAT(14)
       COMMON /COEF/F,NMAT,I,J
C
       M=NMAT(I)
       FSCAT=(F(1,J,M)+
      1       F(2,J,M)*SMU+
      2       F(3,J,M)*.5DO*(3.DO*SMU*SMU-1.DO)+
      3       F(4,J,M)*.5DO*(5.DO*SMU**3-3.DO*SMU)+
      4       F(5,J,M)*.125DO*(3.5D1*SMU**4-3.D1*SMU**2+3.DO)+
      5       F(6,J,M)*6.25D-2*(1.26D2*SMU**5-1.4D2*SMU**3+
      6                3.D1*SMU))/F(1,J,M)
       END
```

```
C   CROSS SECTION LIBRARY FILE "PT-DFAULT"
C
 &DFAULT EN=22.8,140.,265.,770.,964.,
         A=112.4,26.98,55.85,64.28,55.36,0.,
         SIGS=.3453,.3291,.3291,.3152,.2966,
              .3255,.3014,.2230,.2562,.1959,
              .5552,.4026,.2882,.3009,.1992,
              .6407,.5047,.4182,.2822,.2586,
              .5711,.4374,.3097,.2856,.2166,5*0.0,
         MATID='      CADMIUM    ','     ALUMINUM    ',
               '       IRON      ','       BRASS     ',
               'STAINLESS STEEL','                 ',
         TGEOM='CYLINDER AXIS PERPENDICULAR TO SOURCE-TARGET AXIS   ',
               'SOURCE-DISK AXIS PERPENDICULAR TO SOURCE-TARGET AXIS',
               'CYLINDER AXIS COLINEAR WITH SOURCE-TARGET AXIS      ',
               'SOURCE-DISK AXIS COLINEAR WITH SOURCE-TARGET AXIS   ',
         TSCAT='CYLINDER','DISK     ','CYLINDER','DISK     ',
         F=596.97,121.21,4*0.,
           551.56,241.66,114.49,3*0.,
           647.8,613.4,386.7,27.2,45.3,-11.7,
           490.2,645.6,422.1,110.8,26.,58.3,
           445.6,623.,487.1,133.2,86.5,60.6,
           429.72,5*0.,
           397.89,5*0.,
           332.76,86.21,4*0.,
           348.5,146.,84.7,-2.1,14.3,0.,
           265.8,237.3,57.1,-2.1,-12.8,0.,
           521.23,5*0.,
           378.0,5*0.,
           284.9,112.2,65.8,6.6,21.4,4.,
           300.,169.2,204.,27.3,12.3,-9.9,
           163.9,161.3,164.7,42.6,4.9,-.2,
           648.56,5*0.,
           510.89,5*0.,
           425.,93.75,4*0.,
           300.8,117.,99.3,8.1,10.2,0.,
           276.9,162.8,130.2,62.3,-16.1,0.,
           526.8,5*0.,
           403.46,5*0.,
           284.9,112.2,65.8,6.6,21.4,4.,
           300.,169.2,204.,27.3,12.3,-9.9,
           163.9,161.3,164.7,42.6,4.9,-.2,
           30*0. &END
 &DFAULT &END
```

A.5. AVEPATH.FB

The program calculates the average path length factor through a target for neutrons scattered in the disk-shaped backing or foil holder in either the forward or backward direction. The volume averaged path length as a function of scattering angle is weighted with the normalized differential scattering cross section to obtain the average path length for the backing. The input is provided through a series of formatted read statements. A description of the input variables is included below.

ENERGY = photoneutron energy

EFIT = neutron energy of the differential scattering cross section used

NMU = number of μ values over which the path length weighting is performed

BORF = 1 - forward scattering analysis
-1 - backward scattering analysis

F0,..F5 = Legendre polynomial coefficients of the differential scattering cross section

SIGT = macroscopic total cross section of the backing material

RMIN = minimum radius of the backing

RBACK = radius of the backing

RDEP = radius of indium foil

YMAX = maximum thickness of backing

YMIN = minimum depth of scattering in the backing

NHIST = number of neutron histories followed for each scattering angle

SEED = random number generator seed

NPTS = total number of scattering angles investigated

NREG = number of regions into which the backing is divided (max = 2)

NRANGE = number of scattering angle ranges provided

THETAL = low theta value in current range

THETAH = upper theta value in current range

NTHETA = number of scattering angles to be uniformly picked between THETAL and THETAH

```
C     PROGRAM AVEPATH.FB     OBJ:AVEPATH.FB.O     D. GRADY     FEB 1981
C     ***VERSION 2       CALCULATES THE AVERAGE PATH LENGTH FACTOR
C     THROUGH A FISSILE DEPOSIT FOR NEUTRONS SCATTERED IN THE BACKING
C     IN EITHER THE FORWARD OR BACKWARD DIRECTION.  IT DETERMINES THE
C     VOLUME AVERAGED PATH LENGTH FACTOR AS A FUNCTION OF THE SCATTERING
C     ANGLE, WEIGHTED BY THE SCATTERING PROBABILITY.
C
      REAL L,MU,MUTH
      INTEGER SEED
      LOGICAL*1 TITLE(60)
      DIMENSION PROB(501),MU(501),THETA(501),STHETA(99),SMU(99),SPATH(99,2),
     1THETAL(10),THETAH(10),NTHETA(10),SPASS(99,2),VOL(2),VAPL(99)
     2,SMUI(99),VAPLI(99),SCAT2(99,2),V(5),Z(5)
      COMMON SPATH,SPASS,SCAT2,SUM,FACTOR,VOL
C
C   "GRAN" IS THE FIFTH ORDER LEGENDRE POLYNOMIAL EXPANSION OF THE
C         DIFFERENTIAL ELASTIC SCATTERING CROSS SECTION FOR THE BACKING MATERIAL.
C
      GRAN(X)=(F0+
     1         F1*X+
     2         F2*.5*(3*X**2-1)+
     3         F3*.5*(5.*X**3-3.*X)+
     4         F4*.125*(35.*X**4-30.*X**2+3.)+
     5         F5*.0625*(126.*X**5-140.*X**3+30.*X))
C
C   READ SOME INPUT DATA FOR THE DETERMINATION OF THE NORMALIZED
C   SCATTERING PROBABILITIES FROM THE LEGENDRE FIT.
C
      READ(5,100) ENERGY,EFIT,NMU,BORF,TITLE
  100 FORMAT(2F6.1,I4,F4.0,60A1)
      READ(5,101) F0,F1,F2,F3,F4,F5
  101 FORMAT(6F6.1)
      PI=3.14159
      DO 5 I=1,598
    5 SPATH(I,1)=0.0
      NMU1=NMU-1
      DO 10  I=1,NMU
      MU(I)=(I-1.)/(NMU1*BORF)
      THETA(I)=ARCOS(MU(I))*180./PI
      PROB(I)=GRAN(MU(I))
   10 SUM=SUM+PROB(I)
      DO 11  I=1,NMU
   11 PROB(I)=PROB(I)/SUM
C
C   "PROB" NOW CONTAINS THE NORMALIZED SCATTERING PROBABILITIES FOR
C         THE "NMU" EQUIDISTANT "MU" VALUES FROM 0 TO 1.
C
      WRITE(6,200)
  200 FORMAT('1PROGRAM "AVEPATH.FB":'/'0THIS CODE DETERMINES THE ',
     1'PATH LENGTH FACTOR THROUGH THE DEPOSIT'/' AVERAGED OVER ALL ',
     2'NEUTRONS SCATTERED IN THE BACKING.'/'-     THIS ',
     3'CALCULATION INVOLVES THE FOLLOWING FOUR STEPS:'/'0',8X,
     4'1.  THE POINTWISE NORMALIZED SCATTERING PROBABILITY MUST BE'/
     5' ',12X,'DETERMINED FROM THE LEGENDRE POLYNOMIAL ',
     6'EXPANSION.'/'0',8X,'2.  THE GEOMETRY WEIGHTED PATH LENGTH ',
     7'FACTOR FOR UP TO 99 ANGLES'/' ',12X,'MUST BE DETERMINED USING ',
     8'MODIFIED PT-SCAT3 MONTE CARLO METHODS.'/'0',8X,'3.  THE PATH ',
     9'LENGTH FACTOR AS A FUNCTION OF "MU" IS SPLINE FITTED.'/'0',8X,
     &'4.  THE SPLINE FITTED PATH LENGTH FACTORS ARE WEIGHTED WITH'/
     1' ',12X,'THE NORMALIZED SCATTERING PROBABILITIES AT SEVERAL ',
     2'POINTS'/' ',12X,'TO OBTAIN THE FINAL PATH LENGTH FACTOR FOR '/
     3' ',12X,'SCATTERING IN THE BACKING.')
      WRITE(6,201) ENERGY
  201 FORMAT('1THE RESULTS OF THE CALCULATION ARE FOR A NEUTRON ENERGY ',
     1'OF:',F6.1,' KEV')
      WRITE(6,202)
  202 FORMAT(' ',69('_'))
      WRITE(6,203) TITLE
  203 FORMAT('-*** THE RESULTS OF STEP #1 ***'/'0  TITLE: ',60A1)
      WRITE(6,204) EFIT,F0,F1,F2,F3,F4,F5,NMU
```

```
  204 FORMAT('0  DATA FROM THE LEGENDRE POLYNOMIAL FIT AT',F6.1,' KEV'/
     1'0  WITH LEGENDRE COEFFICIENTS OF:   FO =',F6.1/36X,'F1 =',F6.1/
     236X,'F2 =',F6.1/36X,'F3 =',F6.1/36X,'F4 =',F6.1/36X,'F5 =',F6.1/
     3'0  FOR',I4,' MU VALUES BETWEEN 0 AND 1.'/'-',15X,'NORMALIZED',
     418X,'NORMALIZED',18X,'NORMALIZED'/' ',15X,'SCATTERING',18X,
     5'SCATTERING',18X,'SCATTERING'/' ',5X,'MU',7X,'PROBABILITY',8X,
     6'MU',7X,'PROBABILITY',8X,'MU',7X,'PROBABILITY'/' ')
      N=NMU/3
      N=N*3
      DO 12 I=1,N,3
   12 WRITE(6,205) MU(I),PROB(I),MU(I+1),PROB(I+1),MU(I+2),PROB(I+2)
  205 FORMAT(3(F11.6,E16.6,1X))
      FS=(FO+F1/2.-F3/8.+F5/16.)/(2.*FO)
      FS1=1.-FS
      WRITE(6,209) FS,FS1
  209 FORMAT('-   FRACTION OF NEUTRONS SCATTERED FORWARD = ',F6.4/
     1       '0  FRACTION OF NEUTRONS SCATTERED BACKWARD = ',F6.4/' ')
      IF(N.EQ.NMU)GO TO 13
      IF(N.EQ.NMU-1)WRITE(6,205) MU(NMU),PROB(NMU)
      IF(N.EQ.NMU-2)WRITE(6,205) MU(NMU-1),PROB(NMU-1),MU(NMU),PROB(NMU)
   13 CONTINUE
C
C   THE NEXT STEP IS TO READ IN THE GEOMETRY, CROSS SECTION AND ANGLE
C   RANGE INFORMATION FOR THE MONTE CARLO ANALYSIS OF THE AVERAGE
C   PATH LENGTH AS A FUNCTION OF SCATTERING ANGLE.
C
      READ(5,102) SIGT,RMIN,RBACK,RDEP,YMAX,YMIN
  102 FORMAT(6E12.6)
      READ(5,103) NHIST,SEED,NRANGE,NPTS,NREG
  103 FORMAT(I5,I10,3I3)
      READ(5,104) (THETAL(I),THETAH(I),NTHETA(I), I=1,NRANGE)
  104 FORMAT(2F8.3,I3)
      K=0
      DO 14 I=1,NRANGE
      LOOP=NTHETA(I)
      DO 15 J=1,LOOP
      K=K+1
      STHETA(K)=(THETAH(I)-THETAL(I))/(NTHETA(I)-1.)*(J-1.)+THETAL(I)
   15 SMU(K)=COS(STHETA(K)*PI/180.)
   14 CONTINUE
      STHETA(NPTS)=STHETA(NPTS)+(1.-BORF)*(180.-STHETA(1)-STHETA(NPTS))/2.
      IF(BORF.EQ.-1.)STHETA(1)=90.
      SMU(NPTS)=0.0
      WRITE(6,206) TITLE
  206 FORMAT('1*** THE RESULTS OF STEP #2 ***'/'0  TITLE: ',60A1)
      KK=1
      WRITE(6,207) KK,YMAX,YMIN,RMIN,RBACK,RDEP,STHETA(NPTS),STHETA(1),SIGT
  207 FORMAT('-  REGION #',I1,' INPUT PARAMETERS'/'0    MAX. DEPTH ',
     1'SAMPLED =',F10.5,' CM'/'      MIN. DEPTH SAMPLED =',F10.5,' CM'/
     2'     MIN. RADIUS SAMPLED =',F10.5,' CM'/
     3'       RADIUS OF BACKING =',F10.5,' CM'/'      RADIUS OF ',
     4'DEPOSIT =',F10.5,' CM'/'      MAX. ANGLE SAMPLED =',F10.5,
     5' DEGREES'/'     MIN. ANGLE SAMPLED =',F10.5,' DEGREES'/
     6'      BACKING SIGMA TOT. =',F10.5,' CM**-1')
      WRITE(6,208) NHIST,SEED
  208 FORMAT('0    NUMBER OF NEUTRON HISTORIES FOLLOWED =',I10,
     1       ' PER SCATTERING ANGLE INVESTIGATED'/
     2       '     BEGINNING PSEUDORANDOM SEED          =',I10)
C
C   PERFORM THE MONTE CARLO-LIKE ANALYSIS OF THE AVERAGE PATH
C   LENGTH FACTORS FOR EACH OF THE DESIRED ANGLES.
C
      NPTS1=NPTS-1
      DO 40 K=1,NREG
      DO 20 I=1,NPTS1
      PL=1./ABS(SMU(I))
      REACH=0.0
      SCAT=0.0
      DO 21 N=1,NHIST
      NOWAY=0
```

```
      R=SQRT((RBACK**2-RMIN**2)*URAND(SEED)+RMIN**2)
      Y=YMIN+URAND(SEED)*(YMAX-YMIN)
      L=PL*Y
      MUTH=Y/SQRT((R+RBACK)**2+Y*Y)
      IF(SMU(I).LT.MUTH)NOWAY=1
      IF(NOWAY.EQ.1)L=(R+RBACK)/SQRT(1.-SMU(I)**2)
      P=EXP(-SIGT*L)
      IF(URAND(SEED)-P)7,7,31
    7 IF(NOWAY.EQ.1)GO TO 21
      XSQ=L*L-Y*Y
      X=SQRT(XSQ)
      IF(R.EQ.0.0)R=1.0E-10
      ARG=(XSQ+R**2-RDEP**2)/(2.0*X*R)
      IF(ARG.LE.-1.0)F=1.0
      IF(ARG.GT.-1.0.AND.ARG.LE.1.0)F=(1.0/PI)*ARCOS(ARG)
      IF(ARG.GT.1.0)F=0.0
      REACH=REACH+F
      GO TO 21
   31 SCAT=SCAT+1.
   21 CONTINUE
      SCAT2(I,K)=SCAT*100./(NHIST*1.)
      SPATH(I,K)=REACH*PL/(NHIST*1.0)
   20 SPASS(I,K)=REACH*100./(NHIST*1.0)
      VOL(K)=PI*(RBACK**2-RMIN**2)*(YMAX-YMIN)
      IF(NREG.EQ.2.AND.K.EQ.1)READ(5,102) RMIN,RBACK,RDEP,YMAX,YMIN
   40 CONTINUE
      KK=2
      IF(NREG.EQ.2)WRITE(6,207) KK,YMAX,YMIN,RMIN,RBACK,RDEP,STHETA(NPTS),
     1STHETA(1),SIGT
      VOLUME=VOL(1)+VOL(2)
      VOL(1)=VOL(1)/VOLUME
      VOL(2)=VOL(2)/VOLUME
C
C   DETERMINE THE VOLUME WEIGHTED PATH LENGTH FACTORS.
C
      DO 50 I=1,NPTS
      SMU(I)=SMU(I)*BORF
      STHETA(I)=ARCOS(SMU(I))*180./PI
   50 VAPL(I)=VOL(1)*SPATH(I,1)+VOL(2)*SPATH(I,2)
   51 WRITE(6,210)
  210 FORMAT('- THE ANGLE AND REGIONWISE PATH LENGTH FACTORS ARE:'/
     1       '0',62X,'PERCENT SCATTERED',7X,'PERCENT NEUTRONS'/
     2       '     ANGLE',9X,'MU',14X,'PATH LENGTH FACTORS',9X,
     3       'THROUGH THE DEPOSIT',6X,'SECOND SCATTERED'/'0',27X,
     4       'REGION 1   REGION 2     TOTAL     REGION 1   REGION 2',
     5       5X,'REGION 1   REGION 2'/' ')
      WRITE(6,211) (STHETA(I),SMU(I),SPATH(I,1),SPATH(I,2),VAPL(I),
     1SPASS(I,1),SPASS(I,2),SCAT2(I,1),SCAT2(I,2), I=1,NPTS)
  211 FORMAT(' ',F9.4,5X,F8.5,5X,F8.4,3X,F8.4,3X,F8.4,4X,F8.4,3X,F8.4,
     1       5X,F8.4,3X,F8.4)
      WRITE(6,212) TITLE
  212 FORMAT('1*** THE RESULTS OF STEP #3 AND STEP #4 ***'/
     1       '0  TITLE: ',60A1)
      WRITE(6,213)
  213 FORMAT('0',24X,'PATH LENGTH',7X,'SCATTERING'/'   ANGLE',9X,
     1'MU',9X,'FACTOR',8X,'PROBABILITY',8X,'PRODUCT'/' ')
C
C   DETERMINE THE PATH LENGTH FACTOR THROUGH THE DEPOSIT FOR ALL
C   NEUTRONS SCATTERED ANYWHERE IN THE BACKING.
C
   95 DO 70 I=1,NMU
      CALL INTER(MU(I),SMU,VAPL,FITTED,NPTS)
      PROD=PROB(I)*FITTED
      FACTOR=FACTOR+PROD
      WRITE(7,214) THETA(I),MU(I),FITTED,PROB(I),PROD
   70 WRITE(6,214) THETA(I),MU(I),FITTED,PROB(I),PROD
  214 FORMAT(F9.4,5X,F8.5,4X,F8.4,7X,E12.6,5X,E12.6)
      WRITE(6,215) FACTOR
  215 FORMAT('-*** THE AVERAGE PATH LENGTH FACTOR IS:',F9.5)
      IF(BORF.EQ.-1.)WRITE(6,216)
```

```
      IF(BORF.EQ.1.)WRITE(6,217)
  216 FORMAT('-     FOR THE CASE OF BACKSCATTERED NEUTRONS.')
  217 FORMAT('-     FOR THE CASE OF FORWARD SCATTERED NEUTRONS.')
      RETURN
      END


      FUNCTION URAND(IX)
      IY=IX*65539
      IF(IY)5,6,6
    5 IY=IY+2147483647+1
    6 URAND=IY
      URAND=URAND*.4656613E-9
      IX=IY
      RETURN
      END


C
C   THE FOLLOWING SUBROUTINE TAKES THE INPUTTED "MU" VALUE AND
C   DOES A LINEAR SPLINE FIT OR INTERPOLATION FROM THE PATH LENGTH
C   AS A FUNCTION OF ANGLE DATA TO OBTAIN THE PATH LENGTH ASSOCIATED
C   WITH THE GIVEN VALUE OF "MU".
C
      SUBROUTINE INTER(MU,X,Y,FITTED,NPTS)
      DIMENSION X(99),Y(99),V(2),Z(2)
      REAL MU
C
C   SCAN THE PATH LENGTH TABLE FOR THE TWO MU VALUES WHICH
C   ENCLOSE THE "MU" VALUE OF INTEREST.
C
      DO 10 I=1,NPTS
      IF(MU.LE.X(I))GO TO 20
   10 CONTINUE
      GO TO 999
   20 IF(I.EQ.1)I=2
      V(1)=X(I-1)
      V(2)=X(I)
      Z(1)=Y(I-1)
      Z(2)=Y(I)
C
C   CALCULATE THE SLOPE AND INTERCEPT OF THE LINEAR INTERPOLATION.
C
      SLOPE=(Z(2)-Z(1))/(V(2)-V(1))
      CON=Z(1)-V(1)*SLOPE
      FITTED=SLOPE*MU+CON
      RETURN
  999 WRITE(6,100)
  100 FORMAT('0**ERROR: TABLE ENTRY COULD NOT BE FOUND.')
      RETURN
      END
```

APPENDIX B

SIMPLIFIED FLUX CALCULATION APPROACH

In the simplified flux calculation, the emission angular distribution histogram from VES is used directly to obtain an expression for the scalar flux at a distance Z from the source center. As a result, $F(\mu)$ is defined as

$$F(\mu) = f_1 \Big|_{\mu_0}^{\mu_1}, f_2 \Big|_{\mu_1}^{\mu_2}, \ldots. f_{20} \Big|_{\mu_{19}}^{\mu_{20}} \qquad \text{B.1}$$

where: f_i = number of neutrons in the i^{th} angular bin (μ_{i-1} to μ_i)

and the normalization constant, A_n is determined from equation 6.B.2 as

$$A_n = \Delta\mu \sum_{i=1}^{20} f_i \qquad \text{B.2}$$

where: $\Delta\mu = 1/20$

Using the same variables and geometry as described in figure 6.B.1, equations 6.B.4 and 6.B.1 can be combined to produce the integral for the histogram-determined flux, $\phi_H(Z)$,

$$\phi_H(Z) = \frac{-1}{4\pi A_n R_s Z} \sum_{i=1}^{20} f_i \int_{r(\mu_{i-1})}^{r(\mu_i)} \frac{dr}{r} \qquad \text{B.3}$$

with $r(\mu)$ being determined from equations 6.B.7 and 6.B.8 as

$$r(\mu) = \sqrt{Z^2 - R_s^2(1-\mu^2)} - R_s\mu \quad . \qquad \text{B.4}$$

Performing the integration in equation B.3 and substituting the appropriate $r(\mu_i)$ values, the histogram flux expression becomes

$$\phi_H(Z) = \frac{-1}{4\pi A_n R_s Z} \sum_{i=1}^{20} f_i \ln\left[\frac{\sqrt{Z^2 - R_s^2(1-\mu_i^2)} - R_s\mu_i}{\sqrt{Z^2 - R_s^2(1-\mu_{i-1}^2)} - R_s\mu_{i-1}}\right] \qquad \text{B.5}$$

APPENDIX C

THE SPURIOUS PULSE PROBLEM

C.1. Problem Description

During the intial operation of the beta detector an unusual spurious problem was encountered. A small, but steady increase in the detector background with time was observed. This increase was traced to spurious pulses from the detector which were present even in the absence of a beta source. The spurious pulse problem in proportional counters as discussed in a review by Campion (CAM 73) is normally associated with periodic afterpulsing due to a photoelectric effect at the cathode. Optical radiation liberated in the Townsend avalanche initiated by charged particle interaction in the detector active volume can give rise to a photoelectron at the cathode. This process can then produce a spurious pulse train with a period equal to the electron transit time to the anode. In general, amplifier time constants on the order of tens of microseconds and detector operation at or near the center of the beta plateau reduces the spurious pulse problem to insignificant levels. Both criteria were met with this gas flow proportional counter, strongly suggesting an alternative mechanism for the spurious pulses.

C.2. Source of the Problem

Initially, a low-level, electrical breakdown was suspected as the source of the spurious pulses. This led to a variety of changes in the counter design, including the new anode mounting procedure described in section 4.A. After each modification the anode wires were replaced and the spurious pulses reappeared after several days of operation. This behavior suggested that something was building up on the wires. A quick, in-place cleaning of the wires with acetone temporarily solved the spurious pulse problem. The P-10 flow gas of the detector was suspected as the source of the problem. A change of P-10 supplies remedied the situation and it has not reoccurred in four years of detector operation.

Microscopic examination wires exposed to the original flow gas revealed several deposits on the surface of the wires. The nature of the deposits suggested chemical interaction of trace contaminants in the flow gas with one or more components of the anode wires. These results indicated that the source of the spurious pulse problem was a contaminant in the P-10 flow gas.

C.3. Investigation of the Cause

An attempt to both identify the flow gas contaminant and determine the spurious pulse formation mechanism was made. Anode wires which has been operated at 1950 V for

one week, as well as a control sample of the wire, were examined with a scanning electron microscope (SEM). Figure C.1 is an electron micrograph of the control wire at a magnification of 2000X. No remarkable deposits of any sort were observed.

Figures C.2 and C.3, however, clearly indicate the results of an interaction of a component of the flow gas with a component of the wire. The dendritic deposit on the wire of figure C.2 (1000X magnification) appears to follow a die line from the drawing of the wire. This suggests that the growth of the deposits initiated at surface defects and supports the possibility that the interaction is chemical in nature.

Figure C.3 (5000X magnification) is a micrograph of the wire surface beneath a deposit which was intentionally removed. Both the smooth pit and the deep, exaggerated die lines observed in this photograph are also characteristic of the results of chemical attack, further substantiating the chemical interaction theory.

In order to determine the identity of the flow gas contaminant, an investigation of the deposit composition was made using a scanning electron microprobe. With this device the characteristic X-rays of the deposit were excited with an electron beam and detected by a thin window proportional counter. In all of the deposits examined, the X-rays were from predominantly copper (major

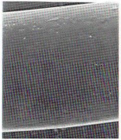

Figure C.1.

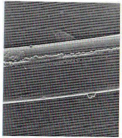

Figure C.2.

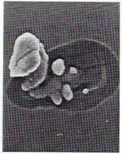

Figure C.3.

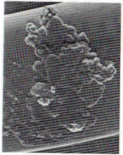

Figure C.4.

Figure C.1. Control Wire (2000X)
2. Dendritic Deposit (1000X)
3. Wire Surface Beneath a Deposit (5000X)
4. Charge Build-up Effects (2000X)

Figure C.1.

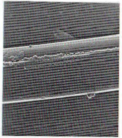

Figure C.2.

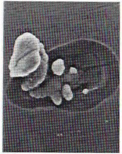

Figure C.3.

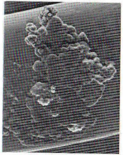

Figure C.4.

Figure C.1. Control Wire (2000X)
2. Dendritic Deposit (1000X)
3. Wire Surface Beneath a Deposit (5000X)
4. Charge Build-up Effects (2000X)

Figure C.1.

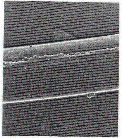

Figure C.2.

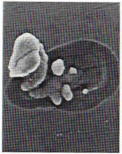

Figure C.3.

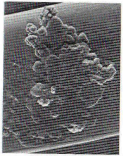

Figure C.4.

Figure C.1. Control Wire (2000X)
2. Dendritic Deposit (1000X)
3. Wire Surface Beneath a Deposit (5000X)
4. Charge Build-up Effects (2000X)

wire component) and sulfur (apparent component of the P-10 gas contaminant). Additional proof that the deposits were indeed copper and sulfur (probably copper sulfide) was provided by both copper and sulfur X-ray imaging. The source of the X-rays coincided exactly with the location of the deposits on the wire.

Although, most certainly not elemental sulfur, further attempts to identify the sulfur bearing impurity of the flow gas led only to the conclusion that its concentration was low. The most sensitive device, a gas chromatography-mass spectrometer, with a detection threshold of about 500 ppm revealed no contaminant. Regardless of the fact that the contaminant was not identified, it is clear from the results of this investigation that a low-level, chemically reactive, sulfur bearing contaminant in the P-10 gas was the cause of the spurious pulse problem.

A potential formation mechanism for the pulses can also be advanced from observations during the investigation. Several of the wire deposits exhibited image flickering on the CRT display of the SEM. This effect is indicative of non-conductive surfaces which accumulate charge and deflect the SEM electron beam. On the micrograph of figure C.4 (2000X magnification) this effect is manifested by relatively bright spots on the photograph. This charging effect suggests that the copper sulfide is acting as an insulator. Electrons produced in an avalanche

accumulate on the deposit until enough charge existed to allow a short to the anode. The resulting pulse would depend upon factors such as deposit thickness and resistance, but it could certainly be mistaken by the detector electronics as a true signal pulse.

C.4. Conclusion

Specifically, a small, sulfur bearing contaminant in the P-10 flow gas chemically interacted with the anode wire to form spurious pulses in the proportional counter. Although the fill gas is not normally considered a major source of difficulty in many gas-filled detector applications, this study would recommend its consideration when detector response deviates from expected performance.

More generally, it is possible that the long term degradation in gas flow detector performance may be due, at least in part, to the accumulation of very low concentration contaminants (from the counter gas) on the anode wires.

REFERENCES

BAE 65 A. P. Baerg, "Measurement of Radioactive Disintegration Rate by the Coincidence Method", Metrologia, 2, No. 1, 23, (1965).

BAE 73 A. P. Baerg, "The Efficiency Extrapolation Method in Coincidence Counting", Nuclear Instruments and Methods, 112, 143, (1973).

BAL 80 G. T. Baldwin, private communication, 1980.

BAL 81 G. T. Baldwin, Ph.D. Dissertation, Department of Nuclear Engineering, The University of Michigan, (1981).

BEL 66 T. S. Belanova, A. A. Van'kov, F. F. Mikhailus and Yu. Ya. Stavisskii, "Absolute Measurements of the Absorption Cross Sections of 24 keV Neutrons", J. Nuclear Energy, 20, A/B, 411 (1966).

BEN 69 F. Bensch, F. Vesely and H. Hejtmanek, "A Monte Carlo Program for the Determination of the Neutron Energy Spectrum of Photoneutron Sources", Nukleonik, 6, 300 (1968).

BJO 74 A. Bjork and G. Dahlquist, Numerical Methods, Prentice-Hall, Inc., New Jersey, (1974).

BOW 76 W. C. Bowman, Master's Thesis, Department of Nuclear Engineering, The University of Michigan, (1976).

BOZ H. Bozorgmanesh, Ph.D. Dissertation, Department of Nuclear Engineering, The University of Michigan, (1976).

CAM 59 P. J. Campion, "The Standardization of Radioisotopes by the Beta-Gamma Coincidence Method Using High Efficiency Detectors", J. Appl. Radiation and Isotopes", 4, 232,(1959).

CAM 73 P. J. Campion, "Spurious Pulses in Proportional Counters, Nuclear Instruments and Methods, 112, 75, (1973).

CHA 65 A. K. Chaubey and M. L. Sehgal, Nuclear Physics, 66, 267 (1965).

COX 64 S. A. Cox, "Neutron Activation Cross Sections for Br^{79}, Br^{81}, Rh^{103}, In^{115}, I^{127} and Ta^{181}", Phys. Rev., 133, B378, (1964).

DAV 76 M.C. Davis, Ph.D. Dissertation, Department of Nuclear Engineering, The University of Michigan, (1976).

DIE 56 W. Diethorn, NYO-6628, (1956).

ENG 76 J. C. Engdahl, Master's Thesis, Department of Nuclear Engineering, The University of Michigan, (1976).

ENG 78 J. C. Engdahl, Ph.D. Dissertation, Department of Nuclear Engineering, The University of Michigan, (1978).

GIL 73 D. M. Gilliam, Ph.D. Dissertation, Department of Nuclear Engineering, The University of Michigan, (1973).

GRA 79 D. J. Grady, G. T. Baldwin and G. F. Knoll, NBS Special Publication 594, Knoxville, Tenn. 976, (1979).

GRE 68 H. A. Grench and H. O. Menlove, "$In^{113}(n,\gamma)In^{114m}$ $In^{113}(n,n')In^{113m}$, $In^{115}(n,\gamma)In^{116m,116g}$ and $In^{115}(n,n')In^{115m}$ Activation Cross Sections Between 0.36 and 1.02 MeV", Phys. Rev., 165, 1298, (1968).

JOH 59 A. E. Johnsrud, M. C. Silbert and H. H. Barschall, "Energy Dependence of Fast Neutron Activation Cross Sections", Phys. Rev., 116, 927, (1959).

KNO 79 G. F. Knoll, Radiation Detection and Measurement, John Wiley and Sons, New York, (1979).

KON 59 V. N. Kononov, Yu. Ya. Stavisskii, and V. A. Tolstikov, "Radiative Capture Cross Sections for 25 keV", J. Nuclear Energy, 11, 46, (1959).

KOR 79 W. Korman, Cf^{252} Information Center, private communication, 1979.

LED 78 C. M. Lederer and V. S. Shirley, Table of Isotopes, Seventh Edition, John Wiley and Sons, (1978).

MEN 67 H. O. Menlove and H. A. Grench, Phys. Rev., 163, 1299, (1967).

MOS 60 E. R. Mosburg, Jr. and W. M. Murphy, National Bureau of Standards Technical Note 63, "Single Scattered Neutrons from an Isotropic Point Source", (1960).

NCR 78 National Committee on Radiation Protection and Measurement. A Handbook of Radioactivity Measurements Procedures, NCRP Report #58, (1978).

PUT 50 J. L. Putman, British Journal Radiol., 23, 46, (1950).

RIG 80 W. L. Rigot, Neutron Activation Analysis Performed at the University of Michigan, 1980.

RIM 75 K. Rimawi and R. E. Chrien, Proceedings Conf. Nuclear Cross Section Technology, NBS Special Publication #425, 920,(1975).

ROB 74 J. C. Robertson, private communication, 1974.

ROB 80 J. C. Robertson, private communication, 1980.

RYV 73 T. B. Ryves, J. B. Hunt and J. C. Robertson, "Neutron Capture Cross Section Measurements for U^{238} and In^{115} between 150 and 630 keV", J. Nuclear Energy, 27, 519, (1973).

SMI 75 D. L. Smith and J. W. Meadows, "Cross Sections for the $Zn^{68}(n,p)Cu^{66}$, $In^{113}(n,n')In^{113m}$ and $In^{115}(n,n')In^{115m}$ Reactions Near Threshold to 10 MeV", ANL/NDM-14, (1975).

SMI 76 D. L. Smith, "Evaluation of the $In^{115}(n,n')In^{115m}$ Reaction for the ENDF/B-IV Dosimetry File", ANL/NDM-26, (1976).

SMI 78 D. Smith, "Improved Correction Formula for Coincidence Counting", Nuclear Instruments and Methods, 152, 505, (1978).

SNA 76 W. Snapp, Master's Thesis, Department of Nuclear Engineering, The University of Michigan, (1976).

STE 75 W. P. Stephany, Ph.D. Dissertation, Department of Nuclear Engineering, The University of Michigan, (1975).